



HAL
open science

The role of sulphur on the melting of Ca-poor sediment and on trace element transfer in subduction zones: an experimental investigation

Anne-Aziliz Pelleter, Gaëlle Prouteau, Bruno Scaillet

► To cite this version:

Anne-Aziliz Pelleter, Gaëlle Prouteau, Bruno Scaillet. The role of sulphur on the melting of Ca-poor sediment and on trace element transfer in subduction zones: an experimental investigation. *Journal of Petrology*, 2021, 62 (9), pp.egab005. 10.1093/petrology/egab005 . insu-03143260

HAL Id: insu-03143260

<https://insu.hal.science/insu-03143260>

Submitted on 16 Feb 2021

HAL is a multi-disciplinary open access archive for the deposit and dissemination of scientific research documents, whether they are published or not. The documents may come from teaching and research institutions in France or abroad, or from public or private research centers.

L'archive ouverte pluridisciplinaire **HAL**, est destinée au dépôt et à la diffusion de documents scientifiques de niveau recherche, publiés ou non, émanant des établissements d'enseignement et de recherche français ou étrangers, des laboratoires publics ou privés.

The role of sulphur on the melting of Ca-poor sediment and on trace element transfer in subduction zones: an experimental investigation

Anne-Aziliz Pelleter ¹, Gaëlle Prouteau ^{1*}, Bruno Scaillet ¹

¹ Institut des Sciences de la Terre d'Orléans (ISTO), UMR 7327, Université d'Orléans, CNRS, BRGM, F-45071 Orléans, France

* *Corresponding author. E-mail: gaelle.prouteau@cnrs-orleans.fr*

ABSTRACT

We performed phase equilibrium experiments on a natural Ca-poor pelite at 3 GPa, 750-1000°C, under moderately oxidizing conditions, simulating the partial melting of such lithologies in subduction zones. Experiments investigated the effect of sulphur addition on phase equilibria and compositions, with S contents of up to ~ 2.2 wt. %. Run products were characterized for their major and trace element contents, in order to shed light on the role of sulphur on the trace element patterns of melts produced by partial melting of oceanic Ca-poor sediments. Results show that sulphur addition leads to the replacement of phengite by biotite along with the progressive consumption of garnet, which is replaced by an orthopyroxene-kyanite assemblage at the highest sulphur content investigated. All Fe-Mg silicate phases produced with sulphur, including melt, have higher MgO/(MgO+FeO) ratios (relative to S-free/poor conditions), owing to Fe being primarily locked up by sulphide in the investigated redox range. Secular infiltration of the mantle wedge by such MgO and K₂O-rich melts may

have contributed to the Mg and K-rich character of the modern continental crust. Addition of sulphur does not affect significantly the stability of the main accessory phases controlling the behaviour of trace elements (monazite, rutile and zircon), although our results suggest that monazite solubility is sensitive to S content at the conditions investigated. The low temperature ($\sim 800^{\circ}\text{C}$) S-bearing and Ca-poor sediment sourced slab melts show Th and La abundances, Th/La systematics and HFSE signatures in agreement with the characteristics of sediment-rich arc magmas. Because high S contents diminish phengite and garnet stabilities, S-rich and Ca-poor sediment sourced slab melts have higher contents of Rb, B, Li (to a lesser extent), and HREE. The highest ratios of La/Yb are observed in sulphur-poor runs (with a high proportion of garnet, which retains HREE) and beyond the monazite out curve (which retains LREE). Sulphides appear to be relatively Pb-poor and impart high Pb/Ce ratio to coexisting melts, even at high S content. Overall, our results show that Phanerozoic arc magmas from high sediment flux margins owe their geochemical signature to the subduction of terrigenous, sometimes S-rich, sediments. In contrast, subduction of such lithologies during Archean appears unlikely or unrecorded.

Key words: arc magmas; experimental petrology; sediment melting; sulphur cycle; trace elements geochemistry

INTRODUCTION

Arc volcanism has been a prominent source of sulphur to the atmosphere during much of geological time. Restored sulphur contents of arc magmas prior to eruption yield bulk S contents at ca 0.5 wt. %, reaching several wt. % in some instances (Scaillet & Pichavant, 2003). High sulphur concentrations (typically 900-2500 ppm, but values extend as high as 7000 ppm) in silicate-melt inclusions hosted in olivine from arc harzburgitic xenoliths or primitive basaltic lava samples from convergent settings also indicate that arc mantle may be significantly enriched in sulphur (up to 500 ppm) relative to MORB (Mid-Ocean Ridge Basalt) source mantle (ca 120 ppm, Salters & Stracke, 2004) (Métrich *et al.*, 1999; de Hoog *et al.*, 2001a; Cervantes & Wallace, 2003; Wallace & Edmonds, 2011). This suggests large-scale fluxing of sulphur into the mantle wedge, transported by an H₂O-rich agent with up to several wt. % sulphur (Cervantes & Wallace, 2003). The main contributor to the sulphur budget of subduction zones is altered ocean crust (AOC) (1.5×10^{12} mol year⁻¹), followed by serpentinite (0.68×10^{12} mol year⁻¹) and sediments (0.62×10^{12} mol year⁻¹), which contribute to ~20 % of the total input (Evans, 2012). The estimate for sediments is based on an assumed value for the total subducted sediment flux of 1.73×10^{12} kg year⁻¹, which includes 8 wt. % water and a maximum S content of 1.15 wt. % (Evans, 2012). This estimated sulphur budget suggests that ~15 wt. % of subducted sulphur is recycled by arc magmatism (Evans, 2012). For instance, Li *et al.* (2020) have shown, based on the Tianshan high pressure-low temperature terrane study, that dehydration-related fluids transfer up to 20 wt. % of total subducted sulphur from the slab to the mantle wedge. Sulphur isotopes in arc volcanoes suggest moreover that subducted oceanic sediment is a likely and significant source for the S enrichment observed in arc magmas (Alt & Burdett, 1992; de Hoog *et al.*, 2001b; Bouvier *et al.* 2008), although the

isotopic signature of the sediment component that ultimately contribute to magma source is difficult to predict (e.g. Evans *et al.*, 2014).

Traditionally, hydrous fluids are thought to transport sulphur from the subducting slab to the site of melting in the mantle wedge (e.g. Tomkins & Evans, 2015; Jégo & Dasgupta, 2013; Walters *et al.*, 2019; Li *et al.*, 2020). Sulphur exhibits low solubility in silicic melts at low pressure and temperature (e.g. Luhr, 1990; Carroll & Webster, 1994; Scaillet *et al.*, 1998), and consequently silicate melts were usually considered not to be an efficient agent of sulphur extraction from the slab. However, experimental works have demonstrated that the sulphur content of high pressure oxidized hydrous silicic melts is at least 10-20 times higher than at low pressures (Prouteau & Scaillet, 2013; Jégo & Dasgupta, 2014; Canil & Fellows, 2017; D'Souza & Canil, 2018; Li *et al.*, 2019). This finding reduces the restriction that the sulphur-rich character of present-day arc volcanism bears evidence solely of a sulphur-rich hydrous fluid. The most extreme sulphur content in these recent studies was achieved with a pelite (of the same composition as our starting product) doped with 4 wt. % elemental S at 3 GPa, conditions under which the felsic silicate melt dissolved nearly 1 wt. % sulphur at 900°C (Prouteau & Scaillet, 2013). Sulphur has been shown to affect the stabilities of phases other than those S-bearing, i.e. amphibole, biotite in magmas (Scaillet & Evans, 1999; Costa *et al.*, 2004; Prouteau & Scaillet, 2013; Canil & Fellows, 2017; D'Souza & Canil, 2018). It is thus important to assess the role of S on the stability of phases of subducted sediments in order to evaluate its potential effect on trace element patterns.

Within this context, this study aims at exploring the phase relationships and compositions (major elements, trace elements, sulphur content) during the high pressure hydrous melting of a Ca-poor natural sediment both with and without S so as to constrain the role of the latter on the geochemical pattern of arc magmas. The trench sediment is largely dominated by terrigenous sediments and has a geochemical composition very similar to the

post-Archean average shales and the upper continental crust (Plank & Langmuir, 1998). Piston-cylinder experiments were performed in the temperature range 750 to 1000°C at 3 GPa. Such P-T conditions are inferred to prevail at the top of the subducted slab beneath the majority of active volcanic arcs (e.g. Syracuse *et al.*, 2010), and are thus supposed to mimic slab melting nowadays. Our experiments were designed to test flux-melting mechanism by using starting materials in which H₂O contents (~8.5 to 15 wt. % H₂O) exceed the water budget of hydrous minerals, under moderately oxidized conditions. We explored a range of bulk sulphur content, from ~ 900 ppm up to ~ 2.2 wt. %. Estimates of the sulphur content of subducting sediments or exhumed sediment eclogites are sparse. Goldhaber (2003) reported total sulphur abundance in recent marine sediments (exclusive of sediment deposited under anoxic conditions and those dominated by a carbonate matrix) varying from ~ 0.1 wt. % to greater than 2 wt. %. Metapelites in the Tianshan HP metamorphic belt have $[S]_{\text{wr}} = 1101\text{-}5612$ ppm which are the highest whole-rock sulphur concentrations of high pressure (HP) exhumed slab rocks (including eclogite and serpentinites) reported so far (Li *et al.*, 2020). Evans (2012), following the approach of Canfield (2004), assumes that approximately 1 wt.% Fe in deep sea sediments is available for pyrite formation, which gives a S content for these sediments of 1.15 wt.% (maximum value for the case where all subducting sediments have undergone pyrite formation in the sulphide stability field, and given a 50 % relative uncertainty). Therefore, natural variation in sediment S content (measured or estimated), although poorly constrained, is roughly of the same order of magnitude as the range of variation explored in our experiments.

Experimental charges were analysed by EPMA (Electron Probe Microanalysis) and LA-ICP-MS (Laser Ablation Inductively Coupled Plasma Mass Spectrometry). Our results are then applied to subduction zone magmatism, in an effort to unravel the role of such sediment-sourced slab melt on the geochemical signature of arc magmas (and continental

crust). Below, in order to put our results in a broader perspective, we first review in some detail the main geochemical characteristics of arc magmas, focusing on trace elements commonly used in the geochemical community, and their main mineral carriers including micas, garnet, monazite, zircon and rutile.

KEY GEOCHEMICAL FEATURES OF ARC MAGMAS

There is a consensus that key geochemical features of island arc basalt (IAB) (e.g. the lower abundances of HFSE (High Field Strength Elements) relative to the LREE (Light Rare Earth Elements) and LILE (Large Ion Lithophile Elements), with respect to MORB are controlled by the addition of slab-derived fluids of various nature (fluids, melts or supercritical liquids, e.g. Schmidt & Jagoutz, 2017) to the peridotitic mantle wedge. A single slab component, much beloved for its simplicity, is often advocated, but detailed studies on individual arcs as well as global surveys of primitive arc magma compositions have led to the inescapable conclusion that in many, if not all, arcs there are (at least) two discrete slab components (expelled from subducted sediment and altered oceanic crust, respectively) added, with variable contribution, to a depleted mantle (e.g. Kay, 1980; Ellam & Hawkesworth, 1988; Plank & Langmuir, 1992; McDermott *et al.*, 1993; Miller *et al.*, 1994; Regelous *et al.*, 1997; Turner *et al.*, 1997; Class *et al.*, 2000; Elliott, 2003; Schmidt & Jagoutz, 2017). The “sediment-starved” arc magmas typically have low concentrations of incompatible elements when compared with those in sediment-rich arcs and exhibit low La/Sm and high Ba/Th and U/Th ratios, common activity excess of ^{238}U over ^{230}Th , as well isotopic signatures consistent with contributions from an altered MORB source (Hawkesworth *et al.*, 1997; Elliott, 2003). Therefore, transport of material from altered mafic oceanic crust to the arc lava source needs to selectively fractionate elements that are highly incompatible during mantle melting (e.g. Ba

from Th or U from Th). These characteristics have been traditionally ascribed to an aqueous fluid, selectively enriched in “mobile” elements such U and Ba, derived from the altered oceanic crust (e.g. Elliott *et al.*, 1997; Elliott, 2003; Pearce *et al.*, 2005). However, Carter *et al.* (2015) and Skora *et al.* (2015, 2017) have demonstrated that oceanic crust or carbonated-sediment can contribute high pressure melts with high ratios of Ba/Th and U/Th. Such a process could also explain the high Ba/Th and U/Th ratios observed in high-pressure exhumed mélange zones; these mélanges are interpreted as blobs of low density diapirs (made of variable amount of crust+sediment+mantle) formed at the slab-mantle interface and transported into the hot corner of the mantle wedge beneath arcs (e.g. Marschall & Schumacher, 2012).

Arc magmas dominated by a sediment component are characterized by low Ba/Th or U/Th ratios and high La/Sm ratio associated with very high incompatible elements, such as Th and LREE (e.g. Hawkesworth *et al.*, 1997; Elliott, 2003). They plot generally either close to the equiline or sporadically towards slight Th activity excess on a $^{230}\text{Th}/^{232}\text{Th}$ versus $^{238}\text{U}/^{232}\text{Th}$ diagram (e.g. Condomines & Sigmarsson, 1993; Elliott *et al.*, 1997; Hawkesworth *et al.*, 1997; Turner *et al.*, 2012). A high concentration of ^{10}Be in arc lavas is an unequivocal indicator of the contribution of subducting sediments (e.g. Morris *et al.*, 1990). Additionally, sediment partial melting is required for critical elements such as Th and Be to be efficiently transferred into the mantle wedge (Johnson & Plank, 1999; Hermann & Spandler, 2008; Hermann & Rubatto, 2009) though this remains debated (e.g. Kessel *et al.*, 2005; Schmidt & Poli, 2014). Plank and Langmuir (1993, 1998) and Plank (2005) have demonstrated moreover that the ratios of key incompatible elements (e.g. Th/La) at various arcs worldwide correspond closely to the subducted sediment signatures, which implies that this ratio is not, or weakly, fractionated during sediment melting. Skora *et al.* (2015, 2017) have shown that, for slab-top temperatures compatible with recent numerical models, LREE and Th fluxes entering the arc

basalt source region from Ca-rich sediments is negligible, owing to residual epidote and/or carbonate in such lithologies. The LREE and Th enrichment in arc magmas must therefore originate from the Ca-poor sedimentary veneer, a hypothesis explored in our experiments.

The unique and ubiquitous HFSE negative anomaly in arc magmas is traditionally ascribed to the HFSE depletion, relative to other elements of comparable incompatibility, of the fluid component(s) leaving the slab. The negative Nb (and Ta) anomaly becomes even more pronounced in sediment-rich subduction zones, even though Nb abundances are higher in these contexts. Although most oceanic sediments show negative Nb anomalies, to generate the source of the enriched arc lavas requires the addition of a component with even higher Th/Nb than the subducting sediment (Elliott, 2003). The Nb/Ta ratios of mafic arc magmas (e.g. Münker *et al.*, 2004), as that of most accessible silicates, including the bulk continental crust (e.g. Barth *et al.*, 2000), are lower than the chondritic value of 17.5 (Jochum *et al.*, 2000) or 19.9 (Münker *et al.*, 2003). There have been several attempts to identify reservoirs with super-chondritic Nb/Ta to solve this imbalance (see Stepanov & Hermann (2013) and references therein). One hypothesis is that the sub-chondritic nature of the bulk silicate Earth is a feature that was inherited within the first 100 million years of Earth's history, perhaps via preferential sequestration of Nb into the core during planetary accretion (Wade & Wood, 2001; Münker *et al.*, 2003; Tang *et al.*, 2019). The other is that there is a hidden reservoir of refractory rutile-bearing eclogites with super-chondritic Nb/Ta ratios in the deep mantle to counterbalance the continental crust and depleted mantle (Kamber & Collerson, 2000; Rudnick *et al.*, 2000; Xiong *et al.*, 2011). The low Nb/Ta ratios are in this case inherited from the source, such as through slab melting (e.g. Xiong *et al.*, 2011) or through differential transport in hydrous fluids. Below we explore these last two hypotheses in the light of our experimental results.

Since the pioneering work of White & Patchett (1984), many isotopic studies have concluded that subduction and recycling of marine sediments contribute to the Hf-Nd composition of arc magmas (e.g. Carpentier *et al.*, 2009; Chauvel *et al.*, 2009). Zircon is the main carrier of Zr and Hf in detrital sediment (e.g. van de Flierdt *et al.*, 2007; Chen *et al.*, 2011). Given the low solubility of zircon in aqueous fluids (e.g. Ayers *et al.*, 1991; Kovalenko & Ryzhenko, 2009), some authors have proposed that sediment melts transfer efficiently their isotopic signature to the source of magma (e.g. Woodhead *et al.*, 2001; Carpentier *et al.*, 2009; Nebel *et al.*, 2011). The dissolution of zircon moreover controls the Zr/Hf and Lu/Hf ratios of the slab fluid, which may further help to unravel the isotopic sediment signature.

Finally, arc magmas are characterized by a marked enrichment in Pb compared to the HFSE and REE. The Ce/Pb ratio in arc basalts and average continental crust (~ 3) is considerably below that of oceanic basalts (~ 25) and of the bulk Earth (~ 10). This geochemical signature is classically attributed to the fluxing of the mantle wedge by low Ce/Pb hydrous fluids of various salinities, generated by the dehydration of subducted lithologies (e.g. Brenan *et al.*, 1995; Chauvel *et al.*, 1995; Keppler, 1996; Kessel *et al.*, 2005a). Pb isotopic compositions provide definitive evidence of a sediment contribution (e.g. Miller *et al.*, 1994; Gertisser & Keller, 2003; Carpentier *et al.*, 2008). Previous studies have shown that Ca-poor, sediment-derived, hydrous melts successfully fractionate Pb from Ce (e.g. Johnson & Plank, 1999; Hermann & Rubatto, 2009). As Pb is a nominally chalcophile element, one can expect a different behaviour in sulphur-rich systems, that can be evaluated in our experiments.

EXPERIMENTAL AND ANALYTICAL PROCEDURES

Rationale

Several experimental studies have focused on the trace element signature of Ca-poor sediment melts in subduction zones by using either synthetic (e.g. Hermann & Rubatto, 2009; Skora & Blundy, 2010, 2012; Stepanov *et al.*, 2012) or natural (Johnson & Plank, 1999; Martindale *et al.*, 2013) sediments. In most cases, the starting materials of these studies were doped with trace elements to facilitate trace element analysis of experimental run products and enhance the stability of accessory phases. This makes, however, direct application of experimental data to natural contexts difficult (Skora & Blundy, 2012; Stepanov *et al.*, 2012). Here we have deliberately used a non-doped starting material, which makes run product characterization more challenging, sometimes impossible for some elements or phases, but such an approach has the benefit of a direct correspondence with natural conditions. We have thus chosen to work with a real, low grade sediment, keeping in mind that any subducted lithology may be chemically modified during prograde metamorphism and subsequent devolatilization. It is however difficult to quantify volatiles lost from the slab. Moreover, water (and dissolved mobile elements) is reintroduced to the sediments at sub-arc depths, by dewatering of underlying subducting sediments, altered oceanic crust and serpentinite (e.g. Ulmer & Trommsdorff, 1995; Syracuse *et al.*, 2010; van Keken *et al.*, 2011; Bénard *et al.*, 2018). Our hydrous experiments (8.53 % bounded H₂O or around 15 wt. % total H₂O, see below) simulate this scenario, as already explored in previous studies (e.g. Johnson & Plank, 1999; Prouteau *et al.*, 1999, 2001; Hermann & Green, 2001; Klimm *et al.*, 2008; Skora & Blundy, 2010; Martindale *et al.*, 2013; Prouteau & Scaillet, 2013).

While the case for H₂O-rich conditions and related high fO₂ in arc magmas is clear (Kelley & Cottrell, 2009), that for S is less obvious. There is growing evidence for fluxes of sulphate in fluids during metamorphism both in and outside the subduction zone setting (e.g.

Pons *et al.*, 2016; Connolly & Galvez, 2018; Walters *et al.*, 2019, 2020). Such aqueous fluids have been described in inclusions trapped in metasomatic veins preserved in ultrahigh pressure eclogite (e.g. Sulu orogen : Zhang *et al.*, 2008; Frezzotti & Ferrando, 2015). Sulphate inclusions have also been identified in metasomatic garnet from the Bardane peridotite (Western Gneiss Region of Norway), which represents one of the best-known analogue for fluid-related redox processes at sub-arc depth (Rielli *et al.*, 2017). Similarly, other studies have suggested that sulphate (anhydrite) should dominantly dissolve into metamorphic fluids released across the transition from blueschist to eclogite facies in metabasalt (e.g. Tomkins & Evans, 2015). The fO_2 of altered oceanic crust (AOC) is \sim FMQ+1 (Foley, 2011) at the trench and decreases gradually with increasing depth (below FMQ at depths corresponding to eclogite-facies conditions, e.g. Li *et al.* 2016). Very few studies have focused on in situ prograde fO_2 of subducted sediments. Tao *et al.* (2020) studied the prograde fO_2 of carbon-rich high pressure metamorphic rocks (marble, metapelite, eclogite) from the Western Tianshan subduction zone. In comparison with redox conditions of other subduction zones, Western Tianshan has the lowest oxygen fugacity (FMQ-1.9 to FMQ-2.5), but the studied compositions (5-20 vol % carbonation) are different from our starting pelite. Our experiments have mostly explored moderately oxidized conditions in an attempt to replicate partial melting processes of subducted sediments under relatively high fO_2 conditions, but we do not exclude that more reducing conditions could prevail in such a context. Evidence from blueschists and eclogite terrains suggests that both pyrrhotite or pyrite occur in metasediments during subduction at various metamorphic grades, though pyrrhotite is more common at higher grades (e.g Brown *et al.*, 2014), via pyrite breakdown (e.g. Tomkins & Evans 2015). Our experiments doped with elemental sulphur produce an assemblage saturated with rutile and pyrrhotite (see below), as often observed in exhumed high pressure metasediments.

Starting material

Our starting material (sample B12a) is taken from the Lesser Antilles arc in the West Indies. The rock powder used for this study is an aliquot of the pelitic sediment studied by Carpentier (2007), Carpentier *et al.* (2008) and Prouteau & Scaillet (2013), sampled in the Lower Scotland unity from the Barbados accretionary prism. The pelite has a mineralogy of quartz, clays (kaolinite, illite), K-feldspar, plagioclase and muscovite, in order of decreasing abundance. It is CaO-poor ($X_{Ca} = 0.05$) and highly peraluminous ($A/CNK = 3.72$) compared to the mean composition of global oceanic sediment analogue (GLOSS-II, Table 1), representing a chemical endmember of ocean sediment composition. Carpentier *et al.* (2008) reported its major (Table 1) and isotopic compositions. Trace elements and volatiles (H_2O , S, Cl, F and CO_2) contents were obtained by inductively coupled plasma mass spectrometry (ICP-MS, CRPG, Nancy, France) (Tables 1 and 4). Sample B12a is volatile-rich with 8.53 wt. % initial H_2O , 1.03 wt. % CO_2 , 900 ppm S, 565 ppm Cl and 560 ppm F (Table 1; 1 ppm = 1 $\mu g/g$). The ratio FeO/FeO_{total} (potentiometric dosing, CRPG, France) is 0.3 (Table 1), i.e. similar to commonly observed values for subducting terrigenous sediments (~ 0.2 ; Chester, 1990). It shows a typical terrigenous sediment trace element pattern (Fig. 1), with a clear enrichment in LILE (K, Rb, Ba, Sr), a depletion in HFSE (e.g. Nb, Ta), a low Ce/Pb ratio and highly fractionated REE.

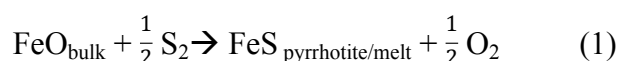
Experimental techniques

To investigate the role of sulphur on phase relationships and compositions in the pelitic system, 1 to 2.1 wt. % elemental sulphur was added to the powdered pelite, following the protocol of Prouteau & Scaillet (2013). We are interested in a process whereby the sulphur is

mainly brought to the system via the ingress of hydrous fluids released by dewatering of subducted lithologies. Indeed, using either pyrrhotite or anhydrite (as commonly practiced) as a source of S in experimental charges would imply that slab-derived fluids contain S and Fe (or Ca) in broadly equal molar proportions, which would change the bulk composition. An additional experiment has been performed at 900°C using a diluted H₂SO₄ solution (5 mol/L) as a source of fluid, following the protocol of Zajacz (2015). The 1 wt. % S_{in} run contains ~ 15 wt. % H₂O, and we add also ~ 8 wt. % H₂O to the S-undoped control sample to homogenize total water content. With this experimental strategy, it can be expected that S is dominantly present as SO₂ in any excess fluid (Binder & Keppler, 2011; Borisova *et al.*, 2014; Zajacz, 2015).

Powdered, hydrous (structurally bound water only) starting material was loaded into Au capsules (outer diameter: 2.0 mm; inner diameter: 1.6 mm; length: 10 mm). On average, each experimental run contained three capsules, positioned next to each other, with 0, 1 and 2.1 wt. % S added (S_{in}, added sulphur), respectively. The pressure cell consisted of inner spacers of alumina, a graphite furnace, and an outer sleeve of talc and Pyrex. The reported pressure is nominal value. The friction coefficient for a talc-pyrex assembly is 3.6 % (McDade *et al.*, 2002). We used magnesia or boron nitride (BN) fillers (Table 2). No attempt was made to monitor fO_2 during the experiments. However, our previous work carried out using the same vessel and MgO assemblies produced pyrrhotite + anhydrite bearing charges (Prouteau & Scaillet, 2013), reflecting thus an intermediate fO_2 range for buffer reactions involving sulphide-anhydrite-garnet-clinopyroxene. In piston cylinder experiments, the final oxygen fugacity is controlled by the initial bulk Fe²⁺/Fe³⁺ (FeO/FeO_{total} = 0.3, Table 1), S⁶⁺/ΣS and C⁴⁺/ΣC of the starting material and by the intrinsic fH_2 of the furnace assembly (e.g. Holloway *et al.*, 1992; Truckenbrodt *et al.*, 1997; Kägi *et al.*, 2005). In S-free systems, the intrinsic fH_2 of magnesia or boron nitride-talc-Pyrex assemblies imposes redox conditions

at or below NNO, with MgO assemblies imposing more oxidizing conditions, around NNO+1 (e.g. Kägi *et al.*, 2005; Sisson *et al.*, 2005; Prouteau & Scaillet, 2013). Runs at 800°C and 1000°C were performed with BN assemblies and thus at an fO_2 below NNO (in S-undoped charges), while runs at 750°C, 850°C, and 900°C were done with MgO fillers, resulting in a fO_2 above NNO (in S-undoped charges). The introduction of S will rise the fO_2 by virtue of the following reaction:



This increase in fO_2 is not quantifiable, but we assume that the relative difference in fO_2 imposed by the use of different assemblies remains. The assemblage pyrrhotite + rutile (see below), present in all our elemental S-doped experiments, is consistent with a large range of fO_2 , from NNO+1 (provided that $\log fS_2 > \sim +2$, Supplementary Data 7) to highly reducing conditions (green area in Supplementary Data 7). As fS_2 is unknown, this assemblage provides therefore few constraints on the fO_2 of our experiments. The run performed with H_2SO_4 , i.e. with a very high starting $S^{6+}/\Sigma S$, yielded higher fO_2 ($> \text{NNO}+2$), in agreement with run products characteristics (rutile + magnetite, Supplementary Data 7).

Experiments were carried out in a half-inch, end-loaded, piston-cylinder apparatus (ISTO, Orléans, France) at a nominal pressure of 3 GPa and within the temperature range 750-1000°C. Temperature was controlled using B-type thermocouple ($Pt_{94}Rh_6/Pt_{70}Rh_{30}$; accuracy: $\pm 10^\circ\text{C}$) separated from the capsules by a 0.5 mm thick alumina wafer. Runs lasted 4-10 days, depending on temperature. The approach toward equilibrium was checked by performing two experiments with different durations (90 to 196 h) at 800°C (Table 2).

Experiments were quenched isobarically by adjusting the pressure during cooling. After quenching, the capsules were reweighed, showing no significant weight loss after the experiments. The entire capsules were mounted in epoxy and carefully polished with abrasive

paper under water. Further epoxy is then added to avoid loss of the run products. The final polishing was performed with a series of diamond pastes.

Analytical methods

Run products were characterized using scanning electron microscopy (SEM, ISTO/BRGM, Orléans, France), electron microprobe (EMP, Cameca SX Five, ISTO/BRGM, Orléans) and laser-ablation inductively coupled plasma mass spectrometry (LA-ICP-MS, LMV, Clermont-Ferrand, France and IRAMAT/ISTO/CEMHTI, Orléans, France). Additional observation with a cathodoluminescence (CL) microscope (beam current 120 nA during 20 s) was aimed to identify μm -sized accessory phases (monazite and zircon). Finally, Raman spectroscopy has led to the identification of crystallized carbonate phases ($< \mu\text{size}$) in high temperature runs (see Supplementary Data 3).

Major elements of both glasses and crystals were determined by electron microprobe with the following analytical conditions: accelerating voltage of 15 kV, sample current of 6 nA, counting time of 10 s on peak, with either a defocused (glass, $8\mu\text{m}$) or focused (crystals) beam. The measured alkali concentrations of the glasses were corrected by using secondary standards of rhyolitic compositions with known alkali and water contents (Scaillet *et al.*, 1995). The water contents of the experimental glasses were determined by using the summation deficit to 100 % of the EMP analyses method (Devine *et al.*, 1995), with four rhyolitic standard glasses containing up to 6.4 wt. % H_2O , as determined by Karl Fisher titration or ion-microprobe analysis (Scaillet *et al.*, 1999; Martel *et al.*, 1998). Owing to potential volatile exsolution during quench, we also estimated the amount of dissolved H_2O by mass balance (Table 3). The sulphur content of the glasses was determined using an accelerating voltage of 15 kV, a current of 50 nA, counting time of 60 s and a defocused beam

of 10 μm . We used three S-bearing dacitic glass standards with sulphur contents determined by wet chemistry (Clemente *et al.*, 2004). Pyrrhotites were analysed for four experiments (900 and 1000°C; 1 and 2.1 wt. % S_{in}) with a focused beam (20 kV, 20 nA) and a counting time of 30 seconds for each element (S, Fe).

Wherever possible owing to the phase sizes, trace element contents of glasses and minerals were obtained by laser-ablation ICP-MS. The concentrations of alkalis (Li, Rb), alkaline earth (Be, Sr, Ba), lanthanides (La, Ce, Nd, Sm, Eu, Dy, Yb), Y, actinides (Th, U), Pb, HFSE (Nb, Ta, Zr, Hf) and B of glasses and silicate minerals were determined using a pulsed 193 nm EXCIMER laser (Resonetics M-50E) coupled to an Agilent 7500 ICP-MS (LMV, Clermont-Ferrand, France). Additional analyses of Pb in glasses and sulphides were carried out with a pulsed 193 nm EXCIMER laser coupled to a Thermo Element XR ICP-MS (IRAMAT/ISTO/CEMHTI, Orléans, France). The following settings were used: a 2.8 $\text{J}\cdot\text{cm}^{-2}$ fluence at a repetition rate of 2 Hz and a spot size of 20-26 μm for glasses, 15-20 μm for silicate minerals and 11-15 μm for sulphides. For each analysis, data were collected for a total time of 90 seconds, including gas (argon) background of 25 seconds. The synthetic glass NIST 610 was used for external calibration for silicate phases and MASS-1 for sulphides. NIST 612 and a BCR-2G glasses (Jochum *et al.*, 2005; Jacob, 2006) were used as secondary standards and the measured compositions are given in Supplementary Data 6. For silicate phases, we used concentration of aluminium (^{27}Al) as internal standard. To determine the partitioning of Pb between sulphides and silicate glasses, the concentration of iron (^{57}Fe) was used as an internal standard. Data were reduced using the GLITTER software and mineral inclusions were excluded via inspection of a count-rate versus time diagram. The average analytical standard error (1 sigma) was < 5% for most trace elements except for Hf (~ 7%), Yb and Ta (~ 10 %), Be (~ 18%) and B (~ 24%).

Finally, micro-Raman spectra (Supplementary Data 3) were acquired on a Horiba Jobin-Yvon LabRam© HR800 Evolution spectrometer (Laboratoire de Planétologie et de Géodynamique, Nantes, France). The spectrometer is equipped with a solid-state laser diode operating at 532 nm and with a 1800 grooves/mm grating allowing a spectral resolution on the order of $\sim 0.4 \text{ cm}^{-1}$. Analyses were performed in confocal mode (hole = 75 μm) using a x100 Olympus objective. The studied spectral range was between 300 and 1250 cm^{-1} , covering the area of the silicate network. The spectral frequency position was calibrated using the emission lines of Ne- and Hg-lamps. The acquisition time of a given sample was typically between 5 and 10 s and 10 scans were accumulated. The output power was set to 100 mW.

EXPERIMENTAL RESULTS

Details of experimental conditions and run products are listed in Table 2 and illustrated in Fig. 2.

Time series experiment at 800°C

After 90 hours, silicate melt coexists with staurolite + quartz + biotite \pm garnet (0 wt. % S_{in}) + rutile + pyrrhotite. The proportion of biotite (phlogopite *sensu stricto*, see below) increases with increasing S_{in} . Phengite is systematically absent in these short run duration experiments, regardless S_{in} (Table 2). Garnet is present only in the S-undoped charge. Fe-staurolite is abundant (24-26 wt. %, whatever the bulk sulphur content), being present across the entire length of the charges as microcrystals (mean length = 2-3 μm ; Fig. 2b).

After 196 hours, biotite is observed only in S-doped experiments (1 and 2.1 wt. % S_{in}) as large (80-90 μm) euhedral crystals (Fig. 2d) and its proportion increases with S_{in} (Table 2). In contrast, phengite is present only in the S-undoped charge. Kyanite is the main aluminium

silicate phase (Figs 2c, 2d) and staurolite is present only in trace amounts. Garnet is identified in all charges in these long run duration experiments and its mode decreases with S_{in} (Table 2).

The main effects of an increase of run duration, at fixed S content, are therefore summarized as follows (Table 2): for the sulphur-undoped runs, longer duration promotes the crystallization of phengite whereas biotite is not stable anymore. The recent experimental study of Pichavant *et al.* (2016) shows that at low fO_2 (NNO-1.6 to -1.4) biotite is the stable mica in peraluminous melts, whereas at high fO_2 (NNO+1 to +3) it is replaced by muscovite. On this basis, we suggest that the observed phengite to biotite phase change reflects a higher fO_2 in 196 hours run duration experiment (through H_2 -mediated redox reactions). In sulphur-doped experiments, phengite is never stable (see later) and the proportion of biotite systematically increases with increasing run duration (from 3.4 to 6.6 wt. % for 1 wt. % S_{in} and from 4.9 to 10.6 wt. % for 2.1 wt. % S_{in} , Table 2).

Nucleation and growth of garnet is promoted in long run duration experiments (Table 2). In contrast, staurolite is replaced by kyanite or kyanite + garnet in long duration runs. This observation is consistent with recent experimental studies, which suggest that staurolite nucleates metastably at high pressure (3 GPa) in sedimentary (Skora & Blundy, 2010) or basaltic (Carter *et al.*, 2015) systems. Pioneer studies on the stability of staurolite in pelitic system have suggested indeed that almandine+kyanite is stable relative to Fe-rich staurolite at eclogite-facies conditions (e.g. Richardson, 1968; Ganguly, 1972; Ballèvre *et al.*, 1989). Staurolite presence is not consistent with natural phase assemblages or thermodynamic grids of high-pressure, low-temperature metapelites (e.g. Yardley, 1977; Powell & Holland, 1990, Wei & Powell, 2003; Smye *et al.*, 2010) or other experimental studies (e.g. Johnson & Plank, 1999; Hermann & Spandler, 2008).

We thus conclude that staurolite is metastable relative to garnet and kyanite, and that long run durations are necessary to reach steady state in the lower temperature range. Based on these tests, we favor the long run duration experiments for 800°C and only their results will be presented and discussed in the following sections. Below 900°C, the melting experiments performed were generally held at pressure and temperature for more than 7 days. However, at 750°C, despite a long run duration (> 10 days), staurolite remains the main aluminosilicate phase (kyanite is only identified in trace amounts at 2.1 wt. % S_{in} , see Table 2 and Figs 2a, 3, 4). The increase in run durations could lead to the desiccation of the charge, following a drastic loss of H_2 through the sleeve and, therefore, could induce a significant change of fO_2 and H_2O content during the experiment. If at 750°C staurolite is also metastable, then experiments at 800°C suggest that it should be replaced by kyanite and garnet. While the former phase has no practical consequence on trace element behaviour, the same is not true for garnet. The interpretation of analytical results discussed below should therefore bear in mind that garnet proportions in the 750°C charges are probably minimum values.

General observations

Inter-experiment variation as a function of run conditions are consistent, considering the wide range of variables in our experiments. No systematic variations in most mineral or melt compositions (within analytical error) were found across the length of experimental charges. Limited mineral zoning was identified only in garnet, especially at low temperature (Supplementary Data 1). Most crystals are euhedral except some xenomorphic quartz at the bottom end of capsule at or below 800°C. No mineral quench phases have been observed within experimentally produced glass. Hydrous silicate glass (quench liquid) is present in all experimental charges. Glass occurs evenly throughout charges, although some local

concentrations are apparent near the tip of the capsule. At 750 °C and, to a lesser extent, 800°C, charges show two spatially segregated regions of phase crystallization, with a region dominated by phengite (\pm biotite) and quartz, while the others, near the tip of the capsules, consist generally of garnet (\pm kyanite) and hydrous, vesiculated glass. These phase segregations, already observed in previous studies (e.g. Schmidt & Ulmer, 2004; Li & Hermann, 2015), could represent the segregation of reactants and products during melting. Small, micron-sized vesicles, free of crystal inclusions, occur in quenched glasses of low temperature experiments (\leq 850°C). The abundance of vesicles decreases with increasing temperature (Figs 2a, 2c, 2e). We interpret these as resulting from fluid exsolution upon quench. At 900 and 1000 °C, the glass displays a clean texture, free of any bubbles, supporting the idea that our run products have been cooled at a rate fast enough to avoid large quench effects (e.g. Hermann & Spandler, 2008). Therefore we propose that the pelite experiments with 8.5 wt. % structurally bound H₂O are water-undersaturated and fully quenchable to a glass. For the two experiments with added H₂O or H₂SO₄, PEL68h and PEL69h respectively (Table 2), run products show a vesicular glassy matrix with, in addition to micron-sized vesicles, a population of larger vesicles probably arising from vapour-saturated conditions at high P-T conditions. Phase segregations (quartz + minor staurolite) have been observed near the tip of the PEL69h capsule.

Charges are dominated by the assemblage kyanite \pm garnet \pm quartz \pm phengite and/or biotite \pm orthopyroxene and peraluminous to metaluminous granitic melts (Table 2, Fig. 2). Identified minor phases include rutile, Ti-magnetite, monazite, zircon, pyrrhotite and submicron-sized Cl-rich and carbonated phases. As stated in the previous section, microcrystals ($<$ 5 μ m) of staurolite persist at 750°C and, to a lesser extent, 800°C, either as isolated phases or as inclusion in quartz and micas, from major to trace amounts, instead of, or together with, kyanite.

For experiments performed at or above 850°C, a crystalline, micron-sized (<5 µm) Cl-rich phase has been identified (Supplementary Data 3). Semi-quantitative analysis (Energy dispersive X-ray mapping analysis; detector EDS QUANTAX, ISTO) shows that this phase is Na₂O- (~ 35 wt. % at 900°C) and Cl-rich (~ 40 wt. %) with some K₂O and traces of Al₂O₃, SiO₂, CaO and MgO. We interpret the Cl bearing phase as (minor) quench product, since the bulk Cl content of the starting material (565 ppm) is well below brine saturation values of common silicate melts (Webster *et al.*, 2015) and the applied pressure is well above the crest of the H₂O-NaCl solvus in a P-X_{NaCl-H₂O} projection (ca 0.2 GPa). Submicron-size carbonated phases have been unambiguously identified by Raman spectroscopy (Supplementary Data 3) above 850 °C (Table 2).

Phase proportions

Details on run products and phase proportions, calculated by mass balance (Albarède, 1995), are listed in Table 2 and illustrated in Fig. 3. Isobaric phase relations are reported as a function of S addition (S_{in}) in Fig. 4. Phase boundaries (Fig. 4) are drawn for melting experiments doped with elemental S, with BN or MgO fillers. Despite the range of fO_2 induced by these various assemblies, a consistent picture emerges in Figs 3 and 4.

Effect of temperature at fixed S_{in}

For sulphur-undoped experiments (8.53 wt. % bound H₂O), glass is the most abundant phase. Melt proportion increases abruptly with temperature until 850 °C and more gently beyond this temperature. At 750°C, staurolite (<5 µm) is abundant (19 wt. %) and probably metastable as discussed above. Phengite makes up > 20 % of the charge at 750°C, appearing as euhedral to

sub-euhedral (10-20 μm) crystals heterogeneously dispersed in the charge (Fig. 3). At 800°C, its abundance decreases to a few percent. Biotite is not stable in the conditions investigated. Garnet has a euhedral shape, with a grain size increasing from $\sim 15 \mu\text{m}$ at 750°C to $\sim 45 \mu\text{m}$ at 1000°C. Micron-sized inclusions in garnet are sporadic (kyanite, rutile, and pyrrhotite). Garnet abundance increases up to 850°C and then decreases significantly (Fig. 3). The proportion of kyanite is roughly constant in the studied melting interval. Quartz abundance decreases sharply until 850°C; at 900°C, only trace amounts of SiO_2 are detected. Finally, charges are saturated in rutile, whose size increases with temperature. They are saturated in pyrrhotite in the entire melting interval, and with monazite and zircon at 750-800°C. Experiment PEL68h, performed at 900°C with $\sim 15 \text{ wt. \%}$ total H_2O yielded the same run products as PEL9 (900 °C, 8.53 wt. % bound H_2O), lacking pyrrhotite (Table 2).

For the elemental S-doped pelite, at fixed S_{in} (1 wt. % and 2.1 wt. %), melt, garnet and quartz exhibit the same behaviour as observed in S-undoped charges with increasing temperature: melt proportion increases abruptly with temperature until 850°C and more gently beyond (Fig. 3); garnet proportion increases from 750 to 850°C and then decreases from 850 to 1000°C. Quartz abundance decreases sharply until 850°C. Modal kyanite decreases slightly with increasing temperature at fixed S content. Phengite is not stable beyond 750°C. Modal biotite increases in the 750-800°C interval and is not stable at higher temperature. Biotite forms euhedral grains ranging from a few microns up to 90 μm for the higher temperature charges. Orthopyroxene trend is less clear, but its proportion decreases with increasing temperature (Table 2). The proportion of pyrrhotite increases from 750 to 800°C, and then appears weakly correlated with temperature (Table 2). The proportion of pyrrhotite reaches 4-5 wt. % in the less oxidizing charges (800 and 1000°C), with $S_{\text{in}} = 2.1 \text{ wt. \%}$. (Table 2).

The H_2SO_4 doped experiment PEL69h, performed at 900°C with $\sim 15 \text{ wt. \%}$ total H_2O (1 wt. % S_{in}), is saturated with both garnet and kyanite and yielded roughly the same run

products as PEL13 (Table 2). Mass balance indicates ~ 1 wt. % of titanomagnetite, whereas only a few crystals of rutile, systematically included in titanomagnetite, have been detected (0.4 wt. %). Pyrrhotite is only present in trace amount. Quartz segregations, isolated at the base of the capsule, are excluded from the mass balance calculation. This calculation yields high residual and suggests the presence of a Ca-bearing phase (anhydrite) which might have gone undetected in the run product (or removed during polishing). The higher standard deviation of SiO₂ indicates that the glass in PEL69h is less homogeneous in major elements than all other charges, hence mass balance constraints are less reliable.

Effect of S_{in} at fixed temperature

At fixed T, adding elemental S at a percent level has a profound effect on phase relationships (Figs 3, 4). Biotite, not stable in S-undoped runs, crystallizes together with (750°C), or in lieu of (800°C), phengite, and its modal abundance increases with S_{in} (Figs 3a, 3b, 4). Conversely, phengite mode decreases with S_{in} (Figs 3a, 3b). The proportion of kyanite (or staurolite at 750°C) increases with S_{in}, at fixed T, together with that of quartz below 900°C (except at 750°C between 0 and 1 wt. % S_{in}). Garnet proportion strongly decreases with increasing sulphur content. In 2.1 wt. % S_{in} charges, only a few crystals are detected at low T and garnet is not stable beyond 850°C. Garnet size increases with S_{in}, while kyanite size decreases. Orthopyroxene crystallizes together with (850°C), or instead of (900 °C), garnet in the 2.1 wt. % S_{in} charges. At fixed T, the modal abundance of pyrrhotite increases markedly with sulphur content (Table 2).

At 750°C, the proportion of melt, saturated with phengite, increases with S content. An opposite effect is observed at 800°C, in the stability field of biotite. At T ≥ 850°C, melt

proportion increases slightly with sulphur content (e.g. from 68 wt. % (0 wt. % S_{in}) to 73 wt. % (2.1 wt. % S_{in}) at 900 °C; Table 2 and Fig. 3).

PHASE COMPOSITIONS

Major element chemistry

Major element compositions of hydrous silicate melts are listed in Table 3. Major element compositions of minerals are given in Supplementary Data 1. Short run duration experiments at 800°C are not presented. Experimental glasses and silicate minerals are relatively homogeneous, with standard deviations (σ) < 10 % relative, with the exception of zoned garnet. Phase compositions are controlled predominantly by temperature, H₂O and bulk sulphur contents. In spite of differences in oxygen fugacity for experiments doped in elementary sulphur performed at 750/850/900°C (magnesia filler) and 800/1000°C (BN filler), this has no detectable effect on major element chemistry.

Garnet

Garnet is present in all experimental charges except those doped with 2.1 wt. % S_{in} at 900 and 1000°C. Zoned garnet cores are characterized by higher Ti, Fe, Mn (p.f.u.) and lower Mg and Ca contents than in the rim (Supplementary Data 1). The following discussion is based on rim compositions, which are interpreted to be in equilibrium with other phases. Garnets have high pyrope (30-56 %) and almandine (36-60 %) contents with significant grossular (0.7 to 10 %) whereas spessartine remains low (0.3 to 5 %). They are characterized by low Ca contents (0.02 to 0.28, pfu; Fig. 5c) compared to high pressure synthetic garnet produced in previous

experiments in pelitic system (e.g. Hermann & Spandler, 2008), reflecting the very low calcium content of our starting composition. Garnet trends reflect high-pressure equilibrium and show systematic changes with temperature and/or S contents.

The most significant feature is an increase of pyrope content and X_{Mg} ($X_{Mg} = Mg/(Fe_T + Mg)$, in moles), and a decrease in Ca and grossular contents with increasing temperature, for a given S_{in} (Figs 5a, 5b, 5c). Ti (p.f.u.) and Al (p.f.u.) values increase between 750 and 850 °C, in the stability field of phengite, and then decrease beyond 850°C. Si (p.f.u.) contents slightly increase with temperature.

With increasing H_2O_{in} (at fixed T and S_{in} ; Supplementary Data 1), Fe (p.f.u.) contents strongly increase while Si and Al (p.f.u.) contents decrease, together with X_{Mg} (Fig. 5b). At fixed T and H_2O_{in} , the X_{Mg} increases drastically with the sulphur content: e.g. from 0.37 in a sulphur-undoped system at 850°C to 0.59 with 2.1 wt. % S_{in} (Fig. 5b). Pyrope, grossular and spessartine components increase with the addition of elemental sulphur, at fixed temperature, whereas almandine component decreases (Figs 5a, 5c). This trend is less clear for the experiment doped with H_2SO_4 (Fig. 5a).

Orthopyroxene

Orthopyroxene is present only in two charges with 2.1 wt. % S_{in} at 850 and 900°C. It is an enstatite with composition $En_{76-77} Fe_{23-24}$ (Supplementary Data 1). The wollastonite component does not exceed 0.2 %. Orthopyroxene is characterized by high Al_2O_3 contents (~ 8-9 wt. % Al_2O_3) and X_{Mg} (~ 0.77). The composition shows no significant variation with varying temperature (Supplementary Data 1).

Phengite

Only the 750°C and the sulphur-undoped 800°C experiments crystallized phengite. Phengite is aluminous (26-30 wt. %) and Na₂O rich (8-9 wt. %) (Supplementary Data 1). TiO₂ content is low (< 1.2 wt. %) and increases with increasing temperature in S-undoped experiments. Structural formulae, calculated on the basis of 11 O, yield Si (p.f.u.) above 3.2. The Si content decreases with increasing temperature for S-undoped charges (Fig. 6a). Both Ti and Si (p.f.u.) trends with temperature are consistent with experiments in chemically comparable systems (e.g. Hermann & Spandler, 2008). At 750 °C, Si content increases with sulphur addition (Fig. 6a). All phengites contain Mg+Fe > Si-3 (p.f.u.), indicating that there is a biotite component present, which increases with T for S-undoped charges. With increasing temperature, Fe, Mn and Mg (p.f.u.) contents and X_{Mg} increase while Na and Al (p.f.u.) contents decrease. At 750°C, Mg (p.f.u.) content increases and Al (p.f.u.) content decreases. At 750°C, X_{Mg} is significantly higher for the 2.1 wt. % S_{in} charge (Fig. 6c).

Biotite

Biotite (*sensu lato*) is present at 750 and 800°C in the most sulphur-rich charges (1 and 2.1 wt. % S_{in}). At fixed S, the TiO₂ contents (1.4-2 wt. %, Supplementary Data 1) increases with temperature together with MgO, whereas the FeO and Na₂O contents decrease. Biotite is aluminous (18.2-20.7 wt. % Al₂O₃) with high MgO contents (13-16 wt. %). Biotite is a phlogopite (*sensu stricto*) following the division of Deer *et al.* (1962) : it is characterized by relatively high X_{Mg} (0.69-0.82; Fig. 6d), which compares well with the X_{Mg} range of biotite produced in sulphur-free experiments in similar systems (e.g. biotite X_{Mg} between 0.71 and 0.78 at 2-5GPa, 750-900°C, Hermann & Spandler, 2008; Fig. 6d). For a given temperature,

X_{Mg} increases strongly with sulphur addition. X_{Mg} increases with temperature, for a given S_{in} . With 1 wt. % sulphur added, this effect is, however, less clear (Fig. 6d).

Other phases

Staurolite occurs as small grains ($< 5 \mu\text{m}$) in all 750°C charges and in the short run duration experiment performed at 800 °C (Table 2). Because of the small grain size, microprobe analysis was difficult. We have successfully analysed Fe-rich staurolite produced at 900°C in H₂O-doped experiments (Supplementary Data 1).

At low temperature ($< 900 \text{ }^\circ\text{C}$), the small size of sulphide (whatever the sulphur content), an ubiquitous minor phase, prevents its accurate chemical characterization.

Sulphides produced at 900 and 1000°C are pyrrhotite with FeO contents of 57-58 wt. % and S contents of 40.5-41.7 wt. % (Supplementary Data 1).

Monazite, ubiquitous at 750 and 800°C, is Ce-rich and may incorporate some sulphur in S-doped experiments, according to chemical mapping (Supplementary Data 3).

Glass

Table 3 presents the glass analyses normalized to 100 % on an anhydrous basis. The water contents of the quenched glasses estimated by the by-difference method fall in the range 6.7-14 wt. % (Table 3), and increase roughly with temperature. The presence of micron-sized bubbles in the lowest temperature charges ($\leq 850^\circ\text{C}$) or in those H₂O-doped suggests, however, that such estimates are minima. In the 750-850°C temperature interval, the full range of mass-balance estimates of dissolved H₂O is 13-36 wt. %, the highest content (at 750°C) being close to the H₂O solubility determined at 4 GPa (Kessel *et al.*, 2005b). These

values are in some cases considerably higher than that given by the by-difference method, especially at low temperatures (e.g. at 750 °C, S-undoped: by-difference = 7.2 wt. %; mass-balance = 36.4 wt. %, Table 3), corroborating the fact that some water may have been exsolved during quenching. The same feature is observed for the H₂O or H₂O+H₂SO₄ doped charges (Table 3). In contrast, for the S-undoped or elemental sulphur-doped experiments performed at 900 and 1000°C, melt water contents determined by the two methods fall within the same range (11.4-14 wt. %), suggesting few if any quenched effects for these experimental conditions.

Experimental glasses have silicic compositions (SiO₂ contents between 74 and 79 wt. %, on an anhydrous basis), becoming increasingly peraluminous (molar Al>Na+K+2Ca) with temperature, all charges defining a single common trend (Fig. 7a). At 750°C, the S-undoped charge produces a metaluminous glass with an aluminium saturation index (ASI or A/CNK = Al/Na+K+2Ca) of ~ 0.94 while glasses in S-doped charges are peraluminous (Fig. 7a, Table 3). The TiO₂ contents are < 1 wt. %, increasing steadily from 750 to 1000°C, reflecting enhanced rutile solubilities at higher temperatures (Table 3, Fig. 7b) (e.g. Ryerson & Watson, 1987; Klimm *et al.*, 2008). Similarly, both FeO and MgO contents increase with increasing temperature, with X_{Mg} in the range 0.36-0.67. At a fixed temperature, FeO decreases whereas MgO increases with the addition of elemental sulphur (Table 3). Therefore, X_{Mg} decreases with increasing temperature at a fixed S_{in}, but this trend is reversed for the most S-doped charges, especially beyond the stability field of garnet (Fig. 7c). In contrast, X_{Mg} increases strongly with the addition of sulphur at a fixed temperature (Fig. 7c).

The CaO content is uniformly low, < 1.5 wt. % (Table 3), decreasing weakly with increasing temperature and increasing with sulphur content (Table 3). The K₂O content ranges between ~ 2 and 4 wt. % (Fig. 7e). With increasing T, first K₂O increases, peaking at T ~ 800°C, (Fig. 7e), then decreases. The first part reflects the progressive consumption of micas,

while the second part a simple dilution effect once micas are exhausted. Na_2O decreases sharply with increasing temperature and, though less clearly, with S_{in} (Fig. 7d). Consequently, the low temperature glasses are characterized by $\text{K}_2\text{O}/\text{Na}_2\text{O}$ ratios lower than that of the starting composition (Fig. 7f). With increasing temperature, the ratio $\text{K}_2\text{O}/\text{Na}_2\text{O}$ increases. At fixed T above 850°C , Na_2O and $\text{K}_2\text{O}/\text{Na}_2\text{O}$ ratios increase with the addition of elemental sulphur (Table 3, Fig. 7f). The glass produced at 900°C with 15 wt. % H_2O and 1 wt. % S_{in} has a significantly higher Na_2O content than the H_2O -undoped experiments performed at the same P-T/ S_{in} conditions (Fig. 7d).

In the Ab-An-Or diagram (Fig. 7g), melt compositions have low anorthite contents, a reflection of their low Ca contents, and trend away from the trondhjemite field towards the granite field as temperature increases, as observed for sulphur-free synthetic pelitic compositions at > 2.5 GPa (e.g. Hermann & Spandler, 2008). At 750°C , increasing sulphur content in the system increases the normative An content (Fig. 7g), while at higher T S-free and S-bearing charges define a single common trend.

Melt sulphur contents

All charges are pyrrhotite-saturated, except PEL68h (15 wt. % H_2O , 900 ppm S). Anhydrite, in addition of pyrrhotite, is suspected in experiment PEL69h (doped with H_2SO_4) but not demonstrated unequivocally.

The S contents in experimental glasses range from 72 to 3507 ppm (Table 3), increasing gently with temperature, other parameters being equal (Fig. 8a), as observed in previous studies (e.g. Carroll & Rutherford, 1987; Luhr, 1990). At fixed T, melt sulphur content increases with S_{in} for a given filler and protocol (elemental S or H_2SO_4 addition) (Table 3, Figs 8a, 8b).. At 1000°C , this effect is, however, barely detectable and melt sulphur

contents are uniformly low (~220-260 ppm, Table 3, Fig. 8a). The glass in the charge PEL69h synthesized at 3 GPa and 900°C, with 1 wt. % S added as H₂SO₄, has a sulphur content of ~3507 ppm (Fig. 8b), which is four times higher than that annealed with 1 wt. % elemental sulphur (~850 ppm). This is thought to reflect higher oxidizing conditions in PEL69h, arising from the use of fully oxidized S along with elevated water contents.

Unlike in basaltic melts, melt sulphur contents are not correlated with melt FeO contents (Table 3), as already shown previously (e.g. Clemente *et al.*, 2004; Prouteau & Scaillet, 2013). Finally, we note that the peraluminous glasses produced here have sulphur contents lower by a factor of 1.5-2 relative to trondhjemitic glasses produced at the same conditions in the basaltic system (melts saturated in pyrrhotite and anhydrite) (Fig. 8a; Prouteau & Scaillet, 2013), in line with the observation that high alkali content enhances sulphur solubility in felsic melts (Scaillet & Macdonald, 2006).

Trace element chemistry

H₂O± H₂SO₄-doped charges have not been analysed for trace elements, as glass pools were too small for successful analysis. Glasses in other charges are relatively homogeneous in trace element composition, as evidenced by multiple analyses (5-6) showing standard deviations of typically ≤ 10 %. Mineral phases proved to be more difficult to analyse, due to their small size, crystal habit or inclusions, and core-to rim trace element zoning could not be determined. Standard deviations are typically around 10 %, but can reach 50 % for some elements (Yb in garnet, Pb in sulphide). The micron-size monazite, rutile, zircon were too small to be reliably analysed by LA-ICP-MS.

In experiments where all host phases were analysed, mass balance for trace elements was good generally, and no evidence for “open system” behaviour was observed, except for

Pb in high temperature (> 850 °C) experiments, for which lead contamination, probably through the lead sheet surrounding the talc-pyrex assembly, is suspected.

Trace element composition of minerals

Garnet is the main host for Y and HREE (Heavy Rare Earth Elements) and is slightly enriched in Li, actinides (Th, U), Zr, Hf and MREE (Supplementary Data 2). LREE, MREE, Zr and Hf contents decrease in garnet with addition of S. Orthopyroxene is poor in trace elements but contains up to 61 ppm lithium (Supplementary Data 2). Micas are the main host for Rb and Ba. Phengite is also enriched in Li (30-60 ppm), B (40-60 ppm), Nb and Pb (Supplementary Data 2). B, La, Ce, Pb and Th contents increase in phengite with addition of S at fixed T. Biotite, produced in S-doped experiments (1 and 2.1 wt. % S_{in}), is the second major host for Rb and Ba, with Ba contents lower than in phengite (1500-2200 ppm in phengite vs. 700-1300 ppm in biotite; Supplementary Data 2). Biotite is enriched in Li (50-120 ppm), B (up to 120 ppm) and Pb (Supplementary Data 2). Sulphides have low Pb contents (< 25 ppm; Supplementary Data 2). Semi-quantitative analyses of monazite (Supplementary Data 3) suggest that it is Ce-rich in S-undoped experiments and that the addition of S decreases LREE (La, Ce, Nd) and P contents and increases Ca and S contents (so-called “anhydrite-celestine” substitution, see Chakhmouradian & Mitchell, 1999; Krenn *et al.*, 2011).

Trace element composition of quenched glasses

The trace element compositions of quenched glasses are given in Table 4. The primitive mantle (McDonough & Sun, 1995) normalized multi-element plots (Fig. 9) illustrate that the

experimental glasses display numerous features typical of arc magmas: fractionated REE pattern, negative anomalies in HFSE (Nb, Ta, Ti and Zr to a lesser extent), selective enrichment in alkalis, earth alkalis, light elements and strong positive Pb anomalies. This geochemical pattern mimics the overall characteristics of the starting sediment, suggesting that high pressure melting can preserve this source signature.

In detail, with increasing temperature (and degree of partial melting), at fixed total S content, the concentration of light elements (Li, Be, B) decreases, together with Sr contents, due to progressive dilution as the melt proportion increases (Figs 9b, 9c). Rb and Ba mimic the behaviour of K_2O : their concentrations first increase with temperature and then decrease upon micas breakdown (Fig. 9d). HFSE (Nb, Ta, Zr, Hf) contents increase from 750°C to 1000°C, owing to the increase in solubility of rutile and zircon with temperature (Fig. 9e). Zr/Hf ratios are sub-chondritic (< 37.1 ; McDonough & Sun, 1995) except in 1000°C garnet-free charges (Zr/Hf = 41.7). Similarly, Nb/Ta ratios are systematically sub-chondritic (< 17.6 , McDonough & Sun, 1995) and increase with increasing temperature (e.g. Nb/Ta increases in the S-undoped experiments from 3.1 to 16.4 with temperature increasing from 750°C to 900°C, Table 4). Pb concentrations decrease from 750 to 850°C (e.g. in the S-undoped experiments, Pb contents decreases from 63.5 ppm to 53.6 ppm with temperature increasing from 750°C to 850°C), with no clear trend at higher temperature (Table 4). Finally, LREE and Th contents increase up to 800-850°C and then decrease once monazite is exhausted from the residue (Fig. 9f).

At fixed T, adding S leads to a decrease of Rb, Ba and Sr contents in melts while HFSE (Nb, Ta, Zr) contents increase. MREE (Sm, Eu), Y and HREE (Dy, Yb) contents strongly increase in the melt (Fig. 9g) while garnet is progressively destabilised with the addition of sulphur.

Mineral-melt partition coefficients

All mineral-melt partition coefficients are calculated using raw trace element compositions of hydrous quenched glasses, without taking into account possible fluid exsolution on quenching. Mineral-melt partition coefficients are plotted for a range of trace elements in Fig. 10 (Li, Be, B, LILE, HFSE, actinides, Pb, Y, REE). The partition coefficients ($D^{\text{solid/melt}}$) in garnet, orthopyroxene, micas and sulphide are listed in Tables 5, 6, 7 and 8, respectively.

Garnet. Partition coefficients ($D^{\text{Grt/melt}}$, Fig. 10a) generally agree well with previous determinations at similar conditions (Klimm *et al.*, 2008; Skora & Blundy, 2010). HREE and Y are systematically compatible in garnet, whatever the temperature and sulphur content (Fig. 10a). In general, temperature influences the partition coefficients, at fixed S, with $D^{\text{Grt/melt}}$ decreasing with increasing temperature (and decreasing $X_{\text{grossular}}$), consistent with previous studies (van Westrenen *et al.*, 2001; Skora & Blundy, 2010). For low temperature conditions ($T \leq 850^\circ\text{C}$, with $X_{\text{grossular}}$ between 1.8 and 10 %), MREE (Sm, Eu), Ti and Zr are compatible in garnet except for high X_{Mg} garnet synthesized in PEL79 (850°C ; 2.1 wt. % S_{in}). For experiments performed at 900°C , Eu, Ti and Zr are compatible in garnet. When S content increases (T fixed), $D^{\text{Grt/melt}}$ for Zr, Hf, MREE, Y and HREE decrease. Incompatible elements with $D^{\text{Grt/melt}} < 1$ are Li, Th, U, Nb, Ce and Pb. The most incompatible elements, with $D^{\text{Grt/melt}} < 0.03$, at all temperatures and sulphur contents, are La and LILE (Rb, Ba, Sr). Garnet strongly fractionates LREE and LILE from HREE and further causes small fractionation by preferring Zr over Hf ($D_{\text{Zr}}/D_{\text{Hf}} \sim 1.3-1.9$) and U over Th ($D_{\text{U}}/D_{\text{Th}} = 1.1-6.7$). $D_{\text{Zr}}/D_{\text{Hf}}$ are inversely correlated to experimental temperature, and therefore decrease with $X_{\text{grossular}}$. Conversely, $D_{\text{U}}/D_{\text{Th}}$ increases with increasing temperature and decreasing $X_{\text{grossular}}$, consistent with Klimm *et al.* (2008) and Skora & Blundy (2010) results. Therefore, garnet crystallizing in Ca-poor sediments can efficiently fractionate U and Th, inducing a selective enrichment of

Th in the corresponding melt, in contrast to what is observed for Ca-rich systems (e.g. in MORB, Klimm *et al.*, 2008).

Orthopyroxene. Partition coefficients ($D^{\text{Opx/melt}}$) for two experiments are presented in Fig. 10b. $D^{\text{Opx/melt}}$ are systematically < 1 . The less incompatible elements, with $D^{\text{Opx/melt}} > 0.1$, are Li, Be, Nb, Ta, Ti, Dy, Y and Yb.

Phengite. Partition coefficients ($D^{\text{Ph/melt}}$) from three experiments (PEL71, PEL72 and PEL50) are shown in Fig. 10c. Elements with $D^{\text{Ph/melt}}$ values around 1-10 include Rb, Ba, Nb and Ti. $D^{\text{Ph/melt}}$ for Li and B are < 1 . There are no published partition coefficients for light elements in phengite. However, $D_{\text{Li}}^{\text{Ph/melt}}$ (0.3-0.6) are slightly greater than $D_{\text{Li}}^{\text{muscovite/melt}}$ (0.12-0.24) determined at low pressure and temperature in peraluminous rhyolite (3 kbar, 620°C; Pichavant *et al.*, 2016). At constant temperature, $D^{\text{Ph/melt}}$ for LILE, Th, LREE and Pb increases with sulphur content. Phengite fractionates Ba from Rb ($D_{\text{Ba}} > D_{\text{Rb}}$) and U from Th ($D_{\text{U}} > D_{\text{Th}}$) (Fig. 10c).

Biotite. Partition coefficients ($D^{\text{Bt/melt}}$) for two experiments doped with 2.1 wt. % S are shown in Fig. 10d. As observed for phengite, partition coefficients for LILE (Rb, Ba) and Ti are > 1 , with $D_{\text{Rb}} > D_{\text{Ba}}$, but $D_{\text{Nb}} < 1$. As in phengite, light elements (Li, B) are incompatible ($D_{\text{Li}}^{\text{Bt/melt}} = 0.49$ to 0.65 and $D_{\text{B}}^{\text{Bt/melt}} \sim 0.05$). These low D_{Li} in biotite are in agreement with previous determinations at low pressure ($D_{\text{Li}}^{\text{Bt/melt}}$: 0.41-1.00; Pichavant *et al.*, 2016).

Sulphide. Partition coefficients for Pb are presented in Table 8. D_{Pb} are systematically below unity (0.13 to 0.54) and poorly correlated to the temperature in the range investigated, consistent with partition coefficients for similar melt compositions at lower pressures (0.5-1.5 GPa; Li & Audétat, 2015).

DISCUSSION

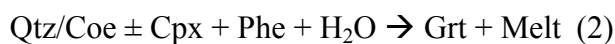
The systematic geochemical trends displayed by both glass and minerals and their coherent variations with experimental variables argues that conditions close to equilibrium were attained, with the exception of experiments performed at 750°C, in which staurolite occurrence suggests that steady state is not fully attained (see above). The wet solidus at 3 GPa has not been bracketed in our study, but our results show that, whatever the bulk sulphur content, it lies below 750°C, in agreement with previous experimental studies on similar bulk compositions (Hermann & Spandler, 2008). Below we first examine melting reactions for S- and Ca-poor oceanic metasediments by reference to previous similar works and then consider the effect of sulphur.

Phase relations and melting reactions of S- and Ca-poor pelites

Previous experiments on subducted crust have demonstrated that the transition from biotite-bearing to phengite-bearing parageneses occurs at $P \sim 2.5$ GPa not only in metapelites, but also in greywacke and K-bearing MORB (Schmidt *et al.*, 2004b; Auzanneau *et al.*, 2006; Hermann & Spandler, 2008). Our results for S-undoped experiments confirm this finding. However, the upper temperature stability for phengite in previous studies occurs above 850°C (e.g. Johnson & Plank, 1999; Skora & Blundy, 2010), whilst phengite is no more stable above 800°C in our runs (Figs 3, 4). The lower thermal stability of phengite might be due to elevated H₂O contents employed here, since it has been shown that a low H₂O content enhances the phengite stability field in high pressure pelites (up to 880-950°C at 3 GPa, for H₂O \sim 1.5 wt. %, Mann & Schmidt, 2015). A high K₂O/H₂O ratio also enhances phengite stability (e.g. Hermann & Spandler, 2008; Skora & Blundy, 2010). For instance, with a bulk K₂O/H₂O = 0.46, phengite persists to high temperature ($> 900^\circ\text{C}$) in the pelitic composition of Hermann & Spandler (2008). The low bulk K₂O/H₂O ratio (0.26) of our starting product could thus also

explain the low temperature of phengite breakdown. We note that our starting composition contains 900 ppm S and is rich in halogens and CO₂ (Table 1), as many subducted sediments (e.g. Li & Schoonmaker, 2014), which could also affect phengite as we show below for sulphur (see Prouteau & Scaillet, 2013).

Phase proportions show systematic changes with temperature, which provide guidance on melting reactions. With increasing temperature, for $T \leq 850$ °C, we observe a significant decrease in the abundance of phengite and, to a lesser extent, SiO₂ phase, whereas there is a strong increase in the amount of melt and a smaller increase in garnet mode. Garnet mode peaks at 850°C, where phengite is exhausted and SiO₂ (quartz) occurs only in low amounts. Kyanite abundance remains relatively constant in this melting interval (Table 2). These observations suggest the following incongruent melting reaction (Schmidt, 1996; Hermann & Green, 2001; Poli & Schmidt, 2002; Hermann & Spandler, 2008; Skora & Blundy, 2010; Mann & Schmidt, 2015):



Here, because of the Ca-poor composition ($X_{\text{Ca}} = 0.05$), all the clinopyroxene has been melted out.

At > 850 °C, beyond phengite-out, there is a clear change in the melting reaction, with melt fraction increasing at the expense of garnet and quartz, while kyanite mode remains constant (Table 2). This suggests that - above 850°C - garnet lies on the reactant, not on the product, side. This coincides with a significant change in melt composition (e.g. strong increase in FeO between 850 and 900°C, from 1.7 wt. % to 2.9 wt. %), consistent with Fe-rich garnet being consumed via a congruent reaction such as (e.g. Auzanneau *et al.*, 2006; Skora & Blundy, 2010):



It is worth noting that there is a remarkable difference in melt productivity between low T reaction (2) and high T reaction (3). Melt productivity has a steep trend until around 850°C, above which the trend flattens out (Fig. 11). Approximately 60 wt. % of the melt is generated at 850°C, whereas a temperature increase to 1000°C produces only 10 wt. % more melt. A comparable evolution of melt productivity has been described for the hydrous melting of a radiolarian clay, with 15 wt. % H₂O (Skora & Blundy, 2010). In contrast, the melt productivity of pelite is considerably lower, at fixed T, for less hydrated system (~ 30 % melt at 850°C with 4.4 wt. % bulk H₂O, Mann & Schmidt, 2015). Altogether, these observations confirm that the proportion of phengite ultimately controls melt productivity at high pressure and that this is considerably enhanced by the addition of water, even at relatively low temperatures (e.g. Schmidt *et al.*, 2004b).

Effect of sulphur on phase relations and melting reactions

The addition of sulphur to the experimental charges results in precipitation of sulphides (as long as fO_2 is not too oxidizing), in increasing proportions with more S input (Table 2), following the common reaction (1):



By virtue of the reaction (1), the increase in elemental S content is therefore coupled with an increase in fO_2 , the two effects cannot be disentangled in our experiments.

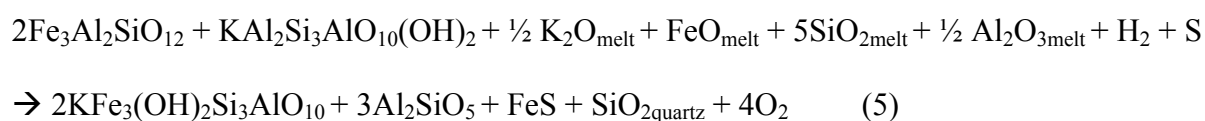
The stability of pyrrhotite in our experiments in the fO_2 range investigated, together with the absence of anhydrite, are consistent with previous experiments performed on Ca-poor sediments (Prouteau & Scaillet, 2013) and with the empirical model of sulphide-sulphate stability in subducting sediments of Canil & Fellows (2017). Because a significant part of iron is locked into sulphide, the X_{Mg} of other Fe-Mg coexisting phases increases. In particular,

liquid, garnet, and micas have systematically higher X_{Mg} compared with sulphur-undoped experiments (e.g. Fig. 5b, 6c, 7c), an observation previously made in low (e.g. Scaillet & Evans, 1999; Costa *et al.*, 2004; Parat *et al.*, 2008) or high (Prouteau & Scaillet, 2013) pressure experiments on silicic magmas, but also on single Fe-Mg silicate phases alone (e.g. Popp *et al.*, 1977). For sulphide-saturated experiments, the more sulphur is added, the more iron is held by sulphide and, as a result, the more the coexisting liquid and ferro-magnesian silicate phases are Mg-rich.

Adding S at 800°C favours the crystallization of biotite in lieu of phengite, thereby confirming that S affects the stability field of phengite (Prouteau & Scaillet, 2013), and expands the biotite stability field toward higher pressure. At 800°C, the addition of sulphur decreases garnet, phengite and melt proportions and increases biotite, kyanite and SiO₂ abundances (Figs 3, 4) suggesting therefore that S promotes a reaction of the form (e.g. Massonne & Szpurka, 1997; Hermann, 2002; Thomsen & Schmidt, 2008) :



This goes along with a decrease in melt proportion relative to the S-undoped system and a higher modal amount of biotite relative to that of phengite (Fig. 3). Therefore reaction (4) with sulphur may be tentatively written as:



with melt components on the reactant side. Only a few experiments of sediments partial melting at $P > 3$ GPa have reported biotite in their run products (Hermann & Green, 2001 and Hermann, 2002 (synthetic sediment - KCMASH); Nichols *et al.*, 1994 (natural clay); Martindale *et al.*, 2013 (natural volcanoclastic sediments)). Comparison of phase relations between Fe-free and Fe-bearing (natural) systems shows that Fe widens the stability field of garnet + phengite (Hermann, 2002). Bulk FeO content has been shown to control the overall

biotite stability and biotite to phengite reactions in sediments (Thomsen & Schmidt, 2008) and our results suggest that high S has a similar effect by scavenging Fe via sulphide crystallization.

In the 800-850°C temperature range, melting involves consumption of biotite, quartz and, to a lesser extent, kyanite, with the production of glass and garnet (1 wt. % S_{in}) or garnet + orthopyroxene (2.1 wt. % S_{in}) (Figs 3, 4). These observations suggest that biotite reacts out via an incongruent melting reaction of the form:



A somewhat similar equation, with kyanite on the reactant side, was proposed by Hermann & Green (2001) as being the high-P biotite-melting reaction in KCMASH model system. At fixed T, melt productivity via reaction (6) is lower than for the phengite-melting reaction (reaction 2), owing to the higher thermal stability of biotite compared to that of phengite (Fig. 4). As more sulphur is added to the system, more biotite is present in the residue and the melt productivity is lower.

Above 800°C, i.e. beyond the mica stability field, garnet proportion strongly decreases with increasing sulphur content at fixed T. Orthopyroxene crystallizes together with (850°C), or instead of (900 °C), garnet in the 2.1 wt. % S_{in} runs. The growth of orthopyroxene is correlated to a moderate increase in kyanite. The following reaction may qualitatively account for garnet consumption in the presence of sulphur:



where Fe₃Al₂SiO₁₂ is the almandine component in garnet and FeAl₂SiO₆ the Fe-tschermak component in orthopyroxene.

Orthopyroxene and orthopyroxene-kyanite stability fields have been bracketed in high pressure experimental melting of Fe-free model composition (KCMASH, Hermann & Green, 2001; Hermann, 2002). Orthopyroxene is not a common high-pressure phase in crustal rocks

(e.g. Hermann, 2002), but orthopyroxene coexisting with kyanite has been described to form in cracks in pyrope megablasts in white schist of the Dora Maira Massif (Simon & Chopin, 2001). The enstatite in equilibrium with kyanite contains typically about 3 wt. % but up to 8.4 wt. % Al_2O_3 , which is in the range of the experimentally grown orthopyroxenes at 850-900°C. This suggests that orthopyroxene and kyanite can be an ultrahigh-pressure assemblage in very Mg-rich rock types (see also discussion in Hermann, 2002).

Above 800°C, the melt fraction increases at the expense of garnet (1 wt. % S_{in}), orthopyroxene (2.1 wt. % S_{in}) and quartz. This suggests that melting is governed by a congruent reaction, similar to reaction (3) in sulphur-poor pelite, such as:



Melt productivity displays a trend in sulphur-rich sediments very similar to that observed in S-undoped charges, namely a steep trend upon reaction (6), in biotite stability field, and a flat trend upon reaction (8) (Fig. 11). The dissolution of anhydrous Fe-Mg phases is enhanced by high S bulk contents, inducing higher melt productivities at fixed T (Fig. 11). This is indicative of a small but detectable flushing role of sulphur at high pressures and for $T > 850^\circ\text{C}$, as already observed for basaltic lithologies (Prouteau & Scaillet, 2013). In contrast, as discussed above, the opposite is observed in the low temperature range.

It is worth noting that the influence of sulphur on phase relationships observed in our experiments (namely, decreasing garnet mode with sulphide content, high X_{Mg} in silicate ferro-magnesian phases) has also been documented during the sulphidation of low grade pelitic rocks. For instance, Guidotti (1970) notices that garnet decreases modally with increasing sulphide content in sillimanite grade pelitic rocks in the Oquossoc area (Maine), biotite being greatly enriched in Mg in sulphide-rich samples. Similarly, Tracy & Robinson (1988) show that very magnesian assemblages (e.g. more magnesian biotite and cordierite) were produced through sulphidation of granulite-grade pelitic rocks from Massachusetts; in

the presence of an H₂S-rich fluid, Fe is progressively and effectively removed from the reactive bulk composition of the rock and sequestered in sulphides. Nesbitt (1986a, b) developed equations and calibrations to document the responses of silicate-oxide-sulphide assemblages to variations in fS_2 (among other parameters) in metamorphic rocks. His results indicate that increasing fS_2 (or fO_2) induces, for example, the disappearance of garnet and the increase of X_{Mg} in ferro-magnesian phases, as reported here. Lastly, such sulphide-silicate reactions have been also documented for prograde sulphide metamorphism in blueschist and eclogite (metasediment and metabasalt) from New Caledonia (Brown *et al.*, 2014). It therefore appears that introduction of S in subsolidus or partially melting rocks drives Fe-Mg silicates towards Mg-rich compositions.

Implications for subduction zone chemical fluxes

Sulphur contents of peraluminous hydrous felsic melts at high pressure

Sulphide is the stable phase in all hydrous (8.5 wt. % total H₂O) experiments undoped or doped with elemental sulphur (Table 2). In contrast, partially melted Ca-rich oceanic basalt is saturated in sulphide and sulphate at equivalent P-T-H₂O- fO_2 conditions and S contents (Prouteau & Scaillet, 2013). These experiments used the same assembly and vessel as the present study, which rules out experimental conditions as being not appropriate (i.e. too reducing) for anhydrite crystallization per se. Instead, the lack of anhydrite reflects primarily the Ca-poor character of our starting material. In particular, our results confirm the prediction of Carroll & Rutherford (1987) that magmas with high normative diopside (i.e. high Ca content) crystallize anhydrite at lower fO_2 than those with low Ca. Canil & Fellows (2017), also documented a shift of the sulphide/sulphate (SSO) buffer to higher fO_2 (~ 1 log unit at

2.5 GPa) for low bulk X_{Ca} pelitic composition. Sulphide has not been identified in charge PEL68h, which has a higher bulk H_2O content (15 wt. % H_2O). The lack of sulphide in this charge is presumably due to higher fO_2 resulting from higher fH_2O . Charge PEL69h is doped with a solution of H_2SO_4 (1 wt. % S_{in} as S^{6+} ; 15 wt. % H_2O) and has trace amounts of sulphide, but anhydrite occurrence is only inferred.

The experiments carried out with a MgO filler (i.e. more oxidizing) show significantly higher melt sulphur contents than those performed with a BN filler (i.e. less oxidizing). For instance, with a BN filler, the melt sulphur content is about 150 ppm at 800°C and $S_{in} = 2.1$ wt.% and reaches ~830 ppm with a MgO filler at 750° C and $S_{in} = 2.1$ wt.% (Fig. 8a, Table 3). This highlights the key role of fO_2 on the sulphur content at sulphide saturation (SCSS) (e.g., Carroll & Rutherford, 1985, 1987; Jugo, 2009; Li & Audétat, 2013, 2015).

For a given filler, melt sulphur contents at sulphide saturation (SCSS) increase with temperature or total sulphur content (Table 3, Fig. 8a). As Stolper *et al.* (1987) have emphasized, the bulk effect of temperature on volatile solubility in silicate melts is controlled by the energetic balance between the reactions controlling molecular (e.g. H_2S) and anion groups' solubilities (e.g. HS^- , SO_4^{2-}). In general, the solubility of molecular species decreases with T (Stolper *et al.*, 1987; Fogel & Rutherford, 1990), whereas the abundance of species formed by reaction with the melt is enhanced by temperature (e.g. Zhang, 1999). The fact that the SCSS has a positive temperature dependence, as observed in previous studies, might be therefore interpreted as the dominant presence of anion group species over molecular species in rhyolite melts (see Clemente *et al.*, 2004). The increase in SCSS with increasing amount of sulphur added to the system suggests that the fO_2 within the capsules increases with increasing S_{in} , by virtue of the reaction (1) (see above). However, we can not exclude also the additional role of pyrrhotite composition (i.e. varying Fe/S atomic ratios with bulk sulphur content) or melt composition (e.g. alkali contents). For instance, Clemente *et al.* (2004) have

shown that, in rhyolite melts, the fS_2 (given by pyrrhotite compositions or calculated from MRK-EOS approach) is a function of the initial amount of sulphur in the charge and of the imposed experimental conditions. They have shown that fS_2 exerts a dominant control on the sulphur solubility in hydrous silicate melts, which increases with fS_2 (Clemente *et al.*, 2004). By adding sulphur to the starting material, we changed the fS_2 of the system (see also Prouteau & Scaillet, 2013). However, as we did not determine the fS_2 in our experiments, its impact on SCSS cannot be properly disentangled from the control of fO_2 .

With a total 2.2 wt. % sulphur content in the source, a hyperaluminous, hydrous ($H_2O > 20$ wt. %) felsic ($SiO_2 \sim 75$ %) sulphide-saturated melts produced at 750 °C can achieve > 800 ppm S content (Table 3, Fig. 8a). Melts produced at 900°C in H_2SO_4 doped experiment (1 wt. % S_{in} , 15 wt. % H_2O) achieves the highest S content of our study (3500 ppm). These observations are consistent with previous studies that show that oxidized conditions enhances the solubility of S (e.g. Carroll & Rutherford, 1987; Luhr, 1990; Scaillet *et al.*, 1998; Jugo *et al.*, 2005; Prouteau & Scaillet, 2013; Jégo & Dasgupta, 2014; Canil & Fellows, 2017). In the 750-800°C temperature range, corresponding to the slab top temperature of most subduction zones (Syracuse *et al.*, 2010), melts at sulphide saturation of the S-undoped experiments represent a small fraction (< 10 %) of the sulphur inventory in the source (Supplementary Data 4). The proportion of pyrrhotite increases with the bulk sulphur content at fixed T and fO_2 (Table 2) and, consequently, the fraction of S removed from the source by the silicate melt decreases with sulphur content (Supplementary Data 4). At higher temperatures (850°C and 900°C), melt can transfer a larger proportion (up to ~ 50 wt. %) of the total sulphur initially present, provided the residue contains only trace amount of sulphide, as is the case for the most oxidizing conditions for S-undoped experiments (Supplementary Data 4).

Considering that the mantle wedge is metasomatized by a few % of such sediment-sourced hydrous melts (less than ~ 5 wt. %, based on isotopic studies for most sediment-rich

arc magmas, e.g. Carpentier *et al.*, 2008), high fO_2 and/or high S content in the source (~ 4 wt. %, Prouteau & Scaillet, 2013) are implied if the S enrichment of arc magma mantle source occurs by this process alone.

LIL and light elements transfer

LIL elements. The first melt (750°C) generated at sub-arc depths from a S-undoped hydrous pelite is strongly trondhjemitic (Figs 7f, 7g), a result of the buffering role of phengite on residual melt composition. Our results indicate that phengite stability is sensitive to sulphur content, and that biotite replaces phengite in sulphur-rich systems, thus buffering melt K_2O content at higher temperatures. In this way, the K_2O/Na_2O ratios of low temperature (i.e. in the micas stability domain) anatectic melts at high pressure will depend not only on the bulk K_2O/H_2O and temperature, but also on the sulphur content. This could explain the large range of K_2O/Na_2O and S/K_2O analysed in melt inclusions in mantle xenoliths, inferred to represent infiltrating slab melts in mantle wedge (e.g. Kepezhinskas *et al.*, 1995, 1996; Schiano *et al.*, 1995; Métrich *et al.*, 1999; Vannucci *et al.*, 2007; Turner *et al.*, 2012), or in IAB melt inclusions (Wallace and Edmonds, 2011 and references herein). The K_2O/Na_2O ratio of the sediment-derived trondhjemites ranges from 0.24 to 0.31, well above that of trondhjemite produced by hydrous melting of mafic crust at sub-arc depths ($K_2O/Na_2O < 0.15$; Prouteau *et al.*, 2001; Prouteau & Scaillet, 2013). At 800°C, melts are mostly granitic (excepted for the most sulphur-rich composition) but the K_2O/Na_2O remains lower than that of the starting composition. Protracted infiltration of such low temperature melts into the overlying mantle will thus impart a more potassic character to the metasomatized mantle, compared to basalt-derived slab melts, and ultimately to arc magmas. Beyond the mica stability field, above 800°C, and regardless the sulphur content, anatectic melts are strongly

potassic (with $K_2O/Na_2O > 2$) and peraluminous, unlike usual melt inclusions or pockets found in supra-subduction mantle xenoliths (e.g. Kepezhinskas *et al.*, 1995, 1996; Schiano *et al.*, 1995; Métrich *et al.*, 1999; Vannucci *et al.*, 2007; Turner *et al.*, 2012). Partial melting of peridotite fluxed by such potassic melts could however contribute to the generation of potassic and ultrapotassic magmas in modern convergent margins (e.g. de Hoog & van Bergen, 2000; Mallik *et al.*, 2015).

The experimental hydrous melts show a systematic enrichment of Sr with respect to the starting material, suggesting that there is no residual phase capable of effectively retaining Sr. Recycling efficiencies, or mobilities, can be calculated from phase proportions and compositions in Tables 2 and 4 respectively (where mobility = $C_i^{melt} * \% \text{ melt} / C_i^{\text{starting composition}}$). Mobilities for Sr are systematically $> \sim 45 \%$, and increase with temperature. Therefore, these metasomatizing melts will selectively transport Sr to the mantle wedge and ultimately to arc magmas.

Our experimental partition coefficients confirm that residual phengite and biotite control the Ba (with $D_{Ba}^{Ph/melt} > D_{Ba}^{Bt/melt}$) and Rb (with $D_{Rb}^{Bt/melt} > D_{Rb}^{Ph/melt}$) contents of the equilibrium melts as well as their Rb/Ba ratios. At 750°C, regardless of the bulk sulphur content, only 20-26 % of the initial inventory of Rb and 11-22 % of Ba are recycled by hydrous sediment melting, due to the large proportion of micas in the solid residue (Tables 2 and 4). As mica is progressively exhausted from the residue with increasing temperature, Rb and Ba concentrations in melt increase steadily and recycling is more efficient ($> 55 \%$ at 800°C for both elements), with Rb/Ba ratios controlled by the relative proportions of phengite and/or biotite in the residue, i.e. by the total sulphur content. At fixed temperature, adding sulphur to the system promotes biotite crystallization at the expense of phengite and therefore decreases melt Rb/Ba ratio. Therefore, variable sulphur content of subducted pelite can contribute to the variability of Rb/Ba ratios identified in mafic arc magmas.

Our partial melts exhibit uniformly low Ba/Th ratios ($30 < \text{Ba/Th} < 35$, Table 4) as expected for the “sedimentary component” in IAB. At low temperature, the effects of monazite (principal host for Th) and micas (principal hosts for Ba) counterbalance each other, while at high temperature no phase controls these elements anymore, hence the partial melts inherit their Ba/Th from the starting material (Fig. 12a). Our data can, however, hardly explain the elevated Ba/Th ratios (~ 100) observed for “sediment-flavored” arc magmas (e.g. South or Central Lesser Antilles (Fig. 13a), Aleutian, Ryuku), without the selective addition of Ba. Local enrichment in Ba in the pelitic sediment should be considered. Indeed, sedimentary Ba concentrations can vary largely because barite (BaSO_4) controls most of the Ba budget of marine sediments (Plank & Langmuir, 1998) and even minor quantities of barite in a sediment will have a large effect on the bulk Ba concentration. A barite-rich lithology will probably produce silicate liquids with a higher Ba/Th ratio (and probably a lower La/Sm_{PM} ratio due to the sulphur effect, see Fig. 13a and next section) but this hypothesis clearly requires further work. We can also envision that aqueous fluids flushing the sedimentary layer are selectively enriched in soluble elements. The main source of water at sub-arc depths comes from serpentinite dehydration (e.g. Syracuse *et al.*, 2010), and fluids produced by this process may carry some of the slab-derived trace elements. However, Ba can show little or no increase in serpentines or their associated pore fluids (Ryan & Chauvel, 2014 and references therein). Moreover, high pressure experiments (e.g. Spandler *et al.*, 2014) show that fluids produced by serpentinite dehydration at sub-arc depths display limited Ba concentrations (~ 10 ppm) and Ba/Th fractionation (~ 25). The high Ba/Th observed in Lesser Antilles (and other sediment-rich subduction zones) is thus best explained by the contribution of Ca-rich sediment-derived melts (Skora *et al.*, 2015, 2017; Carpentier *et al.*, 2009).

Sediment-poor arcs typically exhibit low LREE and Th contents and extreme Ba/Th ratios, in excess of 1000 (Elliott, 2003; Fig. 13a). The corresponding slab component cannot

be extracted from subducted Ca-poor pelite (this work). Ca-rich or CaCO₃-rich sediment-derived melts (Skora *et al.*, 2015, 2017) display higher Ba/Th ratios, but, as for Ca-poor sediments, their quite high LREE or Th contents can hardly explain the overall natural trend in Fig. 13a. To date, these characteristics are best explained by a fluid phase of various salinities expelled from the subducted basaltic crust by devolatilization (Green & Adam, 2003; Kessel *et al.*, 2005b) or hydrous melting (Carter *et al.*, 2015). Our results reinforce therefore the difficulties of explaining arc geochemistry with a single metasomatic agent.

Finally, the post-Archean upper continental crust is enriched in alkali elements (K, Rb), compared to the Archean upper crust (e.g. Condie, 1989). Subduction of sediments derived from newly formed cratons in the late Archean and the secular increase of sediment cycling during the Phanerozoic may have contributed to the LILE inventory that ends up in the mantle wedge.

Light elements. Boron shows an incompatible behaviour in all our experiments and its calculated mobility is $> \sim 70\%$ whatever the temperature or the sulphur content. The behaviour of B is partly controlled by phengite ($D_B \sim 0.2$; Table 6), while it is more incompatible in biotite ($D_B \sim 0.05$; Table 6). Therefore, in the mica stability field, B recycling efficiency through Ca-poor sediment-derived melts will be enhanced by high sulphur contents.

In our experiments, the Li concentration of melt (70 to 130 ppm) decreases steadily with temperature, indicative of behaviour as an incompatible element with no major residual host phase (Fig. 9). At 750°C, Li mobility increases from $\sim 36\%$ in the S-undoped charge to $\sim 59\%$, in the 2.1 wt. % S_{in} charge. This trend is explained by the decrease in modal garnet ($D_{Li}^{Grt/melt}$ up to 0.84, Table 5) as the sulphur content increases. For $T > 800^\circ\text{C}$, calculated mobility is $> 80\%$ whatever the temperature or the sulphur content. Our data show that Li is

efficiently removed from subducted sediments via hydrous partial melting, with an enhanced efficiency at high sulphur content and high degree of partial melting.

Be concentration was below the detection limit for many glasses and silicates in our experiments, which makes interpretation of our results speculative. In the temperature range 800-1000°C, Be concentration in the silicate melt decreases steadily with temperature (Table 4), indicative of an incompatible behaviour with no major residual host phase. At 800 °C (S-undoped run, 4 % phengite in the residue), Be concentration in partial melts is of the order of 5 ppm, representing almost all the initial inventory (~ 2.3 ppm). Be is below the detection limit in micas in the 800 °C charges, but, nevertheless, our data suggest that phengite exerts little control on Be behaviour in the studied melting range, as already observed by Johnson & Plank (1999). Although more work is needed, our results confirm that Be is efficiently recycled by hydrous sediment melting and that phengite complete exhaustion is not necessary to enable an effective transfer of this element (Johnson & Plank, 1999).

REE and actinides behaviour

The concentration of REE and actinides in our experimental melts are mainly controlled by garnet (predominately HREE) and monazite (LREE and actinides).

Monazite buffers the LREE contents of melt and preferentially holds back Th and U, hosting up to 95 % of LREE and Th under subsolidus conditions in Ca-poor sediments (Hermann, 2002). Monazite affects key elemental ratios (La/Yb, La/Sm, Th/La or U/Th) of sediment melts (e.g. Hermann & Rubatto, 2009; Skora & Blundy, 2010, 2012; Stepanov *et al.*, 2012; Maimaiti *et al.*, 2019). In our S-undoped Ca-poor sediment, monazite was identified in all charges up to 800°C, at which melting degree is > 50 %. Following the method proposed by Skora & Blundy (2010), we estimate that monazite disappears between 830°C and 850°C,

whatever the sulphur content. Because Sm was below the detection limit in the glasses produced at 750°C (for S-undoped run), we use Nd concentration and Sm detection limit to estimate the Sm concentration in this glass. We calculate a total LREE (Pr excluded) content of ~70 ppm in the glass of the S-undoped 750°C charge. In the 2.1 wt. % S_{in} 750°C run, the measured Σ LREE (Pr excluded) rises to 140 ppm (Table 4). The concentration of LREE in the melts coexisting with monazite at 800°C for the S-undoped experiment is 208 ppm (Pr excluded) and rises slightly to 217 ppm in the 2.1 wt. % S_{in} experiment (Table 4). These results thus suggest that the LREE content in melt coexisting with monazite increases with bulk sulphur, perhaps due to complex change in major element compositions of hydrous melts as S increases (for example, an increase in CaO melt content as S increases could affect monazite solubility, e.g. Maimaiti *et al.*, 2019). The significant anhydrite-celestine substitution in monazite in the sulphur-doped charges is consistent with this trend, and could have, moreover, a significant impact on the monazite/melt partition coefficients (e.g. D_{Th}/D_{La}).

Effect on REE signature. The complex combined effects of monazite and garnet produces a wide range of La/Yb ratios (Fig. 9a, Table 4): the highest ratios are observed in sulphur-poor runs (with a high proportion of garnet, which retains HREE) and beyond the monazite (which retains LREE) stability field, while monazite-saturated melts of the sulphur-rich experiments show the lowest ratios (Table 4). The addition of sulphur therefore lowers LREE/HREE ratios of hydrous melts at fixed temperature. For instance, at 800°C, the LREE/HREE in the silicate melt decreases from ~74 in sulphur-undoped run to ~12 in the 2.1 wt. % S_{in} experiment. In the same way, La/Sm is mainly controlled by monazite (La) and garnet (Sm). Monazite-saturated melts of the sulphur-rich experiments present the lowest La/Sm, below the La/Sm ratio in the starting sediment, (Fig. 12b, Table 4). This is mainly

because the Sm partition coefficient for low temperature (< 850 °C) grossular-rich garnet can be as high as 6 (Table 6), but we cannot exclude additional effects arising from either the proportion or composition of the monazite (see below). At 850 °C (monazite out), the same effect of sulphur is observed and attributable in that case to garnet only. At 900 and 1000 °C, La is not significantly fractionated from Sm, because low $X_{\text{grossular}}$ garnet does not incorporate Sm (Table 5). Therefore Ca-poor sediment partial melts display a large range of $(\text{La}/\text{Sm})_{\text{PM}}$ explained by the combined effect of temperature and sulphur content (Fig. 13a). This should be taken into consideration when modeling the sediment contribution to arc magmas.

Effect on Th/La. The similarity of Th/La in subducting sediments and in the subduction component of arc magmas has led to the proposition that Th and La behave similarly during sediment recycling to the arc (Plank, 2005). For example, a maximum fractionation of 30 % is observed for Lesser Antilles subduction zone (Plank, 2005). Monazite, which preferentially incorporates LREE and Th, exerts a strong control on the melt Th/LREE ratio (e.g. Hermann & Rubatto, 2009; Skora & Blundy, 2010, 2012; Stepanov *et al.*, 2012). However, in previous trace elements-doped experiments, the partition coefficients for Th are either lower (e.g. Skora & Blundy, 2010) or higher (e.g. Skora & Blundy, 2010; Stepanov *et al.*, 2012) than those for LREE. In our S-undoped experiment, at 750°C, monazite-saturated melts shows their Th/La ratios increased by 60 % compared to the source (Fig. 12c, Table 4). As monazite is the sole phase likely to fractionate drastically Th from La, this pattern suggests that, in our trace elements undoped experiments, $D_{\text{Th}}^{\text{monazite/melt}}/D_{\text{La}}^{\text{monazite/melt}}$ is below unity. Interestingly, this trend is in agreement with the partition coefficients of natural monazite-peraluminous rhyolite glass pair from Macusani, Peru ($D_{\text{Th}}/D_{\text{La}}=0.5$) (Pichavant, 1987; Montel, 1993). With 1 or 2.1 wt. % S_{in} , this Th/La fractionation drops to 14 % (Fig. 12c, Table 4). This could be related to the higher monazite

solubility proposed for the sulphur-rich compositions. Another possible explanation, not exclusive, is that $D_{Th}^{monazite/melt}/D_{La}^{monazite/melt}$ decreases significantly for S-enriched monazite, owing to the anhydrite-celestine substitution, though our semi-quantitative analyses (800°C) suggests the opposite (Table 4, Supplementary Data 3). This last point clearly requires additional work.

In hydrous melts saturated with trace amounts of monazite, at $T = 800^\circ\text{C}$, the source-normalized Th/La is ≈ 1 , regardless of sulphur content (Fig. 12c). The same trend is observed once monazite is exhausted from the residue ($T > 850^\circ\text{C}$). Therefore, our results suggest that minor residual monazite in the subducted sediments will not significantly affect the Th/La of the coexisting melt. There is no need for monazite to be completely consumed in order to transfer the Th/La ratio of sediments into arc magmas, as previously suggested by Stepanov *et al.* (2012). We speculate also that S-rich conditions will favor a low fractionation of LREE relative to Th, for the lowest temperatures.

The sediment signal in arc magmas is moreover characterized by a selective enrichment in LREE and Th abundances. At 750°C , the transport capacity of LREE and Th is relatively low in sulphur-poor (S-undoped) compositions (mobilities of 8 % and 13 % for La and Th, respectively), but rises to more than 20 % for both elements in the 2.1 wt. % S_{in} charges. At 800°C and above, mobilities are uniformly high ($> 50\%$). Therefore, partial melts of subducted Ca-poor sediments with residual monazite for sulphur-rich conditions ($S_{in} = 2.1$ wt.%) at 750°C , or at 800°C and above whatever S content, are in agreement with the observed Th and La abundances and Th/La systematics in sediment-rich arc magmas.

Effect on U/Th. The fractionation of U from Th in Ca-poor sediments is mainly controlled by monazite and, to a lesser extent, garnet and zircon. The 750°C monazite-saturated hydrous melts show a source-normalized U/Th well above unity (Fig. 12d). This is

because $D_{Th}^{monazite/melt}$ is approximately 20 times greater than $D_U^{monazite/melt}$ (Skora & Blundy, 2010; Stepanov *et al.*, 2012). Sulphur impact on U/Th fractionation is moreover noticeable at this temperature: the U/Th ratio increases by > 30 % compared to the starting sediment in the S-undoped charge and this increase is > 50 % in the 2.1 wt. % S_{in} charge (Fig. 12d, Table 4). As $D_U^{Grt/melt} > D_{Th}^{Grt/melt}$ (Table 5), then this effect could probably be partly related to the decrease of residual garnet with increasing sulphur content. However, the impact of sulphur at fixed T is negligible (< 2 wt. %) at 800°C, with trace amounts of monazite, or once monazite is exhausted (T > 850°C) (Fig. 12d, Table 4). We therefore postulate that the proportion and/or composition (with D_{Th}/D_U in S-rich monazite > D_{Th}/D_U in S-poor monazite) of residual S-rich monazite mainly control the trend observed at 750°C. At 800°C, where monazite occurs in trace amounts, or beyond the monazite stability field, Th and U are not significantly fractionated, whatever the sulphur content. The slight uranium excess observed at T > 850°C (Fig. 12d) may be due to the presence of carbonates ($D_U^{carbonate/melt} < D_{Th}^{carbonate/melt}$), identified in trace amounts at high temperature, which probably counteracts the effect of garnet and zircon ($D_U^{zircon/melt} > D_{Th}^{zircon/melt}$ in the explored fO_2 range, Burnham & Berry, 2012).

Our results show that U excess is achieved in Ca-poor sediments partial melts, with larger excess observed at low temperature and sulphur-rich conditions. At low temperatures, this signature is controlled by the proportion and composition of the accessory phases, which depends in turn on the composition of the sediment. For instance, apatite-saturated partial melts expelled from volcanoclastic sediments will have slight Th excess (Martindale *et al.*, 2013), a signature never produced in our composition. Thus, as already noticed by previous authors (e.g. Hermann & Rubatto, 2009), care has to be taken when the nature of the slab fluid phase is determined from such an isotopic signal alone. U-Th systematics of arc lavas best

reflect the contrasting solubilities of accessory phases in subduction zones with different thermal and compositional controls.

Altogether, our results show that melts expelled from Ca-poor sediments variously enriched in sulphur can explain the overall U/Th vs Th trend for most sediment-rich lavas (Fig. 13b) but can hardly account for the extreme U enrichment (associated with low Th concentrations) characteristic of some sediment-poor arcs (Fig. 13b). These arcs require another source than Ca-poor sediments for U efflux from subducted materials, as already discussed above for Ba enrichment.

Recycling of Ca-poor sediment in subduction zones and the HFSE cycle

Nb and Ta signature of pelite melts. As rutile is a major host of HFSE such as Ti, Nb, and Ta, the solubility of rutile is the key to the HFSE concentrations of hydrous silicic melts from the subducting sediment. Moreover, rutile preferentially incorporates Ta over Nb during hydrous melting, with $D_{\text{Nb}}/D_{\text{Ta}} < 1$ (Schmidt *et al.*, 2004a; Klemme *et al.*, 2005; Xiong *et al.*, 2011). Xiong *et al.* (2011) have shown that, in the range 1.5-3.5 GPa and 900-1350°C, temperature and melt water content have marked effects on partition coefficients for felsic melts (D_{Nb} , D_{Ta} and $D_{\text{Nb}}/D_{\text{Ta}}$ increase with decreasing temperature and water content), whereas pressure and melt composition do not.

The hydrous felsic melts produced in our experiments are all saturated in rutile. Whatever the temperature or sulphur content, Ti, Nb and Ta show negative anomalies relative to LILE and are depleted with respect to the starting material (Fig. 9a). $(\text{Th}/\text{Nb})_{\text{N}}$ is also systematically above 1 in our experiments (Fig. 12e). Therefore, our experiments fulfill the constraint that the slab component in the source of the enriched arc lavas exhibits higher Th/Nb than the subducting sediment (Elliott, 2003). In detail, $(\text{Th}/\text{Nb})_{\text{N}}$ increases from 750°C

to 800°C (except for the more S-rich run with $S_{in} = 2.1$ wt. %) owing to increasing monazite dissolution. At 800°C the fractionation is clearly more pronounced in the S-undoped charge, owing to the presence of phengite which incorporates Nb (Fig. 10c); the $(Th/Nb)_N$ ratio then decreases at 850°C because of the Nb contribution from phengite breakdown (in addition to increasing rutile contribution). Beyond the stability field of monazite, $(Th/Nb)_N$ decreases steadily with temperature, whatever the sulphur content: more and more rutile is dissolved into the hydrous melt during the hydrous partial melting of subducting metapelite at subarc depths, more HFSE are delivered to the mantle sources of arc magmas.

All analysed melts show sub-chondritic Nb/Ta ratios (Table 4) and fractionation of Nb/Ta relative to their sediment precursor, but the fractionation direction and magnitude depend, primarily, on temperature (Fig. 12f) and sulphur content. Whatever the sulphur content, $(Nb/Ta)_N$ increases drastically from 750°C to 900°C (Fig. 12f). The elevated Nb/Ta at 900°C is best explained by the preferential incorporation of Ta over Nb in residual rutile (Schmidt *et al.*, 2004a; Klimm *et al.*, 2008; Hermann & Rubatto, 2009). To test this hypothesis, we used the empirical expression derived by Xiong *et al.* (2011) to estimate $D_{Nb}^{rutile/melt} / D_{Ta}^{rutile/melt}$ in our experiments. Calculated $D_{Nb}^{rutile/melt} / D_{Ta}^{rutile/melt}$ vary from 0.6 to 1.0, depending on temperature and melt water content. Therefore, hydrous melting at high temperature, in the presence of residual rutile and without any other phase capable of fractionating significantly Nb and Ta, should result in melts with constant or higher Nb/Ta when compared to the starting sediment, i.e. a trend at variance with the sub-chondritic Nb/Ta ratio of arc magmas. In contrast, low temperature (750°C) melts in equilibrium with phengite (S-undoped) or phengite + biotite (1 wt. % S_{in}) exhibit lower Nb/Ta ratios than the starting sediment. At 800°C and 2.1 wt. % S_{in} , with only biotite in the residue, $(Nb/Ta)_N$ is close to 1, suggesting that biotite alone can hardly counteracts the rutile effect. In agreement with previous studies (Nash & Crecraft, 1985; Acosta-Vigil *et al.*, 2010; Stepanov & Hermann,

2013), our results suggest that low temperature residual phengite in equilibrium with felsic melt preferentially incorporates Nb over Ta. Our results thus extend Stepanov & Hermann's (2013) findings to lower temperatures, suggesting that even Ti-poor phengites (0.5-1.2 wt. % TiO₂, Supplementary Data 3) may significantly fractionate Nb and Ta. Therefore, in the phengite stability field, the rutile effect can be counterbalanced and melting reduces Nb/Ta relative to the sediment precursor.

The above inferences suggest that high pressure hydrous melting of terrigenous sediments in Phanerozoic subduction zones might be an important process to produce Nb-poor melt with sub-chondritic Nb/Ta. Phanerozoic arc magmas and continental crust may inherit their sub-chondritic Nb/Ta ratios from a source metasomatized, inter alia, by these hydrous felsic melts, derived from the top sedimentary layer of the downgoing slab. This process also produces Nb-rich restites with super-chondritic Nb/Ta, that could represent one of the missing reservoirs to balance the sub-chondritic Nb/Ta of the upper crust and the depleted mantle, as already suggested by Stepanov & Hermann (2013).

Whether Nb/Ta fractionation of crustal rocks is a modern process or was already operating during Archean times is unclear. Archean tonalites-trondhjemites-granites (TTGs) represent the oldest felsic continental crust. These felsic, sodic magmas are widely accepted to be the products of partial melting of hydrous metabasalt at pressures sufficiently high to stabilize garnet (e.g. Moyen, 2011). There remains however considerable controversy surrounding the geodynamic setting, some considering that TTGs formed mainly by partial melting of subducting oceanic lithosphere (e.g. Martin, 1986; Drummond *et al.*, 1996) and other favoring TTGs formation at the base of thick, plateau-like basaltic crust (e.g. Smithies *et al.*, 2003; Johnson *et al.*, 2017, 2019). Recent analyses of Nb/Ta in Eoarchean and Mesoarchean TTG associations have shown that these display highly variable Nb/Ta ratios of 7-27 (Hoffmann *et al.*, 2011). Even larger fractionations were observed in Archean migmatitic

TTGs, with Nb/Ta ratios ranging from 14 to 42 with a strongly super-chondritic average Nb/Ta of 29 (Xiong *et al.*, 2011; Stepanov & Hermann, 2013; Li *et al.*, 2017). These scattered and super-chondritic ratios are best explained by hydrous melting of rutile-bearing eclogites, if the average Nb/Ta ratio of the Archean mantle and MORB (Jochum *et al.*, 2001) are accepted. In particular, the very high Nb/Ta ratios of some TTG rocks relative to the average Archean MORB can only be explained by low degree partial melting in the presence of both rutile and a hydrous fluid (Foley *et al.*, 2002; Xiong *et al.*, 2011). Therefore, as insightfully suggested by Green (1995), Archean gneisses may be a complementary component to that part of continental crust which has a relatively low Nb/Ta.

Sedimentary cycling during the Archean is widely discussed. Isotopic studies (mass-independent S isotopic fractionation, Ce-Nd isotopes) suggest recycling of surface materials in a reduced atmosphere before the Great Oxygenation Event, which happened at about 2.4 Ga ago (Cabral *et al.*, 2013; Delavault *et al.*, 2016; Israel *et al.*, 2020). Several authors have proposed (on the basis of isotope data for Hf, O, Si) that Archean juvenile continental crust formed by melting of enriched mafic crust extracted from a still primitive mantle, and that sediment recycling occurred only since the Mesoarchean (e.g. Næraa *et al.*, 2012; Reimink *et al.*, 2016; Roberts & Santosh, 2018; Trail *et al.*, 2018; Smit *et al.*, 2019). Moreover, Rey & Coltice (2008) have proposed that during the Archean, the continental crust, covered by continental flood basalt, and with low surface elevation and low erosion level, has been isolated from other geochemical reservoirs. Their numerical experiments suggest that the relative isolation of the felsic continental crust may have ended during the Neoproterozoic, when the strengthening of the continental lithosphere allowed for the development of significant topography. The subsequent erosion and exhumation of felsic crust would have led to coupling of the continental reservoir with the mantle reservoirs. These observations suggest that deep cycling of surface-altered rocks was restricted to post-Neoproterozoic times when

recycling of such material, possibly by subduction, became prevalent (Valley *et al.*, 2005; Rey & Coltice, 2008).

The above considerations lead us to conclude that the Nb/Ta deficit (together with LILE enrichment) is a post-Archean feature, reflecting the secular increase in terrigenous, K-rich sediments recycling in the subduction factory.

The role of zircon: Zr and Hf signature of pelite-melts. In our experiments, Zr is hosted mainly in zircon, and, to a lesser extent, in garnet (Fig. 10a, Table 5; Rubatto, 2002; Rubatto & Hermann, 2007). Our study shows that zircon persists up to 1000°C and to high degree of partial melting (> 70 %) in the studied starting material. Residual garnet decreases drastically with sulphur addition, at fixed temperature. Zr and Hf concentrations increase steadily with temperature in our experimental melts, a trend consistent with increasing solubility of zircon at higher temperature. The negative Zr anomaly of the starting product is preserved (1000°C) or amplified ($T < 900^\circ\text{C}$) in the entire melting interval (Fig. 12g). At 800°C, Hf concentration in the partial melt is around 2-3 ppm representing 24 % (sulphur-undoped) to 28 % (2.1 wt. % S_{in}) of the initial inventory. These mobilities are of the same order of magnitude as the estimates for the Izu-Mariana arc (Chauvel *et al.*, 2009), and support the hypothesis that the Hf isotopic signature of arc lavas might be related to the addition of sediment melts.

Zircon (Linnen & Keppler, 2002; Rubatto & Hermann, 2007) and garnet ($D_{\text{Zr}}^{\text{Grt/melt}}/D_{\text{Hf}}^{\text{Grt/melt}} \sim 1.3-1.9$; Table 5) are able to fractionate the geochemical twins Zr and Hf. At fixed S_{in} , Zr/Hf ratio increases with increasing temperature, providing new evidence that the melt Zr and Hf are controlled by small amounts of zircon (Fig. 12h). For $T < 900^\circ\text{C}$, the chondritic Zr/Hf ratio of the starting material is preserved or amplified by partial melting, except for the more sulphur-rich run (Fig. 12h). Although data overlap when their

uncertainties are considered (especially at 800 and 900°C), the mean Zr/Hf ratio tends to increase with the sulphur content at fixed temperature (e.g. compare 0 and 2.1 wt. % S_{in} runs at 850°C, Fig. 12h). It can be inferred that Zr-Hf fractionation is probably partly garnet-induced and thus affected by S. The effect of sulphur is much more significant on HREE/Hf ratios, due to high $D_{HREE}^{Grt/melt}$ (Table 5). For example, at 900°C, the Yb/Hf ratio is multiplied by ~10 when 2.1 wt. % sulphur is added (Table 4). Therefore the Lu/Hf, Zr/Hf and Hf isotope systematics usually used to track sediment contribution to the arc magmatism (e.g. Nebel *et al.*, 2011) is sensitive not only to slab surface temperature, but also, albeit to a lesser extent, to the sulphur content of the subducted sediments.

Pb transfer to the mantle wedge

We exclude experiments performed at $T \geq 850^\circ\text{C}$ from this discussion because of Pb contamination suspected at high temperature. Pb is incompatible in the 750-800°C experiments, whatever the sulphur content (Table 4). Pb is more incompatible than Ce, and the ratio $(\text{Ce}/\text{Pb})_N$ is systematically < 1 (Fig. 12i). The fractionation is maximum in charges saturated with high modal monazite (750 °C), which selectively incorporates LREE. Sulphur content has no significant effect on the partitioning of Pb, implying counter-intuitively that sulphide minerals are not an important carrier of Pb. At 800°C (2.1 wt. % S_{in}), pyrrhotite (4.8 wt. % in the run products, Table 2; $D_{Pb}^{\text{pyrrhotite}/\text{melt}} \sim 0.4$, Table 8) sequesters only around 4 % of the initial inventory of Pb (= 22.4 ppm, Table 4). Therefore, our data show that low temperature Ca-poor sediment-derived melt can contribute to the Ce/Pb ratio typical of arc magmas, even for sulphur-rich bulk compositions.

As already stressed, abundant evidence support that the Ce/Pb evolution in the mantle is controlled by subduction processes. Quantitative models for the Ce/Pb evolution of the mantle

and crust generally assume Pb loss from the subducted slab mainly through low Ce/Pb hydrous fluids (e.g. Kelley *et al.*, 2005). Although this point needs clearly further work and is beyond the scope of this study, the secular increase in terrigenous sediments recycling since the Mesoarchean may have contributed to the pervasive depletion of lead in the oceanic mantle. Similarly, our results show that, at low temperature, Pb is extracted 1.5 to 3.5 times more than U by hydrous melt from Ca-poor sediment (i.e. $[\text{Pb}/\text{U}_{\text{melt}}]/[\text{Pb}/\text{U}_{\text{sediment}}] \sim 1.5$ at 800°C and ~ 2 to 3.5 at 750 °C, Table 4). Preferential Pb loss from sediment (together from AOC, the key flux in accounting for U cycle, e.g. Kelley *et al.*, 2005) will increase μ (with $\mu = \text{U}/\text{Pb}$) in the slab residue and therefore potentially contribute to the HIMU mantle component identified in OIB (Ocean Island Basalt) source. Elemental and isotope systematics of U in OIB indicate formation of this mantle reservoir between 2.5 and 1.8 Ga (Andersen *et al.*, 2015).

CONCLUDING REMARKS

We have investigated phase equilibrium and trace element partitioning for hydrous Ca-poor sediments at sub-arc conditions (750-1000°C, 3 GPa). We explored the effect of bulk sulphur content (from 900 ppm to 2.2 wt. %) at various $f\text{O}_2$ on high pressure phase stabilities and compositions. The addition of elemental sulphur decreases effective bulk Fe and this has an impact on both phase compositions (e.g. high X_{Mg} of ferro-magnesian major silicate phases) and stabilities (e.g. breakdown of garnet to orthopyroxene, breakdown of phengite to biotite). The composition and solubility of a key accessory phase such as monazite could be also affected by the bulk S-content (S-component substitution in monazite).

Our results confirm previous suggestions that sediment-derived hydrous melts can exhibit high sulphur contents, and then contribute to the S-rich character of Phanerozoic arc magmas, provided that high fO_2 and/or high S content in the source prevail.

The enrichment or depletion of trace elements in the experimental sediment melts exhibit features similar to the sediment-derived slab component of arc lavas (e.g. La/Sm, Th/La, Th/Nb, Nb/Ta, Ce/Pb ratios). In agreement with previous studies, our work emphasizes the importance of residual mineralogy in controlling the trace element characteristics of sediment-derived melts. The sediment signature, including Th and Be effective transport, is enhanced in the phengite stability field at 750 °C (provided high S content) or 800 °C. This temperature range corresponds roughly to slab-top estimates from recent subduction models.

On the other hand, our study shows that Ca-poor sediment-derived melts cannot explain the large U or Ba enrichments typical of “sediment-starved” arcs. These arcs require another source (fluids expelled from serpentinite, AOC) for U and Ba, which supports the tripartite model of arc source.

Finally, the secular increase in terrigenous sediment recycling since the Mesoproterozoic could have contributed to the evolution of the composition of continental crust with time (e.g. enrichment in LILE, decreasing Nb/Ta). The long-term recycling of sedimentary material will also contribute to the chemical heterogeneity in the terrestrial mantle (e.g. Ce/Pb, U/Pb).

ACKNOWLEDGMENTS

We thank Ida Di Carlo and Patricia Benoist for assistance with EMPA and SEM, Jean-Luc Devidal and Bernard Gratuze for assistance with LA-ICP-MS and Yann Morizet and Aneta

Slodczyk for assistance with Raman spectroscopy. We thank Laura Airaghi for the Perple_X calculations.

The paper greatly benefited from constructive reviews by Yuan Li, Andrew Tomkins and Jesse Walters, and the careful editorial handling of Andreas Audétat and Georg Zellmer.

FUNDING

This work was supported by LabEx VOLTAIRE (LABX-100-01) and EquipEx PLANEX (ANR-11-EQPX-0036) projects and by grants from INSU - TellusS - SYSTER.

REFERENCES

- Acosta-Vigil, A., Buick, I., Hermann, J., Cesare, B., Rubatto, D., London, D. & Morgan, G. B. (2010). Mechanisms of Crustal Anatexis: a Geochemical Study of Partially Melted Metapelitic Enclaves and Host Dacite, SE Spain. *Journal of Petrology*. Oxford Academic **51**, 785–821.
- Albarède, F. (1995). *Introduction to Geochemical Modeling*. Cambridge University Press.
- Alt, J. C. & Burdett, J. W. (1992). Sulfur in Pacific deep-sea sediments (Leg 129) and implications for cycling of sediment in subduction zones. In : *Proc. ODP, Sci. Results. College Station, TX (Ocean Drilling Program)* **129**, 283–294.
- Andersen, M. B., Elliott, T., Freymuth, H., Sims, K. W. W., Niu, Y. & Kelley, K. A. (2015). The terrestrial uranium isotope cycle. *Nature*. Nature Publishing Group **517**, 356–359.
- Auzanneau, E., Vielzeuf, D. & Schmidt, M. W. (2006). Experimental evidence of decompression melting during exhumation of subducted continental crust. *Contributions to Mineralogy and Petrology* **152**, 125–148.
- Ayers, J. C., Watson, E. B., Tarney, J., Pickering, K. T., Knipe, R. J. & Dewey, J. F. (1991). Solubility of apatite, monazite, zircon, and rutile in supercritical aqueous fluids with implications for subduction zone geochemistry. *Philosophical Transactions of the Royal Society of London. Series A: Physical and Engineering Sciences*. Royal Society **335**, 365–375.

- Ballèvre, M., Pinardon, J.-L., Kienast, J.-R. & Vuichard, J.-P. (1989). Reversal of Fe-Mg Partitioning Between Garnet and Staurolite in Eclogite-facies Metapelites from the Champtoceaux Nappe (Brittany, France). *Journal of Petrology* **30**, 1321–1349.
- Barth, M. G., McDonough, W. F. & Rudnick, R. L. (2000). Tracking the budget of Nb and Ta in the continental crust. *Chemical Geology* **165**, 197–213.
- Bénard, A., Klimm, K., Woodland, A.B., Arculus, R.J., Wilke, M., Botcharnikov, R.E., Shimizu, N., Nebel, O., Rivard, C. & Ionov, D.A. (2018). Oxidising agents in sub-arc mantle melts link slab devolatilisation and arc magmas. *Nature Communications* **9**, 1–10.
- Binder, B. & Keppler, H. (2011). The oxidation state of sulfur in magmatic fluids. *Earth and Planetary Science Letters* **301**, 190–198.
- Borisova, A. Y., Toutain, J.-P., Dubessy, J., Pallister, J., Zwick, A. & Salvi, S. (2014). H₂O–CO₂–S fluid triggering the 1991 Mount Pinatubo climactic eruption (Philippines). *Bulletin of Volcanology* **76**, 800.
- Bouvier, A.-S., Métrich, N. & Delouie, E. (2008). Slab-Derived Fluids in the Magma Sources of St. Vincent (Lesser Antilles Arc): Volatile and Light Element Imprints. *Journal of Petrology*. Oxford Academic **49**, 1427–1448.
- Brenan, J. M., Shaw, H. F. & Ryerson, F. J. (1995). Experimental evidence for the origin of lead enrichment in convergent-margin magmas. *Nature* **378**, 54–56.
- Brown, J. L., Christy, A. G., Ellis, D. J. & Arculus, R. J. (2014). Prograde Sulfide Metamorphism in Blueschist and Eclogite, New Caledonia. *Journal of Petrology*. Oxford Academic **55**, 643–670.
- Burnham, A. D. & Berry, A. J. (2012). An experimental study of trace element partitioning between zircon and melt as a function of oxygen fugacity. *Geochimica et Cosmochimica Acta* **95**, 196–212.
- Cabral, R. A., Jackson, M. G., Rose-Koga, E. F., Koga, K. T., Whitehouse, M. J., Antonelli, M. A., Farquhar, J., Day, J. M. D. & Hauri, E. H. (2013). Anomalous sulphur isotopes in plume lavas reveal deep mantle storage of Archaean crust. *Nature*. Nature Publishing Group **496**, 490–493.
- Canfield, D. E. (2004). The evolution of the Earth surface sulfur reservoir. *American Journal of Science*. American Journal of Science **304**, 839–861.
- Canil, D. & Fellows, S. A. (2017). Sulphide–sulphate stability and melting in subducted sediment and its role in arc mantle redox and chalcophile cycling in space and time. *Earth and Planetary Science Letters* **470**, 73–86.
- Carpentier, M. (2007). Composition chimique des sédiments entrant dans la zone de subduction des Petites Antilles. Phd thesis, Université Joseph-Fourier - Grenoble I.

- Carpentier, M., Chauvel, C. & Mattielli, N. (2008). Pb–Nd isotopic constraints on sedimentary input into the Lesser Antilles arc system. *Earth and Planetary Science Letters* **272**, 199–211.
- Carpentier, M., Chauvel, C., Maury, R. C. & Mattielli, N. (2009). The “zircon effect” as recorded by the chemical and Hf isotopic compositions of Lesser Antilles forearc sediments. *Earth and Planetary Science Letters* **287**, 86–99.
- Carroll M. R. & Rutherford M. J. (1985). Sulfide and sulfate saturation in hydrous silicate melts. *Journal of Geophysical Research* **90**, 601–612.
- Carroll, M. R. & Rutherford, M. J. (1987). The Stability of Igneous Anhydrite: Experimental Results and Implications for Sulfur Behavior in the 1982 El Chichon Trachyandesite and Other Evolved Magmas. *Journal of Petrology* **28**, 781–801.
- Carroll, M. R. & Webster, J. D. (1994). Solubilities of sulfur, noble gases, nitrogen, chlorine, and fluorine in magmas. In : Holloway, J.R. & Carroll, M.R. (eds.). *Volatiles in Magmas*. Mineral. Soc. Amer., 231–280.
- Carter, L. B., Skora, S., Blundy, J. D., De Hoog, J. C. M. & Elliott, T. (2015). An Experimental Study of Trace Element Fluxes from Subducted Oceanic Crust. *Journal of Petrology* **56**, 1585–1606.
- Cervantes, P. & Wallace, P. J. (2003). Role of H₂O in subduction-zone magmatism: New insights from melt inclusions in high-Mg basalts from central Mexico. *Geology* **31**, 235–238.
- Chakhmouradian, A. R. & Mitchell, R. H. (1999). Niobian ilmenite, hydroxylapatite and sulfatian monazite; alternative hosts for incompatible elements in calcite kimberlite from Internatsional'naya, Yakutia. *The Canadian Mineralogist* **37**, 1177–1189.
- Chauvel, C., Goldstein, S. L. & Hofmann, A. W. (1995). Hydration and dehydration of oceanic crust controls Pb evolution in the mantle. *Chemical Geology* **126**, 65–75.
- Chauvel, C., Marini, J.-C., Plank, T. & Ludden, J. N. (2009). Hf–Nd input flux in the Izu–Mariana subduction zone and recycling of subducted material in the mantle. *Geochemistry, Geophysics, Geosystems* **10**, Q01001.
- Chen, Y.-X., Zheng, Y.-F., Chen, R.-X., Zhang, S.-B., Li, Q., Dai, M. & Chen, L. (2011). Metamorphic growth and recrystallization of zircons in extremely ¹⁸O-depleted rocks during eclogite-facies metamorphism: Evidence from U–Pb ages, trace elements, and O–Hf isotopes. *Geochimica et Cosmochimica Acta* **75**, 4877–4898.
- Chester, R. (1990). Marine sediments. In: Chester, R. (ed.) *Marine Geochemistry*. Dordrecht: Springer Netherlands, 441–467.

- Class, C., Miller, D. M., Goldstein, S. L. & Langmuir, C. H. (2000). Distinguishing melt and fluid subduction components in Umnak Volcanics, Aleutian Arc. *Geochemistry, Geophysics, Geosystems* **1**, 1004.
- Clemente, B., Scaillet, B. & Pichavant, M. (2004). The Solubility of Sulphur in Hydrous Rhyolitic Melts. *Journal of Petrology* **45**, 2171–2196.
- Condie, K. C. (1989). Geochemical changes in basalts and andesites across the Archean-Proterozoic boundary: Identification and significance. *Lithos* **23**, 1–18.
- Condomines, M. & Sigmarsson, O. (1993). Why are so many arc magmas close to ^{238}U - ^{230}Th radioactive equilibrium? *Geochimica et Cosmochimica Acta* **57**, 4491–4497.
- Connolly, J. A. D. & Galvez, M. E. (2018). Electrolytic fluid speciation by Gibbs energy minimization and implications for subduction zone mass transfer. *Earth and Planetary Science Letters* **501**, 90–102.
- Costa, F., Scaillet, B. & Pichavant, M. (2004). Petrological and Experimental Constraints on the Pre-eruption Conditions of Holocene Dacite from Volcán San Pedro (36°S, Chilean Andes) and the Importance of Sulphur in Silicic Subduction-related Magmas. *Journal of Petrology* **45**, 855–881.
- de Hoog, J. C. M., Mason, P. R. D. & van Bergen, M. J. (2001a). Sulfur and chalcophile elements in subduction zones: constraints from a laser ablation ICP-MS study of melt inclusions from Galunggung Volcano, Indonesia. *Geochimica et Cosmochimica Acta* **65**, 3147–3164.
- de Hoog, J. C. M., Taylor, B. E. & van Bergen, M. J. (2001b). Sulfur isotope systematics of basaltic lavas from Indonesia: implications for the sulfur cycle in subduction zones. *Earth and Planetary Science Letters* **189**, 237–252.
- de Hoog, J. C. M. & van Bergen, M. J. (2000). Volatile-induced transport of HFSE, REE, Th and U in arc magmas: evidence from zirconolite-bearing vesicles in potassic lavas of Lewotolo volcano (Indonesia). *Contributions to Mineralogy and Petrology* **139**, 485–502.
- Deer, W. A. (1962). Rock Forming Minerals. *Sheet Silicates 3*. Wiley.
- Delavault, H., Chauvel, C., Thomassot, E., Devey, C. W. & Dazas, B. (2016). Sulfur and lead isotopic evidence of relic Archean sediments in the Pitcairn mantle plume. *Proceedings of the National Academy of Sciences* **113**, 12952–12956.
- Devine, J. D., Gardner, J. E., Brack, H. P., Laynet, G. D. & Rutherford, M. J. (1995). Comparison of microanalytical methods for estimating H_2O contents of silicic volcanic glasses. *American Mineralogist* **80**, 319–328.

- Drummond, M. S., Defant, M. J. & Kepezhinskas, P. K. (1996). Petrogenesis of slab-derived trondhjemite–tonalite–dacite/adakite magmas. *Earth and Environmental Science Transactions of The Royal Society of Edinburgh*. Royal Society of Edinburgh Scotland Foundation **87**, 205–215.
- D’Souza, R. J. & Canil, D. (2018). The partitioning of chalcophile elements between sediment melts and fluids at 3 GPa, 950–1050°C with implications for slab fluids in subduction zones. *Earth and Planetary Science Letters* **498**, 215–225.
- Ellam, R. M. & Hawkesworth, C. J. (1988). Elemental and isotopic variations in subduction related basalts: evidence for a three component model. *Contributions to Mineralogy and Petrology* **98**, 72–80.
- Elliott, T. (2003). Tracers of the Slab. In: Eiler, J. (ed.) *Inside the Subduction Factory*. American Geophysical Union, 23–45.
- Elliott, T., Plank, T., Zindler, A., White, W. & Bourdon, B. (1997). Element transport from slab to volcanic front at the Mariana arc. *Journal of Geophysical Research: Solid Earth* **102**, 14991–15019.
- Evans, K. A. (2012). The redox budget of subduction zones. *Earth-Science Reviews* **113**, 11–32.
- Evans, K. A., Tomkins, A. G., Cliff, J. & Fiorentini, M. L. (2014). Insights into subduction zone sulfur recycling from isotopic analysis of eclogite-hosted sulfides. *Chemical Geology* **365**, 1–19.
- Foley, S., Tiepolo, M. & Vannucci, R. (2002). Growth of early continental crust controlled by melting of amphibolite in subduction zones. *Nature* **417**, 837–840.
- Fogel, R. A. & Rutherford, M. J. (1990). The solubility of carbon dioxide in rhyolitic melts: a quantitative FTIR study. *American Mineralogist* **75**, 1311–1326.
- Frezzotti, M. L. & Ferrando, S. (2015). The chemical behavior of fluids released during deep subduction based on fluid inclusions. *American Mineralogist*. GeoScienceWorld **100**, 352–377.
- Ganguly, J. (1972). Staurolite Stability and Related Parageneses: Theory, Experiments, and Applications. *Journal of Petrology* **13**, 335–365.
- Gertisser, R. & Keller, J. (2003). Trace Element and Sr, Nd, Pb and O Isotope Variations in Medium-K and High-K Volcanic Rocks from Merapi Volcano, Central Java, Indonesia: Evidence for the Involvement of Subducted Sediments in Sunda Arc Magma Genesis. *Journal of Petrology*. Oxford Academic **44**, 457–489.
- Goldhaber, M. B. (2003). Sulfur-rich Sediments. In: Holland, H.D., Turekian, K.K (eds.). *Treatise on Geochemistry* **7**, 407.

- Green, T. H. (1995). Significance of Nb/Ta as an indicator of geochemical processes in the crust-mantle system. *Chemical Geology* **120**, 347–359.
- Green, T. H. & Adam, J. (2003). Experimentally-determined trace element characteristics of aqueous fluid from partially dehydrated mafic oceanic crust at 3.0 GPa, 650–700°C. *European Journal of Mineralogy* **15**, 815–830.
- Guidotti, C. V. (1970). The Mineralogy and Petrology of the Transition from the Lower to Upper Sillimanite Zone in the Oquossoc Area, Maine. *Journal of Petrology*. Oxford Academic **11**, 277–336.
- Hawkesworth, C. J., Turner, S. P., McDermott, F., Peate, D. W. & Calsteren, P. van (1997). U-Th Isotopes in Arc Magmas: Implications for Element Transfer from the Subducted Crust. *Science*. American Association for the Advancement of Science **276**, 551–555.
- Hermann, J. (2002). Experimental constraints on phase relations in subducted continental crust. *Contributions to Mineralogy and Petrology* **143**, 219–235.
- Hermann, J. & Green, D. H. (2001). Experimental constraints on high pressure melting in subducted crust. *Earth and Planetary Science Letters* **188**, 149–168.
- Hermann, J. & Rubatto, D. (2009). Accessory phase control on the trace element signature of sediment melts in subduction zones. *Chemical Geology* **265**, 512–526.
- Hermann, J. & Spandler, C. J. (2008). Sediment Melts at Sub-arc Depths: an Experimental Study. *Journal of Petrology* **49**, 717–740.
- Hoffmann, J. E., Münker, C., Næraa, T., Rosing, M. T., Herwartz, D., Garbe-Schönberg, D. & Svahnberg, H. (2011). Mechanisms of Archean crust formation inferred from high-precision HFSE systematics in TTGs. *Geochimica et Cosmochimica Acta* **75**, 4157–4178.
- Holloway, J. R., Pan, V. & Gudmundsson, G. (1992). High-pressure fluid-absent melting experiments in the presence of graphite: oxygen fugacity, ferric/ferrous ratio and dissolved CO₂. *European Journal of Mineralogy* **4**, 105–114.
- Israel, C., Boyet, M., Doucelance, R., Bonnand, P., Frossard, P., Auclair, D. & Bouvier, A. (2020). Formation of the Ce-Nd mantle array: Crustal extraction vs. recycling by subduction. *Earth and Planetary Science Letters* **530**, 115941.
- Jacob, D. E. (2006). High Sensitivity Analysis of Trace Element-Poor Geological Reference Glasses by Laser Ablation-Inductively Coupled Plasma-Mass Spectrometry (LA-ICP-MS). *Geostandards and Geoanalytical Research* **30**, 221–235.
- Jégo, S. & Dasgupta, R. (2013). Fluid-present melting of sulfide-bearing ocean-crust: Experimental constraints on the transport of sulfur from subducting slab to mantle wedge. *Geochimica et Cosmochimica Acta* **110**, 106–134.

- Jégo, S. & Dasgupta, R. (2014). The Fate of Sulfur During Fluid-Present Melting of Subducting Basaltic Crust at Variable Oxygen Fugacity. *Journal of Petrology* **55**, 1019–1050.
- Jochum, K. P., Polat, A., Stoll, B. & Hofmann, A. W. (2001). Low Nb/Ta in the Archean mantle: implications for the missing Niobium in the silicate Earth. *EOS Trans* **82**, F1214.
- Jochum, K. P., Willbold, M., Raczek, I., Stoll, B. & Herwig, K. (2005). Chemical Characterisation of the USGS Reference Glasses GSA-1G, GSC-1G, GSD-1G, GSE-1G, BCR-2G, BHVO-2G and BIR-1G Using EPMA, ID-TIMS, ID-ICP-MS and LA-ICP-MS. *Geostandards and Geoanalytical Research* **29**, 285–302.
- Jochum, K.P, Stolz, A.J & Mcorist, G. (2000). Niobium and tantalum in carbonaceous chondrites: Constraints on the solar system and primitive mantle niobium/tantalum, zirconium/niobium, and niobium/uranium ratio. *Meteoritics & Planetary Science* **35**, 229–235.
- Johnson, M. C. & Plank, T. (1999). Dehydration and melting experiments constrain the fate of subducted sediments. *Geochemistry, Geophysics, Geosystems* **1**, 1007.
- Johnson, T. E., Brown, M., Gardiner, N. J., Kirkland, C. L. & Smithies, R. H. (2017). Earth's first stable continents did not form by subduction. *Nature*. Nature Publishing Group **543**, 239–242.
- Johnson, T. E., Kirkland, C. L., Gardiner, N. J., Brown, M., Smithies, R. H. & Santosh, M. (2019). Secular change in TTG compositions: Implications for the evolution of Archaean geodynamics. *Earth and Planetary Science Letters* **505**, 65–75.
- Jugo, P. (2009). Sulfur content at sulfide saturation in oxidized magmas. *Geology* **37**, 415–418.
- Jugo, P. J., Luth, R. W. & Richards, J. P. (2005). Experimental data on the speciation of sulfur as a function of oxygen fugacity in basaltic melts. *Geochimica et Cosmochimica Acta* **69**, 497–503.
- Kägi, R., Müntener, O., Ulmer, P. & Ottolini, L. (2005). Piston-cylinder experiments on H₂O undersaturated Fe-bearing systems: An experimental setup approaching f_{O_2} conditions of natural calc-alkaline magmas. *American Mineralogist* **90**, 708–717.
- Kamber, B. S. & Collerson, K. D. (2000). Role of 'hidden' deeply subducted slabs in mantle depletion. *Chemical Geology* **166**, 241–254.
- Kay, R. W. (1980). Volcanic Arc Magmas: Implications of a Melting-Mixing Model for Element Recycling in the Crust-Upper Mantle System. *The Journal of Geology*. The University of Chicago Press **88**, 497–522.

- Kelley, K. A. & Cottrell, E. (2009). Water and the Oxidation State of Subduction Zone Magmas. *Science* **325**, 605–607.
- Kelley, K. A., Plank, T., Farr, L., Ludden, J. & Staudigel, H. (2005). Subduction cycling of U, Th, and Pb. *Earth and Planetary Science Letters* **234**, 369–383.
- Kepezhinskas, P., Defant, M. J. & Drummond, M. S. (1996). Progressive enrichment of island arc mantle by melt-peridotite interaction inferred from Kamchatka xenoliths. *Geochimica et Cosmochimica Acta* **60**, 1217–1229.
- Kepezhinskas, P. K., Defant, M. J. & Drummond, M. S. (1995). Na Metasomatism in the Island-Arc Mantle by Slab Melt—Peridotite Interaction: Evidence from Mantle Xenoliths in the North Kamchatka Arc. *Journal of Petrology* **36**, 1505–1527.
- Keppler, H. (1996). Constraints from partitioning experiments on the composition of subduction-zone fluids. *Nature* **380**, 237–240.
- Kessel, R., Schmidt, M. W., Ulmer, P. & Pettke, T. (2005a). Trace element signature of subduction-zone fluids, melts and supercritical liquids at 120–180 km depth. *Nature* **437**, 724–727.
- Kessel, R., Ulmer, P., Pettke, T., Schmidt, M. W. & Thompson, A. B. (2005b). The water–basalt system at 4 to 6 GPa: Phase relations and second critical end point in a K-free eclogite at 700 to 1400 °C. *Earth and Planetary Science Letters* **237**, 873–892.
- Klemme, S., Prowatke, S., Hametner, K. & Günther, D. (2005). Partitioning of trace elements between rutile and silicate melts: Implications for subduction zones. *Geochimica et Cosmochimica Acta* **69**, 2361–2371.
- Klimm, K., Blundy, J. D. & Green, T. H. (2008). Trace Element Partitioning and Accessory Phase Saturation during H₂O-Saturated Melting of Basalt with Implications for Subduction Zone Chemical Fluxes. *Journal of Petrology* **49**, 523–553.
- Kovalenko, N. I. & Ryzhenko, B. N. (2009). Comparative study of the solubility of zircon and baddeleyite. *Geochemistry International* **47**, 405–413.
- Krenn, E., Putz, H., Finger, F. & Paar, W. H. (2011). Sulfur-rich monazite with high common Pb in ore-bearing schists from the Schellgaden mining district (Tauern Window, Eastern Alps). *Mineralogy and Petrology* **102**, 51.
- Li, H. & Hermann, J. (2015). Apatite as an indicator of fluid salinity: An experimental study of chlorine and fluorine partitioning in subducted sediments. *Geochimica et Cosmochimica Acta* **166**, 267–297.
- Li, J.-L., Gao, J., Klemm, R., John, T. & Wang, X.-S. (2016). Redox processes in subducting oceanic crust recorded by sulfide-bearing high-pressure rocks and veins (SW Tianshan, China). *Contributions to Mineralogy and Petrology* **171**, 72.

- Li, J.-L., Schwarzenbach, E. M., John, T., Ague, J. J., Huang, F., Gao, J., Klemd, R., Whitehouse, M. J. & Wang, X.-S. (2020). Uncovering and quantifying the subduction zone sulfur cycle from the slab perspective. *Nature Communications*. Nature Publishing Group **11**, 514.
- Li, L., Xiong, X. L. & Liu, X. C. (2017). Nb/Ta Fractionation by Amphibole in Hydrous Basaltic Systems: Implications for Arc Magma Evolution and Continental Crust Formation. *Journal of Petrology* **58**, 3–28.
- Li, Y. & Audéat, A. (2013) Gold solubility and partitioning between sulfide liquid, monosulfide solid solution and hydrous mantle melts: implications for crust–mantle differentiation and the formation of Au-rich magmas. *Geochimica et Cosmochimica Acta* **118**, 247–262.
- Li, Y. & Audéat, A. (2015). Effects of temperature, silicate melt composition, and oxygen fugacity on the partitioning of V, Mn, Co, Ni, Cu, Zn, As, Mo, Ag, Sn, Sb, W, Au, Pb, and Bi between sulfide phases and silicate melt. *Geochimica et Cosmochimica Acta* **162**, 25–45.
- Li, Y., Feng, L., Kiseeva, E. S., Gao, Z., Guo, H., Du, Z., Wang, F. & Shi, L. (2019). An essential role for sulfur in sulfide-silicate melt partitioning of gold and magmatic gold transport at subduction settings. *Earth and Planetary Science Letters* **528**, 115850.
- Li, Y.-H. & Schoonmaker, J. E. (2014). Chemical Composition and Mineralogy of Marine Sediments. In: Holland, H.D., Turekian, K.K (eds.). *Treatise on Geochemistry (Second Edition)*. Oxford: Elsevier, 1–32.
- Linnen, R. L. & Keppler, H. (2002). Melt composition control of Zr/Hf fractionation in magmatic processes. *Geochimica et Cosmochimica Acta* **66**, 3293–3301.
- Luhr, J. F. (1990). Experimental Phase Relations of Water- and Sulfur-Saturated Arc Magmas and the 1982 Eruptions of El Chichón Volcano. *Journal of Petrology* **31**, 1071–1114.
- Maimaiti, M., Fabbrizio, A., Carroll, M. R., Ertel-Ingrisch, W., Abudurehman, A., Paris, E. & Dingwell, D. B. (2019). Experimental study of monazite solubility in haplogranitic melts: a new model for peraluminous and peralkaline melts. *European Journal of Mineralogy* **31**, 49–59.
- Mallik, A., Nelson, J. & Dasgupta, R. (2015). Partial melting of fertile peridotite fluxed by hydrous rhyolitic melt at 2–3 GPa: implications for mantle wedge hybridization by sediment melt and generation of ultrapotassic magmas in convergent margins. *Contributions to Mineralogy and Petrology* **169**, 48.
- Mann, U. & Schmidt, M. W. (2015). Melting of pelitic sediments at subarc depths: 1. Flux vs. fluid-absent melting and a parameterization of melt productivity. *Chemical Geology* **404**, 150–167.

- Marschall, H. R. & Schumacher, J. C. (2012). Arc magmas sourced from mélange diapirs in subduction zones. *Nature Geoscience* **5**, 862–867.
- Martel, C., Pichavant, M., Bourdier, J.-L., Traineau, H., Holtz, F. & Scaillet, B. (1998). Magma storage conditions and control of eruption regime in silicic volcanoes: experimental evidence from Mt. Pelée. *Earth and Planetary Science Letters* **156**, 89–99.
- Martin, H. (1986). Effect of steeper Archean geothermal gradient on geochemistry of subduction-zone magmas. *Geology*. GeoScienceWorld **14**, 753–756.
- Martindale, M., Skora, S., Pickles, J., Elliott, T., Blundy, J. & Avanzinelli, R. (2013). High pressure phase relations of subducted volcanoclastic sediments from the west Pacific and their implications for the geochemistry of Mariana arc magmas. *Chemical Geology* **342**, 94–109.
- Massonne, H.-J. & Szpurka, Z. (1997). Thermodynamic properties of white micas on the basis of high-pressure experiments in the systems K_2O - MgO - Al_2O_3 - SiO_2 - H_2O and K_2O - FeO - Al_2O_3 - SiO_2 - H_2O . *Lithos* **41**, 229–250.
- McCuaig, T. C., Kerrich, R. & Xie, Q. (1994). Phosphorus and high field strength element anomalies in Archean high-magnesian magmas as possible indicators of source mineralogy and depth. *Earth and Planetary Science Letters* **124**, 221–239.
- McDade, P., Wood, B. J., Westrenen, W. V., Brooker, R., Gudmundsson, G., Soulard, H., Najorka, J. & Blundy, J. (2002). Pressure corrections for a selection of piston-cylinder cell assemblies. *Mineralogical Magazine*. Cambridge University Press **66**, 1021–1028.
- McDermott, F., Defant, M. J., Hawkesworth, C. J., Maury, R. C. & Joron, J. L. (1993). Isotope and trace element evidence for three component mixing in the genesis of the North Luzon arc lavas (Philippines). *Contributions to Mineralogy and Petrology* **113**, 9–23.
- McDonough, W. F. & Sun, S.-s. (1995). The composition of the Earth. *Chemical Geology* **120**, 223–253.
- Métrich, N., Schiano, P., Clocchiatti, R. & Maury, R. C. (1999). Transfer of sulfur in subduction settings: an example from Batan Island (Luzon volcanic arc, Philippines). *Earth and Planetary Science Letters* **167**, 1–14.
- Miller, D. M., Goldstein, S. L. & Langmuir, C. H. (1994). Cerium/lead and lead isotope ratios in arc magmas and the enrichment of lead in the continents. *Nature* **368**, 514–520.
- Montel, J.-M. (1993). A model for monazite/melt equilibrium and application to the generation of granitic magmas. *Chemical Geology* **110**, 127–146.
- Morris, J. D., Leeman, W. P. & Tera, F. (1990). The subducted component in island arc lavas: constraints from Be isotopes and B-Be systematics. *Nature* **344**, 31–36.

- Moyen, J.-F. (2011). The composite Archaean grey gneisses: Petrological significance, and evidence for a non-unique tectonic setting for Archaean crustal growth. *Lithos* **123**, 21–36.
- Münker, C., Pfänder, J. A., Weyer, S., Büchl, A., Kleine, T. & Mezger, K. (2003). Evolution of Planetary Cores and the Earth-Moon System from Nb/Ta Systematics. *Science*. American Association for the Advancement of Science **301**, 84–87.
- Münker, C., Wörner, G., Yogodzinski, G. & Churikova, T. (2004). Behaviour of high field strength elements in subduction zones: constraints from Kamchatka–Aleutian arc lavas. *Earth and Planetary Science Letters* **224**, 275–293.
- Næraa, T., Scherstén, A., Rosing, M. T., Kemp, A. I. S., Hoffmann, J. E., Kokfelt, T. F. & Whitehouse, M. J. (2012). Hafnium isotope evidence for a transition in the dynamics of continental growth 3.2 Gyr ago. *Nature*. Nature Publishing Group **485**, 627–630.
- Nash, W. P. & Crecraft, H. R. (1985). Partition coefficients for trace elements in silicic magmas. *Geochimica et Cosmochimica Acta* **49**, 2309–2322.
- Nebel, O., Vroon, P. Z., van Westrenen, W., Iizuka, T. & Davies, G. R. (2011). The effect of sediment recycling in subduction zones on the Hf isotope character of new arc crust, Banda arc, Indonesia. *Earth and Planetary Science Letters* **303**, 240–250.
- Nesbitt, B. E. (1986a). Oxide-sulfide-silicate equilibria associated with metamorphosed ore deposits; Part I, Theoretical considerations. *Economic Geology*. GeoScienceWorld **81**, 831–840.
- Nesbitt, B. E. (1986b). Oxide-sulfide-silicate equilibria associated with metamorphosed ore deposits; Part II, Pelitic and felsic volcanic terrains. *Economic Geology*. GeoScienceWorld **81**, 841–856.
- Nichols, G. T., Wyllie, P. J. & Stern, C. R. (1994). Subduction zone melting of pelagic sediments constrained by melting experiments. *Nature* **371**, 785–788.
- Parat, F., Holtz, F. & Feig, S. (2008). Pre-eruptive Conditions of the Huerto Andesite (Fish Canyon System, San Juan Volcanic Field, Colorado): Influence of Volatiles (C–O–H–S) on Phase Equilibria and Mineral Composition. *Journal of Petrology* **49**, 911–935.
- Pearce, J. A., Stern, R. J., Bloomer, S. H. & Fryer, P. (2005). Geochemical mapping of the Mariana arc-basin system: Implications for the nature and distribution of subduction components. *Geochemistry, Geophysics, Geosystems* **6**.
- Pichavant, M. (1987). The Macusani glasses, SE Peru: evidence of chemical fractionation in peraluminous magmas. *Magmatic Process: Physicochemical Principles*. *Geochem. Soc. Spec. Publ.* **1**, 359–373.

- Pichavant, M., Villaros, A., Deveaud, S., Scaillet, B. & Lahlafi, M. (2016). The Influence of Redox State On Mica Crystallization in Leucogranitic and Pegmatitic Liquids. *The Canadian Mineralogist* **54**, 559–581.
- Plank, T. (2005). Constraints from Thorium/Lanthanum on Sediment Recycling at Subduction Zones and the Evolution of the Continents. *Journal of Petrology* **46**, 921–944.
- Plank, T. (2014). The Chemical Composition of Subducting Sediments. In: Holland, H.D., Turekian, K.K (eds.). *Treatise on Geochemistry (Second Edition)*. Oxford: Elsevier, 607–629.
- Plank, T. & Langmuir, C. H. (1992). Effects of the melting regime on the composition of the oceanic crust. *Journal of Geophysical Research: Solid Earth* **97**, 19749–19770.
- Plank, T. & Langmuir, C. H. (1993). Tracing trace elements from sediment input to volcanic output at subduction zones. *Nature* **362**, 739–743.
- Plank, T. & Langmuir, C. H. (1998). The chemical composition of subducting sediment and its consequences for the crust and mantle. *Chemical Geology* **145**, 325–394.
- Poli, S. & Schmidt, M. W. (2002). Petrology of Subducted Slabs. *Annual Review of Earth and Planetary Sciences* **30**, 207–235.
- Pons, M.-L., Debret, B., Bouilhol, P., Delacour, A. & Williams, H. (2016). Zinc isotope evidence for sulfate-rich fluid transfer across subduction zones. *Nature Communications* **7**, 1–8.
- Popp, R. K., Gilbert, M. C. & Craig, J. R. (1977). Stability of Fe-Mg amphiboles with respect to oxygen fugacity. *American Mineralogist*. GeoScienceWorld **62**, 1–12.
- Powell, R. & Holland, T. (1990). Calculated mineral equilibria in the pelite system, KFMASH (K₂O-FeO-MgO-Al₂O₃-SiO₂-H₂O). *American Mineralogist* **75**, 367–380.
- Prouteau, G. & Scaillet, B. (2013). Experimental Constraints on Sulphur Behaviour in Subduction Zones: Implications for TTG and Adakite Production and the Global Sulphur Cycle since the Archean. *Journal of Petrology* **54**, 183–213.
- Prouteau, G., Scaillet, B., Pichavant, M. & Maury, R. (2001). Evidence for mantle metasomatism by hydrous silicic melts derived from subducted oceanic crust. *Nature* **410**, 197–200.
- Prouteau, G., Scaillet, B., Pichavant, M. & Maury, R. C. (1999). Fluid-present melting of ocean crust in subduction zones. *Geology* **27**, 1111–1114.
- Regelous, M., Collerson, K. D., Ewart, A. & Wendt, J. I. (1997). Trace element transport rates in subduction zones: evidence from Th, Sr and Pb isotope data for Tonga-Kermadec arc lavas. *Earth and Planetary Science Letters* **150**, 291–302.

- Reimink, J. R., Chacko, T., Stern, R. A. & Heaman, L. M. (2016). The birth of a cratonic nucleus: Lithogeochemical evolution of the 4.02–2.94 Ga Acasta Gneiss Complex. *Precambrian Research* **281**, 453–472.
- Rey, P. F. & Coltice, N. (2008). Neoproterozoic lithospheric strengthening and the coupling of Earth's geochemical reservoirs. *Geology* **36**, 635–638.
- Richardson, S. W. (1968). Staurolite Stability in a Part of the System Fe-Al-Si-O-H. *Journal of Petrology* **9**, 467–488.
- Rielli, A., Tomkins, A. G., Nebel, O., Brugger, J., Etschmann, B., Zhong, R., Yaxley, G.M. & Paterson, D. (2017). Evidence of sub-arc mantle oxidation by sulphur and carbon. *Geochemical Perspectives Letters* **3**, 124–132.
- Roberts, N. M. W. & Santosh, M. (2018). Capturing the Mesoarchean Emergence of Continental Crust in the Coorg Block, Southern India. *Geophysical Research Letters* **45**, 7444–7453.
- Rubatto, D. (2002). Zircon trace element geochemistry: partitioning with garnet and the link between U–Pb ages and metamorphism. *Chemical Geology* **184**, 123–138.
- Rubatto, D. & Hermann, J. (2007). Experimental zircon/melt and zircon/garnet trace element partitioning and implications for the geochronology of crustal rocks. *Chemical Geology* **241**, 38–61.
- Rudnick, R. L., Barth, M., Horn, I. & McDonough, W. F. (2000). Rutile-Bearing Refractory Eclogites: Missing Link Between Continents and Depleted Mantle. *Science*. American Association for the Advancement of Science **287**, 278–281.
- Ryan, J. G. & Chauvel, C. (2014). The Subduction-Zone Filter and the Impact of Recycled Materials on the Evolution of the Mantle. In: Holland, H.D., Turekian, K.K (eds.). *Treatise on Geochemistry (Second Edition)*. Oxford: Elsevier, 479–508.
- Ryerson, F. J. & Watson, E. B. (1987). Rutile saturation in magmas: implications for TiNbTa depletion in island-arc basalts. *Earth and Planetary Science Letters* **86**, 225–239.
- Salters, V. J. M. & Stracke, A. (2004). Composition of the depleted mantle. *Geochemistry, Geophysics, Geosystems* **5**, Q05B07.
- Scaillet, B., Clemente, B., Evans, B. W. & Pichavant, M. (1998). Redox control of sulfur degassing in silicic magmas. *Journal of Geophysical Research: Solid Earth* **103**, 23937–23949.
- Scaillet, B. & Evans, B. W. (1999). The 15 June 1991 Eruption of Mount Pinatubo. I. Phase Equilibria and Pre-eruption P–T–fO₂–fH₂O Conditions of the Dacite Magma. *Journal of Petrology* **40**, 381–411.

- Scaillet, B. & Macdonald, R. (2006). Experimental and Thermodynamic Constraints on the Sulphur Yield of Peralkaline and Metaluminous Silicic Flood Eruptions. *Journal of Petrology* **47**, 1413–1437.
- Scaillet, B. & Pichavant, M. (2003). Experimental constraints on volatile abundances in arc magmas and their implications for degassing processes. *Geological Society, London, Special Publications*. Geological Society of London **213**, 23–52.
- Scaillet, B., Pichavant, M. & Roux, J. (1995). Experimental Crystallization of Leucogranite Magmas. *Journal of Petrology* **36**, 663–705.
- Schiano, P., Clocchiatti, R., Shimizu, N., Maury, R. C., Jochum, K. P. & Hofmann, A. W. (1995). Hydrous, silica-rich melts in the sub-arc mantle and their relationship with erupted arc lavas. *Nature* **377**, 595–600.
- Schmidt, M. W. (1996). Experimental Constraints on Recycling of Potassium from Subducted Oceanic Crust. *Science* **272**, 1927–1930.
- Schmidt, M. W., Dardon, A., Chazot, G. & Vannucci, R. (2004a). The dependence of Nb and Ta rutile–melt partitioning on melt composition and Nb/Ta fractionation during subduction processes. *Earth and Planetary Science Letters* **226**, 415–432.
- Schmidt, M. W. & Jagoutz, O. (2017). The global systematics of primitive arc melts. *Geochemistry, Geophysics, Geosystems* **18**, 2817–2854.
- Schmidt, M. W. & Poli, S. (2014). Devolatilization During Subduction. In: Holland, H.D., Turekian, K.K (eds.). *Treatise on Geochemistry (Second Edition)*. Oxford: Elsevier, 669–701.
- Schmidt, M. W. & Ulmer, P. (2004). A rocking multianvil: elimination of chemical segregation in fluid-saturated high-pressure experiments. *Geochimica et Cosmochimica Acta* **68**, 1889–1899.
- Schmidt, M. W., Vielzeuf, D. & Auzanneau, E. (2004b). Melting and dissolution of subducting crust at high pressures: the key role of white mica. *Earth and Planetary Science Letters* **228**, 65–84.
- Smye, A.J., Greenwood, L.V. & Holland, J.B. (2010). Garnet–chloritoid–kyanite assemblages: eclogite facies indicators of subduction constraints in orogenic belts. *Journal of Metamorphic Geology* **28**, 753–768.
- Simon, G. & Chopin, C. (2001). Enstatite–sapphirine crack-related assemblages in ultrahigh-pressure pyrope megablasts, Dora-Maira massif, western Alps. *Contributions to Mineralogy and Petrology* **140**, 422–440.

- Sisson, T. W., Ratajeski, K., Hanks, W. B. & Glazner, A. F. (2005). Voluminous granitic magmas from common basaltic sources. *Contributions to Mineralogy and Petrology* **148**, 635–661.
- Skora, S. & Blundy, J. (2010). High-pressure Hydrous Phase Relations of Radiolarian Clay and Implications for the Involvement of Subducted Sediment in Arc Magmatism. *Journal of Petrology* **51**, 2211–2243.
- Skora, S. & Blundy, J. (2012). Monazite solubility in hydrous silicic melts at high pressure conditions relevant to subduction zone metamorphism. *Earth and Planetary Science Letters* **321–322**, 104–114.
- Skora, S., Blundy, J. D., Brooker, R. A., Green, E. C. R., de Hoog, J. C. M. & Connolly, J. A. D. (2015). Hydrous Phase Relations and Trace Element Partitioning Behaviour in Calcareous Sediments at Subduction-Zone Conditions. *Journal of Petrology* **56**, 953–980.
- Skora, S., Freymuth, H., Blundy, J., Elliott, T. & Guillong, M. (2017). An experimental study of the behaviour of cerium/molybdenum ratios during subduction: Implications for tracing the slab component in the Lesser Antilles and Mariana Arc. *Geochimica et Cosmochimica Acta* **212**, 133–155.
- Smit, M. A., Scherstén, A., Næraa, T., Emo, R. B., Scherer, E.E., Sprung, P., Bleeker, W., Mezger, K., Maltese, A., Cai, Y., Rasbury, E.T. & Whitehouse, M.J. (2019). Formation of Archean continental crust constrained by boron isotopes. *Geochemical Perspectives Letters* **12**, 23–26.
- Smithies, R.H., Champion, D.C. & Cassidy, K.F., 2003. Formation of Earth's early Archaean continental crust. *Precambrian Research* **127**, 89–101.
- Spandler, C., Pettke, T. & Hermann, J. (2014). Experimental study of trace element release during ultrahigh-pressure serpentinite dehydration. *Earth and Planetary Science Letters* **391**, 296–306.
- Stepanov, A. S. & Hermann, J. (2013). Fractionation of Nb and Ta by biotite and phengite: Implications for the “missing Nb paradox.” *Geology* **41**, 303–306.
- Stepanov, A. S., Hermann, J., Rubatto, D. & Rapp, R. P. (2012). Experimental study of monazite/melt partitioning with implications for the REE, Th and U geochemistry of crustal rocks. *Chemical Geology* **300–301**, 200–220.
- Stolper, E. M., Fine, G. J., Johnson, T. & Newman, S. (1987). The solubility of carbon dioxide in albitic melts. *American Mineralogist* **72**, 1071–1085.
- Syracuse, E. M., van Keken, P. E. & Abers, G. A. (2010). The global range of subduction zone thermal models. *Physics of the Earth and Planetary Interiors* **183**, 73–90.

- Tang, M., Lee, C.-T. A., Chen, K., Erdman, M., Costin, G. & Jiang, H. (2019). Nb/Ta systematics in arc magma differentiation and the role of arclogites in continent formation. *Nature Communications*. Nature Publishing Group **10**, 1–8.
- Tao, R., Zhang, L. & Zhang, L. (2020). Redox evolution of western Tianshan subduction zone and its effect on deep carbon cycle. *Geoscience Frontiers* **11**, 915–924.
- Thomsen, T. B. & Schmidt, M. W. (2008). The Biotite to Phengite Reaction and Mica-dominated Melting in Fluid + Carbonate-saturated Pelites at High Pressures. *Journal of Petrology* **49**, 1889–1914.
- Tomkins, A. G. & Evans, K. A. (2015). Separate zones of sulfate and sulfide release from subducted mafic oceanic crust. *Earth and Planetary Science Letters* **428**, 73–83.
- Tracy, R. J. & Robinson, P. (1988). Silicate-sulfide-oxide-fluid reactions in granulite-grade pelitic rocks, central Massachusetts. *American Journal of Science* **288**, 45–74.
- Trail, D., Boehnke, P., Savage, P. S., Liu, M.-C., Miller, M. L. & Bindeman, I. (2018). Origin and significance of Si and O isotope heterogeneities in Phanerozoic, Archean, and Hadean zircon. *Proceedings of the National Academy of Sciences*. National Academy of Sciences **115**, 10287–10292.
- Truckenbrodt, J., Ziegenbein, D. & Johannes, W. (1997). Redox conditions in piston-cylinder apparatus: The different behavior of boron nitride and unfired pyrophyllite assemblies. *American Mineralogist* **82**, 337–344.
- Turner, S., Caulfield, J., Turner, M., van Keken, P., Maury, R., Sandiford, M. & Prouteau, G. (2012). Recent contribution of sediments and fluids to the mantle's volatile budget. *Nature Geoscience* **5**, 50–54.
- Turner, S., Hawkesworth, C., Rogers, N., Bartlett, J., Worthington, T., Hergt, J., Pearce, J. & Smith, I. (1997). ²³⁸U/²³⁰Th disequilibria, magma petrogenesis, and flux rates beneath the depleted Tonga-Kermadec island arc. *Geochimica et Cosmochimica Acta* **61**, 4855–4884.
- Ulmer, P. & Trommsdorff, V. (1995). Serpentine Stability to Mantle Depths and Subduction-Related Magmatism. *Science* **268**, 858–861.
- Valley, J. W., Lackey, J.S., Cavosie, A.J., Clechenko, C. C., Spicuzza, C. C., Basei, M. A. S., Bindeman, I. N., Ferreira, V. P., Sial, A. N., King, E. M., Peck, W.H., Sinha, A. K. & Wei, C. S. (2005). 4.4 billion years of crustal maturation: oxygen isotope ratios of magmatic zircon. *Contributions to Mineralogy and Petrology* **150**, 561–580.
- van de Fliertdt, T., Goldstein, S. L., Hemming, S. R., Roy, M., Frank, M. & Halliday, A. N. (2007). Global neodymium–hafnium isotope systematics — revisited. *Earth and Planetary Science Letters* **259**, 432–441.

- van Keken, P. E., Hacker, B. R., Syracuse, E. M. & Abers, G. A. (2011). Subduction factory: 4. Depth-dependent flux of H₂O from subducting slabs worldwide. *Journal of Geophysical Research: Solid Earth* **116**, B01401.
- van Westrenen, W., Wood, B. J. & Blundy, J. D. (2001). A predictive thermodynamic model of garnet–melt trace element partitioning. *Contributions to Mineralogy and Petrology* **142**, 219–234.
- Vannucci, R., Tiepolo, M., Defant, M. J. & Kepezhinskas, P. (2007). The metasomatic record in the shallow peridotite mantle beneath Grenada (Lesser Antilles arc). *Lithos* **99**, 25–44.
- Wade, J. & Wood, B. J. (2001). The Earth's 'missing' niobium may be in the core. *Nature*. Nature Publishing Group **409**, 75–78.
- Wallace, P. J. & Edmonds, M. (2011). The Sulfur Budget in Magmas: Evidence from Melt Inclusions, Submarine Glasses, and Volcanic Gas Emissions. *Reviews in Mineralogy and Geochemistry* **73**, 215–246.
- Walters, J. B., Cruz-Uribe, A. M. & Marschall, H. R. (2019). Isotopic Compositions of Sulfides in Exhumed High-Pressure Terranes: Implications for Sulfur Cycling in Subduction Zones. *Geochemistry, Geophysics, Geosystems* 2019GC008374.
- Walters, J. B., Cruz-Uribe, A. M. & Marschall, H. R. (2020). Sulfur loss from subducted altered oceanic crust and implications for mantle oxidation. *Geochemical Perspectives Letters* 36–41.
- Webster, J. D., Vetere, F., Botcharnikov, R. E., Goldoff, B., McBirney, A. & Doherty, A. L. (2015). Experimental and modeled chlorine solubilities in aluminosilicate melts at 1 to 7000 bars and 700 to 1250 °C: Applications to magmas of Augustine Volcano, Alaska. *American Mineralogist* **100**, 522–535.
- Wei, C. & Powell, R. (2003). Phase relations in high-pressure metapelites in the system KFMASH (K₂O–FeO–MgO–Al₂O₃–SiO₂–H₂O) with application to natural rocks. *Contributions to Mineralogy and Petrology* **145**, 301–315.
- White, W. M. & Patchett, J. (1984). Hf–Nd–Sr isotopes and incompatible element abundances in island arcs: implications for magma origins and crust–mantle evolution. *Earth and Planetary Science Letters* **67**, 167–185.
- Woodhead, J. D., Hergt, J. M., Davidson, J. P. & Eggins, S. M. (2001). Hafnium isotope evidence for 'conservative' element mobility during subduction zone processes. *Earth and Planetary Science Letters* **192**, 331–346.
- Xiong, X., Keppler, H., Audétat, A., Ni, H., Sun, W. & Li, Y. (2011). Partitioning of Nb and Ta between rutile and felsic melt and the fractionation of Nb/Ta during partial melting of hydrous metabasalt. *Geochimica et Cosmochimica Acta* **75**, 1673–1692.

- Yardley, B. W. D. (1977). Relationships between the chemical and modal compositions of metapelites from Connemara, Ireland. *Lithos* **10**, 235–242.
- Zajacz, Z. (2015). The effect of melt composition on the partitioning of oxidized sulfur between silicate melts and magmatic volatiles. *Geochimica et Cosmochimica Acta* **158**, 223–244.
- Zhang, Y. (1999). H₂O in rhyolitic glasses and melts: measurement, speciation, solubility, and diffusion. *Reviews of Geophysics* **37**, 493–516.
- Zhang, Z.-M., Shen, K., Sun, W.-D., Liu, Y.-S., Liou, J. G., Shi, C. & Wang, J.-L. (2008). Fluids in deeply subducted continental crust: Petrology, mineral chemistry and fluid inclusion of UHP metamorphic veins from the Sulu orogen, eastern China. *Geochimica et Cosmochimica Acta* **72**, 3200–3228.

FIGURE CAPTIONS

Fig. 1: Trace element compositions of B12a (starting composition of this study) and GLOSS-II (Plank, 2014) normalized to PM (Primitive Mantle; McDonough & Sun, 1995). Blue area corresponds to IAB (MgO > 6 wt. %) containing unambiguously a sedimentary component in their source, according to the Elliott (2003) criteria ($Ba/Th < 150$ and $La/Sm_{PM} > 1$) (n= 408 samples, GeoRoc compilation; Supplementary Data 5).

Fig. 2: Representative back-scattered electron (BSE) images of experimental run products (3 GPa, 8.5 wt. % H₂O). Phases abbreviations: Rt, rutile; Zrn, zircon; St, staurolite; Qz, quartz; Grt, garnet; Ky, kyanite; Po, pyrrhotite; Opx, orthopyroxene; Bt, biotite.

Fig. 3: Cumulative modes (calculated from mass balance on the major oxides, Table 2) for experimental charges, plotted against sulphur addition (S_{in}).

Fig. 4: T-wt. % S_{in} stability fields of different parageneses of the main minerals in subducted Ca-poor pelite. The approximate stability limits of key phases are indicated; the curves are labelled with mineral lying inside their respective stability fields. Abbreviations as in Fig. 2 + Ph = phengite and Gl = glass.

Fig. 5: (a) Garnet compositions plotted in molecular proportions of grossular (Grs), almandine (Alm), pyrope (Prp) and spessartine (Sps); (b,c) variations of X_{Mg} and Ca (in cations per formula unit (pfu)) in garnet as a function of temperature. Data from previous studies are represented by grey symbols.

Fig. 6: Variations of Si and Al (in cations pfu) in phengite (a) and biotite (b), after Thomsen & Schmidt (2008); variations of X_{Mg} in phengite (c) and biotite (d) as a function of temperature. Data from previous studies are represented by grey symbols.

Fig. 7: Experimental glass compositions: (a) A/CNK as a function of NK/A; (b, c, d, e, f) variations of melt composition with temperature; (g) anorthite-albite–orthoclase normative triangle; To, tonalite; Tdh, trondhjemite; Gd, granodiorite.

Fig. 8: Sulphur contents (ppm) of experimental glasses as a function of temperature for B12a \pm S (a) and B12a + H₂O \pm H₂SO₄ (b). Vertical bars are 1 standard deviation (when not shown error bars are smaller than the symbol size). Grey symbols show the sulphur content of experimental silicic glasses saturated in sulphide and/or sulphate at 2.3-3 GPa, 700 to 1100°C and $fO_2 = FMQ-4$ to $FMQ+3.5$ (Prouteau & Scaillet, 2013; Jégo & Dasgupta, 2013, 2014; Canil & Fellows, 2017; D’Souza & Canil, 2018).

B12a: Ca-poor pelite with 1-4 wt. % S_{in}; TSC: carbonate-rich sediment with 2 wt. % S_{in}; GM: Ca-rich synthetic pelite with 0.3-1 wt. % S_{in}; CM3: Ca-rich pelite with 2 wt. % S_{in}; PM: Fe-rich pelite with 1.9 wt. % S_{in}.

Fig. 9: (a) Trace element compositions of experimental glasses normalized to PM (McDonough & Sun, 1995). Starting composition is shown as thick black line. Blue area corresponds to IAB with “sediment flavor” (see Fig. 1 for details); (b, c, d, e, f, g) variation of concentration of trace elements (ppm) as a function of temperature.

Fig. 10: Garnet-melt (a), orthopyroxene-melt (b), biotite-melt (c) and phengite-melt (d) partition coefficients for the trace elements studied. Garnet-melt partition coefficients are compared to the coefficients of Skora & Blundy (2010) (grey area in (a)).

Fig. 11: Melt productivity at 3 GPa calculated from mass balance (Table 2) as a function of temperature.

Fig. 12: Element fractionation in hydrous melts as a function of temperature. $(\text{Ba/Th})_N = (\text{Ba/Th})_{\text{melt}}/(\text{Ba/Th})_{\text{starting material}}$ etc.

$$\text{Zr/Zr}^* = \text{Zr}/10^{((\log\text{Nd} + \log\text{Sm})/2)} \text{ (McCuaig } et al., 1994).$$

Fig. 13: (a) $(\text{La/Sm})_{\text{PM}}$ (McDonough & Sun, 1995) versus Ba/Th and (b) Th versus U/Th for mafic ($\text{MgO} > 6$ wt. %) arc lavas worldwide, including the Lesser Antilles (compilation from GeoRoc: <http://georoc.mpch-mainz.gwdg.de>; see Supplementary Data 5 for references).

Superimposed are the chemical compositions of the experimental glasses of this study, as well as the experiments of Skora *et al.* (2015, 2017).

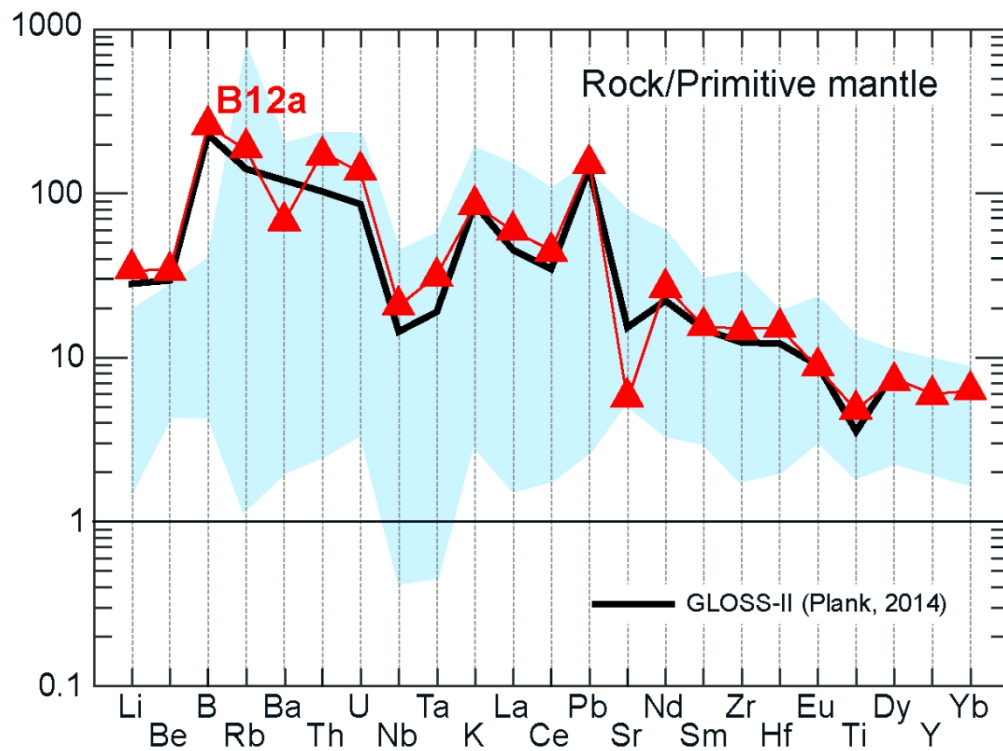


Fig. 1: Trace element compositions of B12a (starting composition of this study) and GLOSS-II (Plank, 2014) normalized to PM (Primitive Mantle; McDonough & Sun, 1995). Blue area corresponds to IAB (MgO > 6 wt. %) containing unambiguously a sedimentary component in their source, according to the Elliott (2003) criteria ($Ba/Th < 150$ and $La/Sm_{PM} > 1$) (n= 408 samples, GeoRoc compilation; Supplementary Data 5).

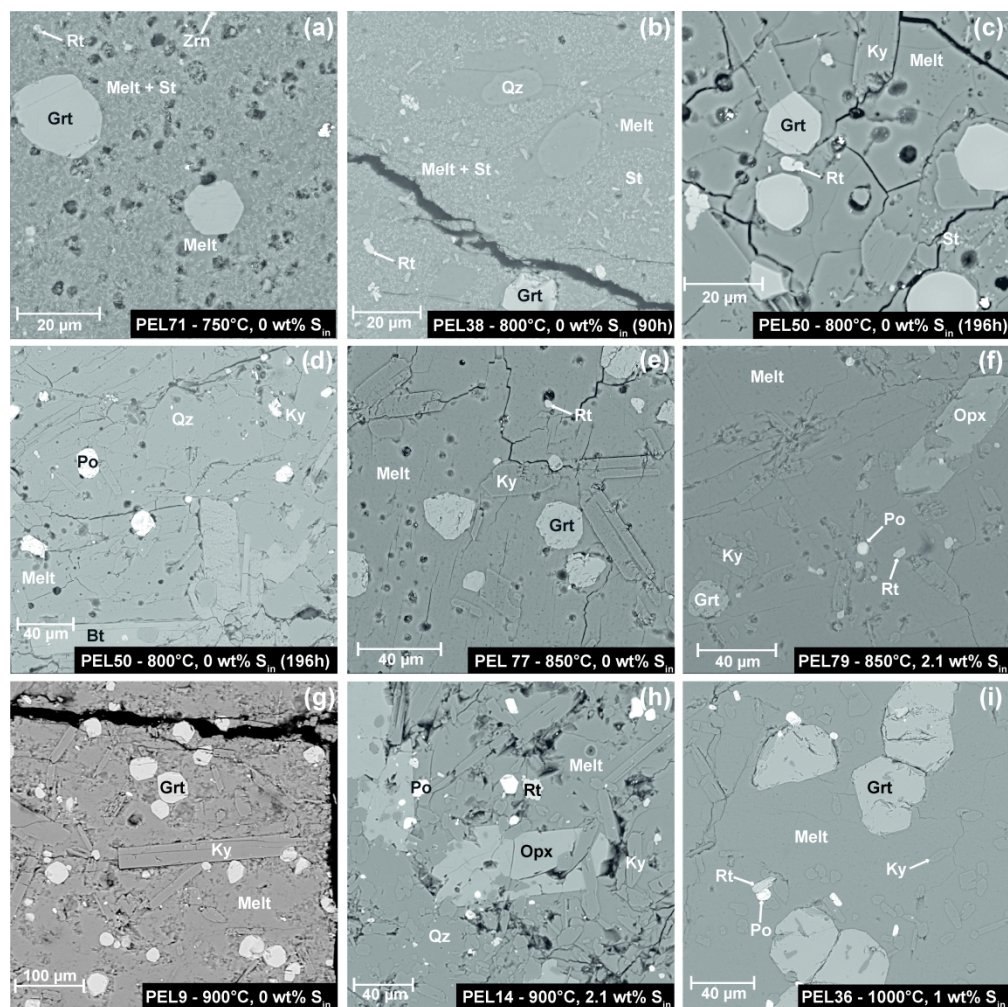


Fig. 2: Representative back-scattered electron (BSE) images of experimental run products (3 GPa, 8.5 wt. % H₂O). Phases abbreviations: Rt, rutile; Zrn, zircon; St, staurolite; Qz, quartz; Grt, garnet; Ky, kyanite; Po, pyrrhotite; Opx, orthopyroxene; Bt, biotite.

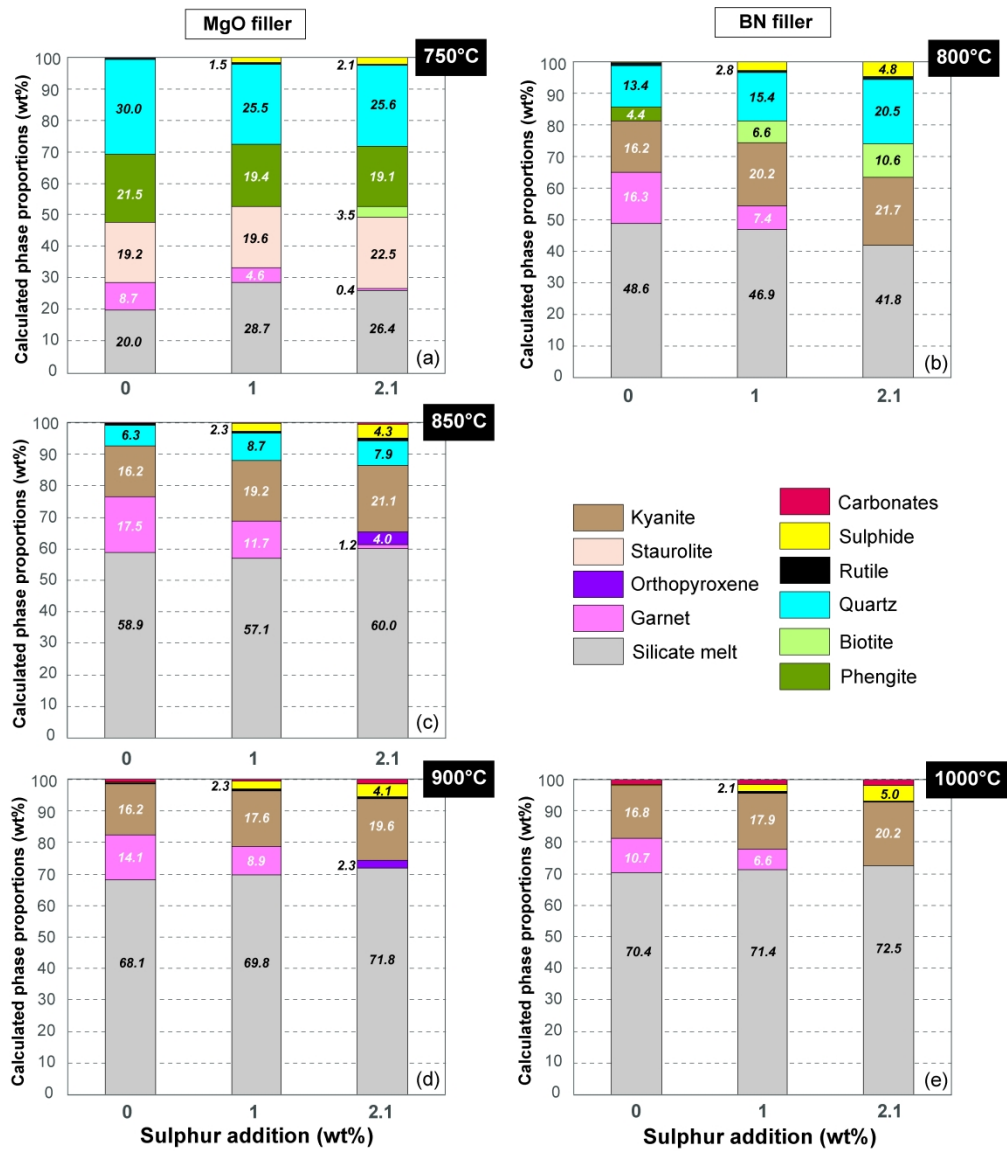


Fig. 3: Cumulative modes (calculated from mass balance on the major oxides, Table 2) for experimental charges, plotted against sulphur addition (S_{in}).

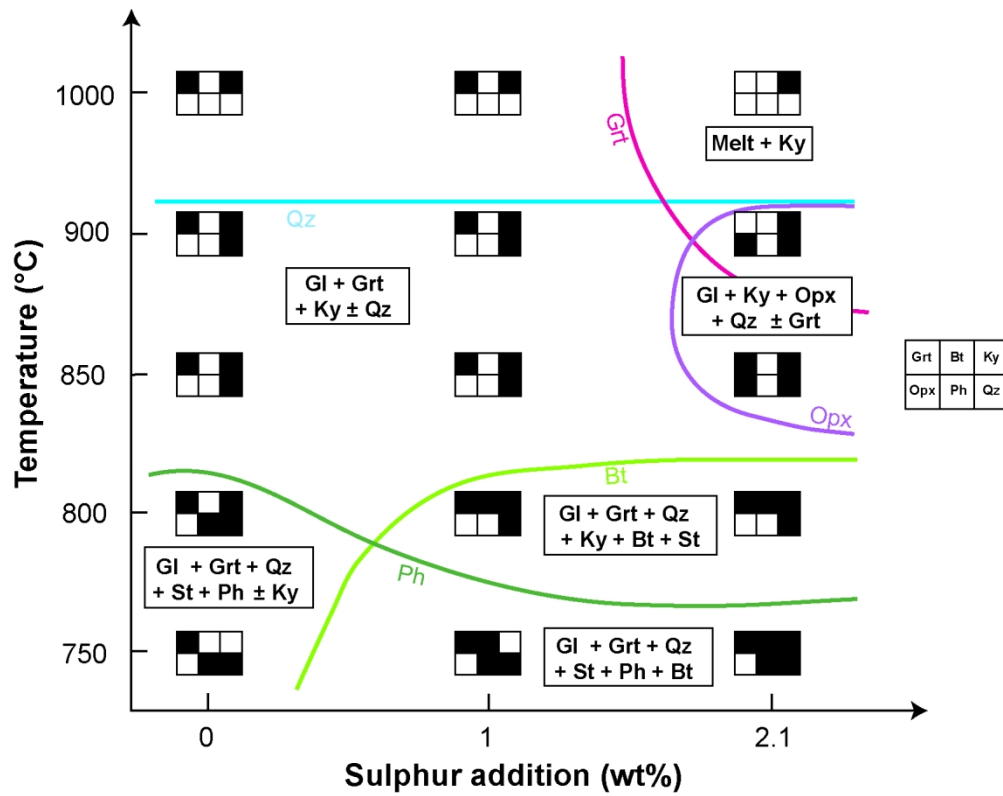


Fig. 4: T-wt. % S_{in} stability fields of different parageneses of the main minerals in subducted Ca-poor pelite. The approximate stability limits of key phases are indicated; the curves are labelled with mineral lying inside their respective stability fields. Abbreviations as in Fig. 2 + Ph = phengite and Gl = glass.

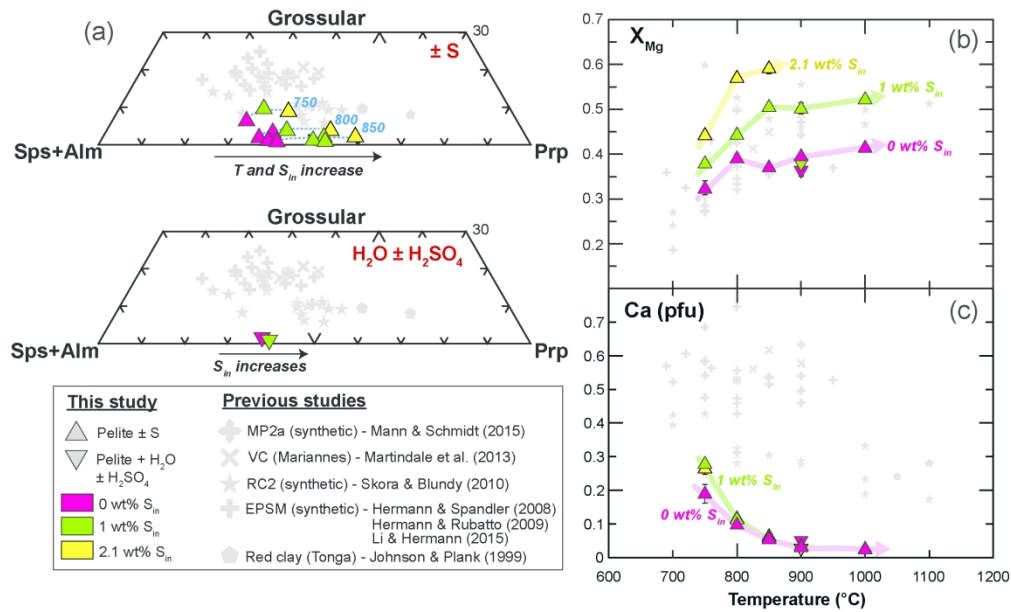


Fig. 5: (a) Garnet compositions plotted in molecular proportions of grossular (Grs), almandine (Alm), pyrope (Prp) and spessartine (Sps); (b,c) variations of X_{Mg} and Ca (in cations per formula unit (pfu)) in garnet as a function of temperature. Data from previous studies are represented by grey symbols.

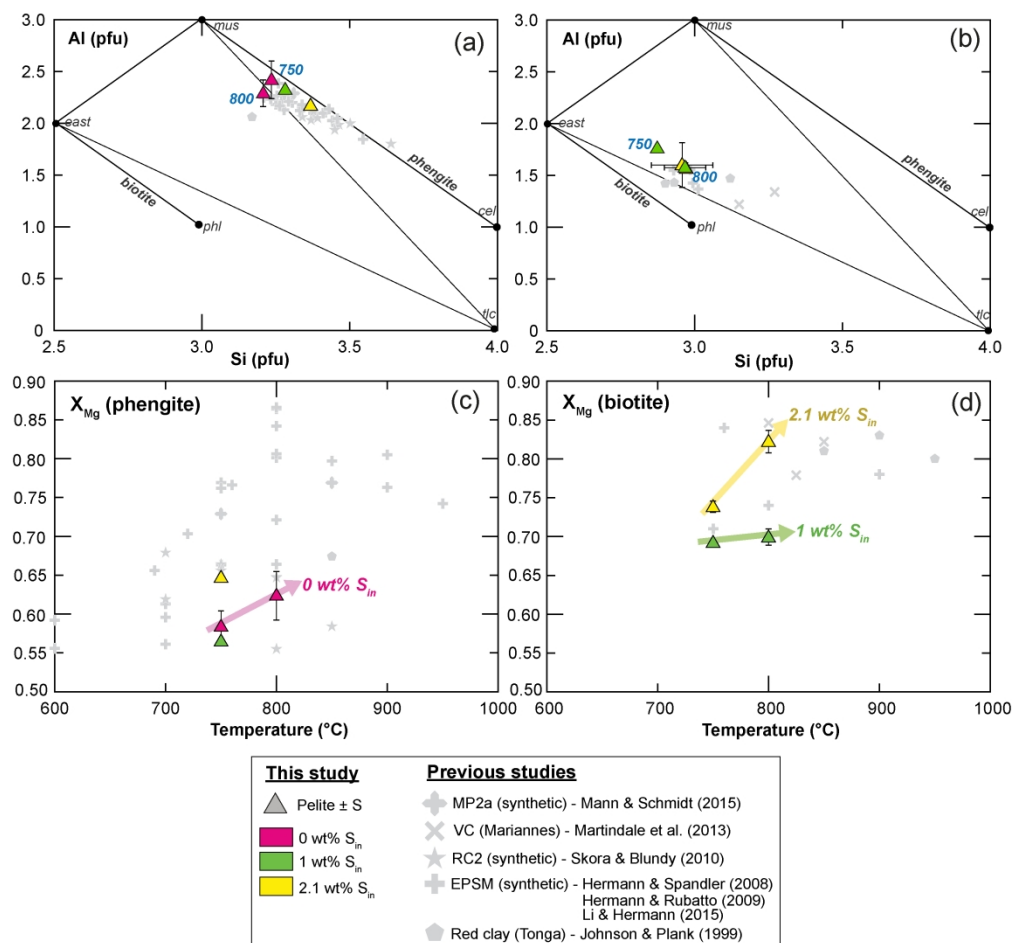


Fig. 6: Variations of Si and Al (in cations pfu) in phengite (a) and biotite (b), after Thomsen & Schmidt (2008); variations of X_{Mg} in phengite (c) and biotite (d) as a function of temperature. Data from previous studies are represented by grey symbols.

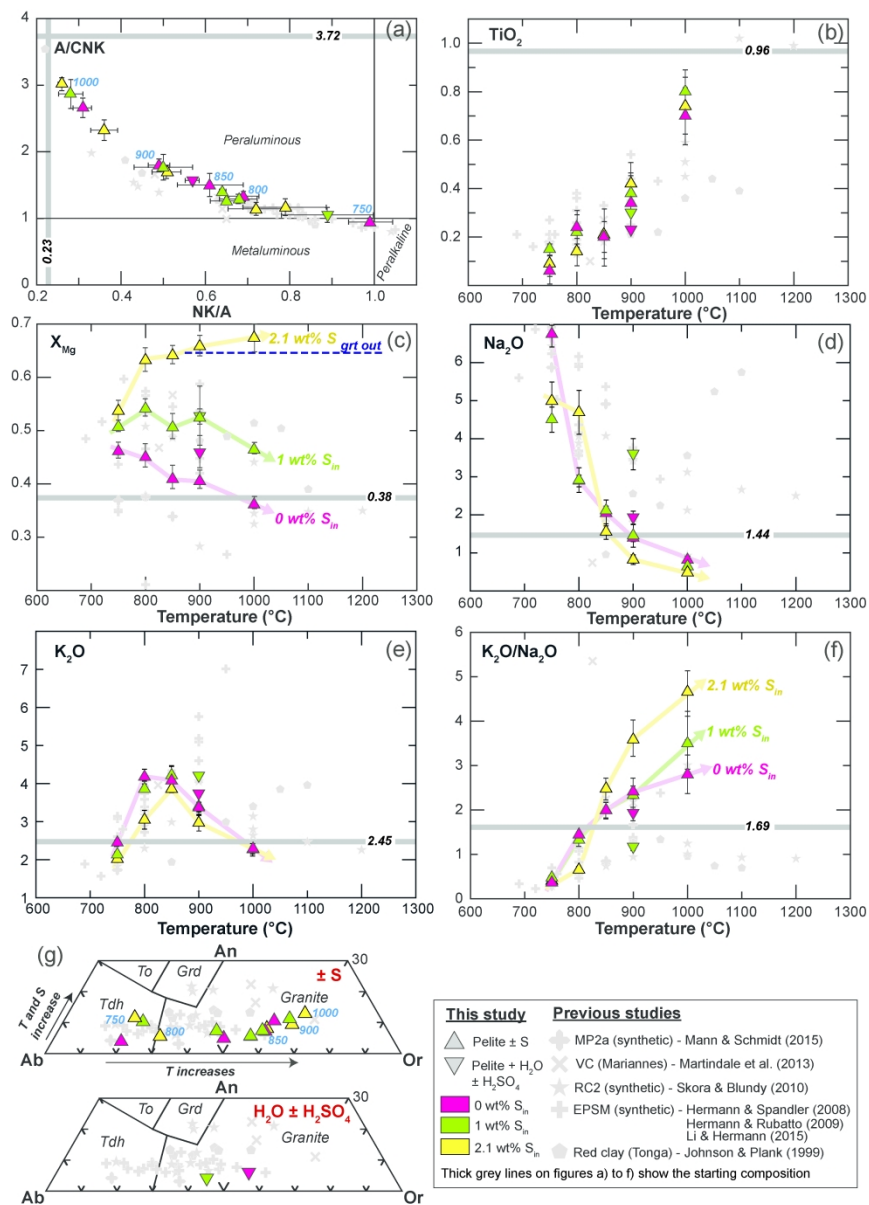


Fig. 7: Experimental glass compositions: (a) A/CNK as a function of NK/A; (b, c, d, e, f) variations of melt composition with temperature; (g) anorthite-albite-orthoclase normative triangle; To, tonalite; Tdh, trondhjemite; Gd, granodiorite.

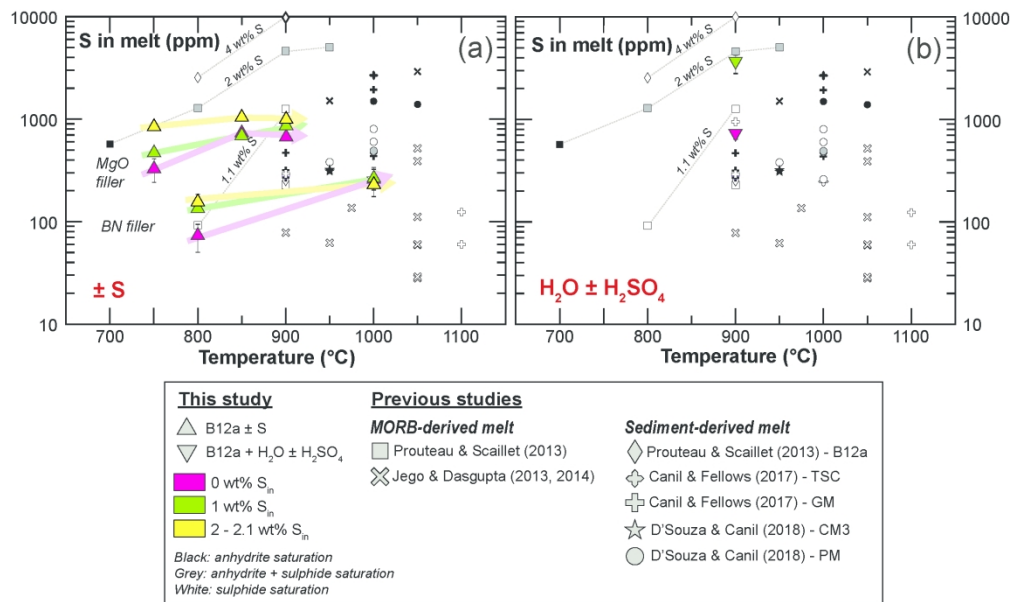


Fig. 8: Sulphur contents (ppm) of experimental glasses as a function of temperature for B12a ± S (a) and B12a + H₂O ± H₂SO₄ (b). Vertical bars are 1 standard deviation (when not shown error bars are smaller than the symbol size). Grey symbols show the sulphur content of experimental silicic glasses saturated in sulphide and/or sulphate at 2.3-3 GPa, 700 to 1100°C and $fO_2 = FMQ-4$ to $FMQ+3.5$ (Prouteau & Scaillet, 2013; Jégo & Dasgupta, 2013, 2014; Canil & Fellows, 2017; D'Souza & Canil, 2018).

B12a: Ca-poor pelite with 1-4 wt. % S_{in}; TSC: carbonate-rich sediment with 2 wt. % S_{in}; GM: Ca-rich synthetic pelite with 0.3-1 wt. % S_{in}; CM3: Ca-rich pelite with 2 wt. % S_{in}; PM: Fe-rich pelite with 1.9 wt. % S_{in}.

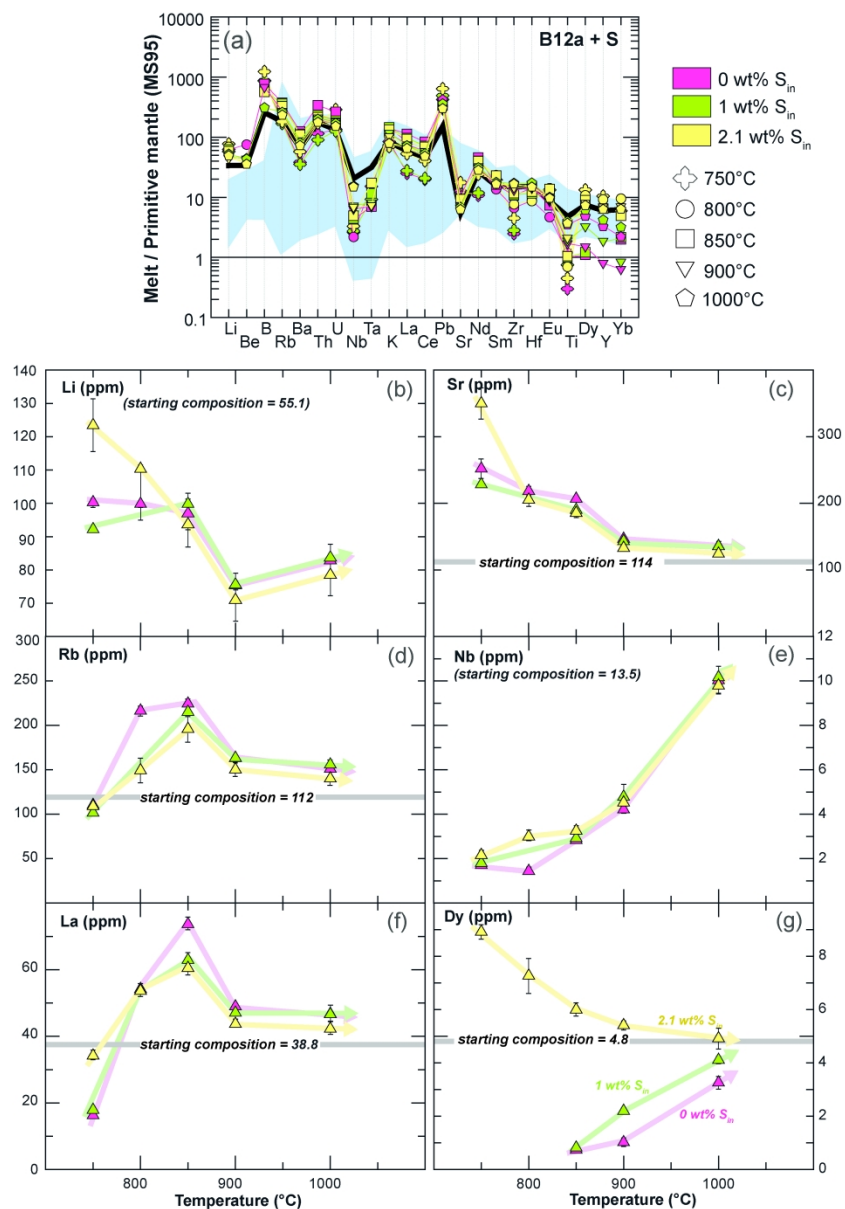


Fig. 9: (a) Trace element compositions of experimental glasses normalized to PM (McDonough & Sun, 1995). Starting composition is shown as thick black line. Blue area corresponds to IAB with "sediment flavor" (see Fig. 1 for details); (b, c, d, e, f, g) variation of concentration of trace elements (ppm) as a function of temperature.

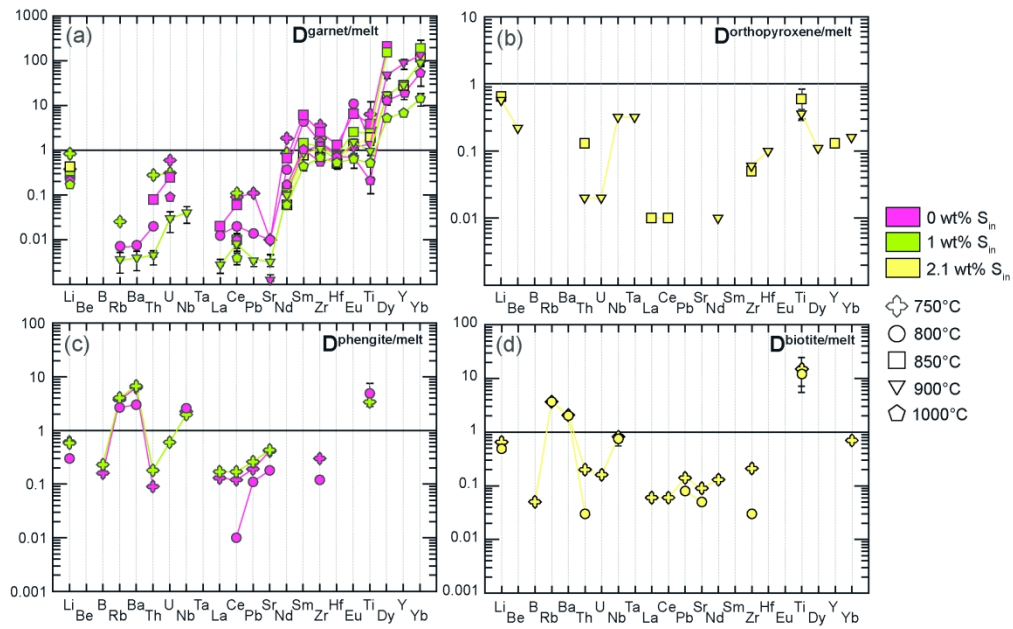


Fig. 10: Garnet-melt (a), orthopyroxene-melt (b), biotite-melt (c) and phengite-melt (d) partition coefficients for the trace elements studied. Garnet-melt partition coefficients are compared to the coefficients of Skora & Blundy (2010) (grey area in (a)).

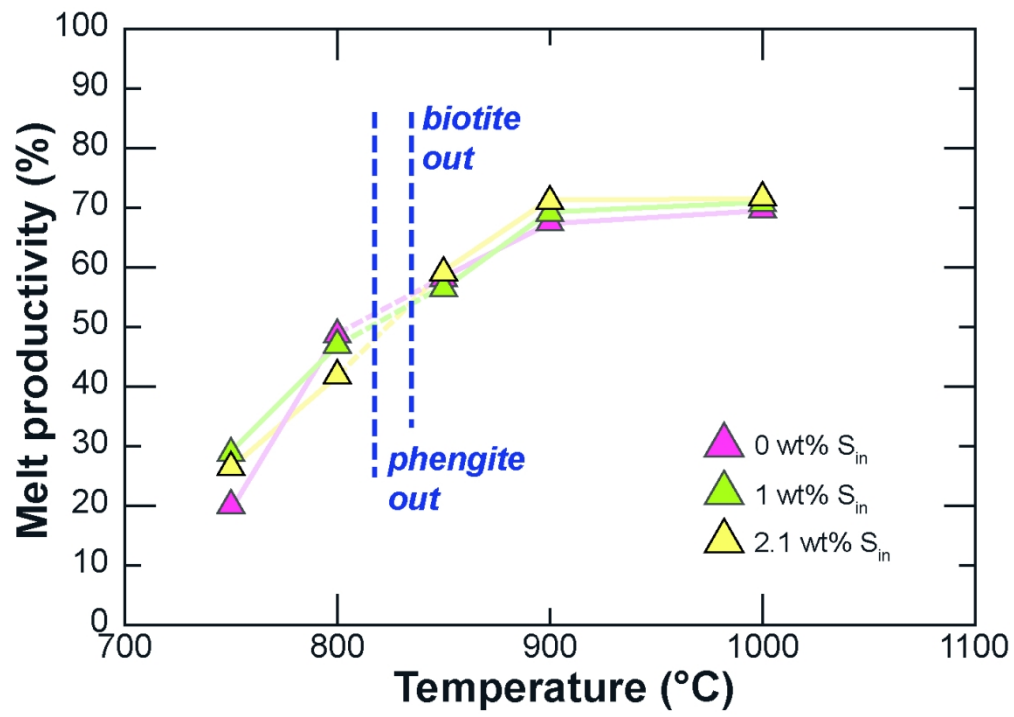


Fig. 11: Melt productivity at 3 GPa calculated from mass balance (Table 2) as a function of temperature.

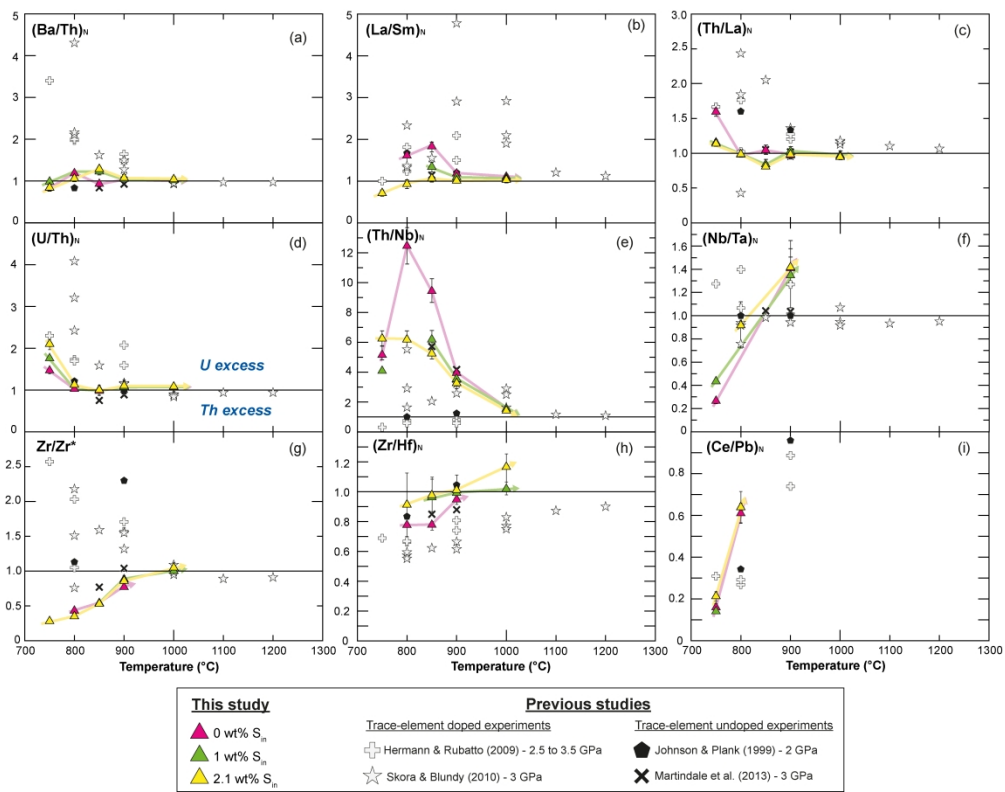


Fig. 12: Element fractionation in hydrous melts as a function of temperature. $(Ba/Th)_N = (Ba/Th)_{melt}/(Ba/Th)_{starting\ material}$ etc.
 $Zr/Zr^* = Zr/10^{((\log Nd + \log Sm)/2)}$ (McCuaig et al., 1994).

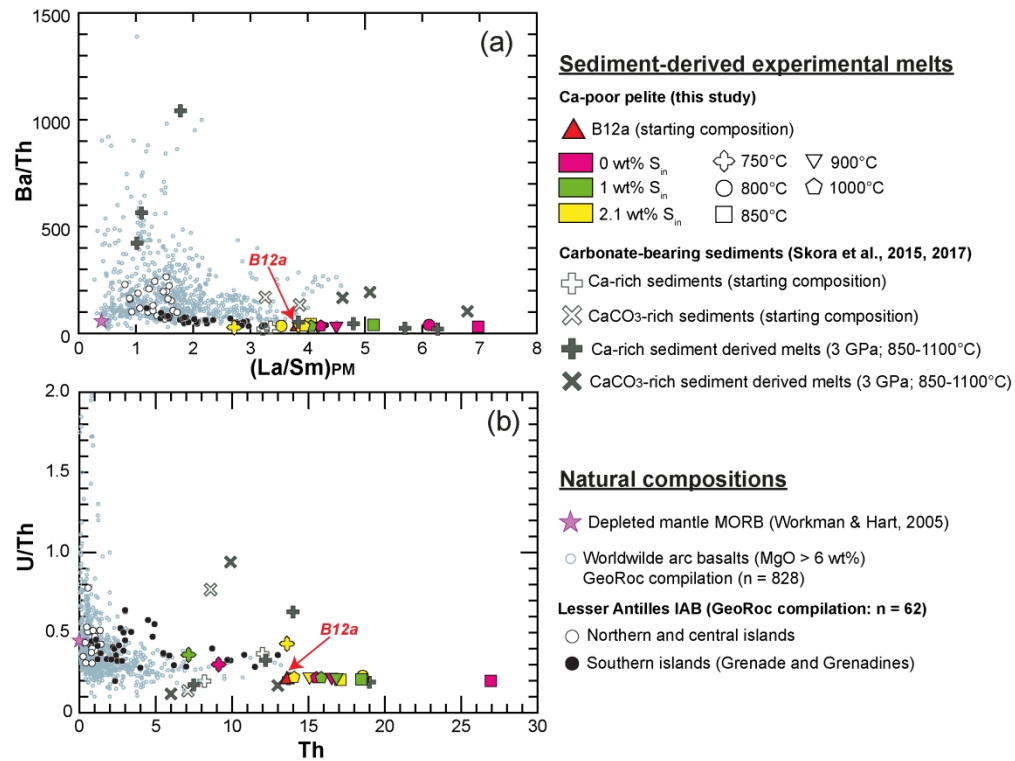


Fig. 13: (a) $(La/Sm)_{PM}$ (McDonough & Sun, 1995) versus Ba/Th and (b) Th versus U/Th for mafic (MgO > 6 wt. %) arc lavas worldwilde, including the Lesser Antilles (compilation from GeoRoc: <http://georoc.mpch-mainz.gwdg.de>; see Supplementary Data 5 for references). Superimposed are the chemical compositions of the experimental glasses of this study, as well as the experiments of Skora et al. (2015, 2017).

Table 1: Starting composition in comparison with natural compositions

| | B12a | B12a⁽¹⁾ | GLOSS-II⁽¹⁾ | S. Ant. Sed.⁽¹⁾ |
|-----------------------------------|-------------|---------------------------|-------------------------------|-----------------------------------|
| <i>wt%</i> | | | | |
| SiO ₂ | 58.49 | 64.80 | 63.08 | 70.78 |
| TiO ₂ | 0.87 | 0.96 | 0.71 | 0.79 |
| Al ₂ O ₃ | 19.35 | 21.44 | 13.94 | 13.82 |
| FeO _{total} | 5.59 | 6.19 | 6.32 | 5.47 |
| FeO | 1.67 | 1.85 | - | - |
| MnO | 0.04 | 0.04 | 0.48 | 0.09 |
| MgO | 1.95 | 2.16 | 3.06 | 2.26 |
| CaO | 0.36 | 0.40 | 6.93 | 1.18 |
| Na ₂ O | 1.31 | 1.45 | 2.79 | 3.01 |
| K ₂ O | 2.21 | 2.45 | 2.46 | 2.18 |
| P ₂ O ₅ | 0.09 | 0.10 | 0.22 | 0.40 |
| LOI | 8.53 | - | - | - |
| Total | 98.79 | 100.00 | 100.00 | 100.00 |
| CO ₂ | 1.03 | - | - | - |
| H ₂ O _{total} | 8.53 | - | - | - |
| H ₂ O ⁻ | 2.53 | - | - | - |
| S | 0.09 | - | - | - |
| F | 0.056 | - | - | - |
| Cl | 0.057 | - | - | - |
| <i>Molar ratios</i> | | | | |
| K/Na | - | 1.11 | 0.58 | 0.48 |
| A/CNK | - | 3.72 | 0.70 | 1.46 |
| NK/A | - | 0.23 | 0.52 | 0.53 |
| X _{Mg} | - | 0.38 | 0.46 | 0.42 |
| X _{Ca} | - | 0.05 | 0.43 | 0.14 |

(1): volatile-free. Normalized to 100%.

GLOSS-II: GLOBal Subducting Sediment and. Ant. Sed.: South Antilles Sediments (Plank, 2014).

LOI: Loss On Ignition.

A/CNK = Al/(Na+K+2Ca); NK/A = (Na+K)/Al;

X_{Mg}: MgO/(MgO+FeO_T); X_{Ca} = CaO/(CaO+Mg+FeO_T); all molar.

Table 2 : Experimental conditions and phase proportions (P = 3 GPa)

| Run | T (°C) | Time (hours) | Ass. | H ₂ O (wt%) | S _{in} (wt%) | Runproducts (%) | | | | | | | | | | | | | | |
|---|-----------|-----------------|------|---------------------------|--------------------------|-----------------|-------------|-----|-------------|-----------|------|------|------------|------------|-----------|-----------|-------|-----|-----------------|----------|
| | | | | | | Melt | Grt | Opx | Ky | St | Bt | Ph | Rt | Ti-Mag | Qz | Po | Cl ph | Cb | ΣR ² | Others |
| <i>B12a + H₂O ± H₂SO₄</i> | | | | | | | | | | | | | | | | | | | | |
| PEL68h | 900 | 94 | MgO | 15.02 | 0 | 66.3 | 14.7 | - | 17.0 | tr | - | - | 0.8 | - | 1.3 | - | - | - | 1.6 | Zrn |
| PEL69h | 900 | 94 | MgO | 15.21 | 1 | <i>68.7</i> | <i>10.0</i> | - | <i>19.9</i> | <i>tr</i> | - | - | <i>0.4</i> | <i>1.0</i> | <i>tr</i> | <i>tr</i> | - | - | <i>66.6</i> | Zrn |
| <i>B12a ± elemental S</i> | | | | | | | | | | | | | | | | | | | | |
| PEL71 | 750 | 241 | MgO | 8.53 | 0 | 20.0 | 8.7 | - | - | 19.2 | - | 21.5 | 0.6 | - | 30.0 | tr | - | - | 0.5 | Mnz, Zrn |
| PEL72 | 750 | 241 | MgO | 8.53 | 1 | 28.7 | 4.6 | - | - | 19.6 | tr | 19.4 | 0.6 | - | 25.5 | 1.5 | - | - | 0.9 | Mnz, Zrn |
| PEL73 | 750 | 241 | MgO | 8.53 | 2.1 | 26.4 | 0.4 | - | tr | 22.5 | 3.5 | 19.1 | 0.5 | - | 25.6 | 2.1 | - | - | 0.0 | Mnz, Zrn |
| PEL50 | 800 | 196 | BN | 8.53 | 0 | 48.6 | 16.3 | - | 16.2 | tr | - | 4.4 | 0.7 | - | 13.4 | 0.4 | - | - | 0.1 | Mnz, Zrn |
| PEL51 | 800 | 196 | BN | 8.53 | 1 | 46.9 | 7.4 | - | 20.2 | tr | 6.6 | - | 0.7 | - | 15.4 | 2.8 | - | - | 0.4 | Mnz, Zrn |
| PEL52 | 800 | 196 | BN | 8.53 | 2.1 | 41.8 | tr | - | 21.7 | tr | 10.6 | - | 0.7 | - | 20.5 | 4.8 | - | - | 22.6 | Mnz, Zrn |
| PEL38 | 800 | 90 | BN | 8.53 | 0 | 48.3 | 6.6 | - | - | 24.7 | 2.8 | - | 0.6 | - | 17.0 | tr | - | - | 7.6 | Zrn |
| PEL39 | 800 | 90 | BN | 8.53 | 1 | 56.3 | - | - | - | 24.9 | 3.4 | - | 0.6 | - | 12.6 | 2.2 | - | - | 11 | Zrn |
| PEL40 | 800 | 90 | BN | 8.53 | 2.1 | 47.0 | - | - | tr | 25.7 | 4.9 | - | 0.6 | - | 19.4 | 2.4 | - | - | 7.1 | Zrn |
| PEL77 | 850 | 170 | MgO | 8.53 | 0 | 58.9 | 17.5 | - | 16.2 | - | - | - | 0.7 | - | 6.3 | tr | <0.1 | 0.3 | 1.4 | |
| PEL78 | 850 | 170 | MgO | 8.53 | 1 | 57.1 | 11.7 | - | 19.2 | - | - | - | 0.7 | - | 8.7 | 2.3 | <0.1 | 0.4 | 0.2 | |
| PEL79 | 850 | 170 | MgO | 8.53 | 2.1 | 60.0 | 1.2 | 4.0 | 21.1 | - | - | - | 0.8 | - | 7.9 | 4.3 | <0.1 | 0.7 | 0.2 | |
| PEL9 | 900 | 91 | MgO | 8.53 | 0 | 68.1 | 14.1 | - | 16.2 | - | - | - | 0.7 | - | tr | 0.1 | <0.1 | 0.8 | 0.0 | |
| PEL13 | 900 | 91 | MgO | 8.53 | 1 | 69.8 | 8.9 | - | 17.6 | - | - | - | 0.7 | - | tr | 2.3 | <0.1 | 0.7 | 0.0 | |
| PEL14 | 900 | 91 | MgO | 8.53 | 2.1 | 71.8 | - | 2.3 | 19.6 | - | - | - | 0.7 | - | tr | 4.1 | <0.1 | 1.4 | 0.1 | Zrn |
| PEL35 | 1000 | 93 | BN | 8.53 | 0 | 70.4 | 10.7 | - | 16.8 | - | - | - | 0.4 | - | - | 0.1 | <0.1 | 1.4 | 0.1 | |
| PEL36 | 1000 | 93 | BN | 8.53 | 1 | 71.4 | 6.6 | - | 17.9 | - | - | - | 0.4 | - | - | 2.1 | <0.1 | 1.7 | 0.1 | Zrn |
| PEL37 | 1000 | 93 | BN | 8.53 | 2.1 | 72.5 | - | - | 20.2 | - | - | - | 0.4 | - | - | 5.0 | <0.1 | 1.8 | 10.9 | |

Phase proportions calculated using a least-square mass balance (Albarède, 1995). Mass balance calculations at T > 850°C include carbonates and Cl-rich phase with putative compositions (Supplementary Data 3). S_{in} represents the amount of sulphur loaded to the capsule. Abbreviations: Ass.: assembly; Grt: garnet; Opx: orthopyroxene; Ky: kyanite; St: staurolite; Bt: biotite; Ph: phengite; Rt: rutile; Ti-Mag: Ti-magnetite; Qz: quartz; Po: pyrrhotite; Cl ph: Cl-rich phases; Cb: carbonate; Zrn: zircon; Mnz: monzazite; tr: traces. Mass balance calculation for PEL69h (in italics) is to consider with caution, see text.

Table 3: Compositions of experimental glasses (normalized to 100 wt% anhydrous)

| Run no. | PEL71 | PEL72 | PEL73 | PEL50 | PEL51 | PEL52 | PEL77 | PEL78 | PEL79 | | | | | | | | | |
|---------------------------------------|-------|-----------------|-----------------|-----------------|-----------------|-----------------|-----------------|-----------------|-----------------|-----------------|-------|------|-------|------|-------|------|-------|------|
| Temperature (°C) | 750 | 750 | 750 | 800 | 800 | 800 | 850 | 850 | 850 | | | | | | | | | |
| Duration (h) | 241 | 241 | 241 | 196 | 196 | 196 | 170 | 170 | 170 | | | | | | | | | |
| H ₂ O _{in} (wt %) | - | - | - | - | - | - | - | - | - | | | | | | | | | |
| S _{in} (wt %) | - | 1 | 2.1 | - | 1 | 2.1 | - | 1 | 2.1 | | | | | | | | | |
| <i>wt%</i> | | <i>sd (n=6)</i> | <i>sd (n=5)</i> | <i>sd (n=6)</i> | <i>sd (n=6)</i> | <i>sd (n=7)</i> | <i>sd (n=7)</i> | <i>sd (n=6)</i> | <i>sd (n=7)</i> | <i>sd (n=6)</i> | | | | | | | | |
| SiO ₂ | 74.69 | 0.49 | 75.35 | 0.60 | 75.03 | 0.47 | 76.52 | 0.49 | 76.84 | 0.39 | 75.35 | 1.07 | 77.90 | 0.58 | 77.83 | 0.30 | 77.30 | 0.38 |
| TiO ₂ | 0.06 | 0.06 | 0.14 | 0.03 | 0.09 | 0.06 | 0.24 | 0.07 | 0.22 | 0.07 | 0.14 | 0.06 | 0.20 | 0.12 | 0.20 | 0.06 | 0.21 | 0.10 |
| Al ₂ O ₃ | 13.83 | 0.29 | 14.72 | 0.41 | 14.41 | 0.44 | 13.46 | 0.47 | 13.15 | 0.17 | 14.05 | 0.88 | 12.79 | 0.14 | 12.53 | 0.20 | 13.30 | 0.24 |
| FeO | 1.12 | 0.12 | 1.16 | 0.07 | 1.16 | 0.12 | 1.42 | 0.11 | 1.26 | 0.14 | 0.98 | 0.09 | 1.73 | 0.11 | 1.58 | 0.14 | 1.51 | 0.10 |
| MnO | 0.01 | 0.01 | 0.07 | 0.05 | 0.07 | 0.10 | 0.06 | 0.05 | 0.05 | 0.07 | 0.06 | 0.06 | 0.02 | 0.04 | 0.04 | 0.04 | 0.04 | 0.06 |
| MgO | 0.54 | 0.04 | 0.67 | 0.02 | 0.75 | 0.07 | 0.65 | 0.04 | 0.83 | 0.07 | 0.94 | 0.06 | 0.67 | 0.02 | 0.91 | 0.03 | 1.51 | 0.05 |
| CaO | 0.56 | 0.05 | 1.19 | 0.03 | 1.41 | 0.09 | 0.50 | 0.06 | 0.75 | 0.05 | 0.67 | 0.02 | 0.48 | 0.03 | 0.51 | 0.03 | 0.63 | 0.03 |
| Na ₂ O | 6.72 | 0.33 | 4.45 | 0.34 | 4.96 | 0.50 | 2.90 | 0.16 | 2.92 | 0.33 | 4.70 | 0.59 | 2.05 | 0.35 | 2.12 | 0.12 | 1.56 | 0.21 |
| K ₂ O | 2.42 | 0.08 | 2.10 | 0.10 | 1.98 | 0.07 | 4.18 | 0.16 | 3.86 | 0.11 | 3.05 | 0.25 | 4.08 | 0.35 | 4.22 | 0.19 | 3.86 | 0.13 |
| P ₂ O ₅ | 0.06 | 0.05 | 0.15 | 0.09 | 0.14 | 0.11 | 0.07 | 0.08 | 0.10 | 0.08 | 0.06 | 0.06 | 0.07 | 0.04 | 0.06 | 0.06 | 0.07 | 0.06 |
| Hydrous total | 91.95 | 0.32 | 90.45 | 1.02 | 90.93 | 0.43 | 90.35 | 0.65 | 88.40 | 1.05 | 90.23 | 1.02 | 89.64 | 1.45 | 90.13 | 0.65 | 88.60 | 0.96 |
| H ₂ O _{by diff.} | 7.2 | 0.3 | 7.3 | 0.9 | 6.7 | 0.7 | 8.4 | 0.6 | 11.0 | 1.0 | 9.4 | 1.1 | 10.2 | 1.4 | 9.7 | 0.6 | 11.2 | 0.9 |
| H ₂ O _{calc.} | 36.4 | 2.9 | 25.6 | 2.0 | 27.2 | 2.4 | 17.1 | 0.2 | 17.5 | 0.3 | 19.3 | 0.5 | 14.4 | 0.1 | 15.4 | 0.1 | 14.1 | 0.1 |
| S melt (ppm) | 322 | 86 | 461 | 36 | 829 | 49 | 72 | 28 | 132 | 33 | 153 | 30 | 728 | 34 | 685 | 27 | 1033 | 42 |
| n(S) | 7 | - | 6 | - | 6 | - | 8 | - | 7 | - | 7 | - | 7 | - | 7 | - | 7 | - |
| X _{Mg} | 0.46 | 0.02 | 0.51 | 0.01 | 0.54 | 0.02 | 0.45 | 0.02 | 0.54 | 0.02 | 0.63 | 0.02 | 0.41 | 0.02 | 0.51 | 0.02 | 0.64 | 0.02 |
| X _{Ca} | 0.26 | 0.02 | 0.39 | 0.02 | 0.42 | 0.03 | 0.20 | 0.02 | 0.26 | 0.02 | 0.24 | 0.01 | 0.17 | 0.01 | 0.17 | 0.00 | 0.16 | 0.01 |
| A/CNK | 0.94 | 0.05 | 1.25 | 0.06 | 1.13 | 0.10 | 1.32 | 0.08 | 1.28 | 0.08 | 1.16 | 0.13 | 1.49 | 0.18 | 1.39 | 0.02 | 1.69 | 0.11 |
| NK/A | 0.99 | 0.05 | 0.65 | 0.04 | 0.72 | 0.07 | 0.69 | 0.04 | 0.68 | 0.05 | 0.79 | 0.10 | 0.61 | 0.08 | 0.64 | 0.01 | 0.51 | 0.04 |
| K/Na | 0.24 | 0.01 | 0.31 | 0.03 | 0.27 | 0.02 | 0.95 | 0.05 | 0.88 | 0.11 | 0.43 | 0.05 | 1.32 | 0.12 | 1.31 | 0.13 | 1.64 | 0.17 |
| Ab% | 76.95 | - | 67.32 | - | 69.15 | - | 47.43 | - | 48.26 | - | 65.10 | - | 39.64 | - | 39.54 | - | 33.80 | - |
| An% | 3.74 | - | 10.53 | - | 11.53 | - | 4.80 | - | 7.24 | - | 5.43 | - | 5.46 | - | 5.60 | - | 8.02 | - |
| Or% | 19.31 | - | 22.144 | - | 19.325 | - | 47.77 | - | 44.503 | - | 29.47 | - | 54.9 | - | 54.86 | - | 58.17 | - |

Table 3, continued

| Run no. | PEL9 | PEL13 | PEL14 | PEL35 | PEL36 | PEL37 | PEL68H | PEL69H | | | | | | | | |
|---------------------------------------|-------|-----------------|-----------------|-----------------|-----------------|-----------------|-----------------|-----------------|-----------------|------|-------|------|-------|------|-------|------|
| Temperature (°C) | 900 | 900 | 900 | 1000 | 1000 | 1000 | 900 | 900 | | | | | | | | |
| Duration (h) | 91 | 91 | 91 | 93 | 93 | 93 | 94 | 94 | | | | | | | | |
| H ₂ O _{in} (wt %) | - | - | - | - | - | - | 6.5 | 6.7 | | | | | | | | |
| S _{in} (wt %) | - | 1 | 2.1 | - | 1 | 2.1 | - | 1 | | | | | | | | |
| <i>wt%</i> | | <i>sd (n=6)</i> | <i>sd (n=5)</i> | <i>sd (n=8)</i> | <i>sd (n=5)</i> | <i>sd (n=5)</i> | <i>sd (n=6)</i> | <i>sd (n=6)</i> | <i>sd (n=5)</i> | | | | | | | |
| SiO ₂ | 78.03 | 0.26 | 78.13 | 0.63 | 78.14 | 0.49 | 77.49 | 0.28 | 77.93 | 0.09 | 78.55 | 0.35 | 78.13 | 0.59 | 74.32 | 1.33 |
| TiO ₂ | 0.34 | 0.12 | 0.38 | 0.08 | 0.42 | 0.09 | 0.70 | 0.12 | 0.80 | 0.09 | 0.74 | 0.12 | 0.23 | 0.06 | 0.30 | 0.04 |
| Al ₂ O ₃ | 12.26 | 0.23 | 12.25 | 0.15 | 12.70 | 0.19 | 12.48 | 0.14 | 12.55 | 0.14 | 12.73 | 0.16 | 12.28 | 0.20 | 12.05 | 0.19 |
| FeO | 2.87 | 0.17 | 2.33 | 0.14 | 2.06 | 0.19 | 4.30 | 0.08 | 3.48 | 0.20 | 2.13 | 0.32 | 2.07 | 0.31 | 2.91 | 0.66 |
| MnO | 0.02 | 0.03 | 0.06 | 0.08 | 0.05 | 0.08 | 0.04 | 0.05 | 0.09 | 0.07 | 0.01 | 0.02 | 0.01 | 0.02 | 0.03 | 0.07 |
| MgO | 1.10 | 0.03 | 1.44 | 0.03 | 2.22 | 0.06 | 1.36 | 0.05 | 1.69 | 0.05 | 2.45 | 0.08 | 0.98 | 0.09 | 1.84 | 0.51 |
| CaO | 0.49 | 0.02 | 0.52 | 0.04 | 0.51 | 0.04 | 0.48 | 0.01 | 0.48 | 0.04 | 0.52 | 0.02 | 0.49 | 0.03 | 0.47 | 0.05 |
| Na ₂ O | 1.40 | 0.11 | 1.46 | 0.32 | 0.83 | 0.14 | 0.82 | 0.11 | 0.65 | 0.13 | 0.49 | 0.05 | 1.94 | 0.19 | 3.61 | 0.42 |
| K ₂ O | 3.37 | 0.13 | 3.40 | 0.25 | 2.97 | 0.22 | 2.29 | 0.17 | 2.27 | 0.18 | 2.28 | 0.11 | 3.74 | 0.22 | 4.21 | 0.24 |
| P ₂ O ₅ | 0.12 | 0.07 | 0.04 | 0.03 | 0.10 | 0.06 | 0.05 | 0.01 | 0.07 | 0.05 | 0.08 | 0.06 | 0.13 | 0.14 | 0.25 | 0.28 |
| Hydrous total | 86.74 | 0.90 | 86.76 | 0.80 | 84.99 | 1.05 | 85.81 | 0.96 | 85.60 | 0.61 | 84.50 | 0.51 | 88.39 | 1.54 | 88.10 | 0.50 |
| H ₂ O _{by diff.} | 12.6 | 1.0 | 11.4 | 0.7 | 13.7 | 1.1 | 12.7 | 0.8 | 13.0 | 0.5 | 14.0 | 0.4 | 10.9 | 1.2 | 10.9 | 0.7 |
| H ₂ O _{calc.} | 12.4 | 0.1 | 12.2 | 0.1 | 11.7 | 0.1 | 12.1 | 0.1 | 11.9 | 0.1 | 11.8 | 0.1 | 22.7 | - | 22.1 | - |
| S melt (ppm) | 658 | 7 | 849 | 42 | 980 | 27 | 254 | 82 | 261 | 61 | 226 | 27 | 698 | 54 | 3507 | 607 |
| n(S) | 9 | - | 9 | - | 9 | - | 8 | - | 7 | - | 8 | - | 8 | - | 4 | - |
| X _{Mg} | 0.41 | 0.02 | 0.52 | 0.02 | 0.66 | 0.02 | 0.36 | 0.01 | 0.46 | 0.01 | 0.67 | 0.03 | 0.46 | 0.03 | 0.53 | 0.06 |
| X _{Ca} | 0.12 | 0.01 | 0.12 | 0.01 | 0.10 | 0.01 | 0.08 | 0.00 | 0.09 | 0.00 | 0.09 | 0.00 | 0.14 | 0.02 | 0.10 | 0.02 |
| A/CNK | 1.79 | 0.10 | 1.76 | 0.20 | 2.32 | 0.16 | 2.66 | 0.15 | 2.87 | 0.22 | 3.02 | 0.10 | 1.57 | 0.05 | 1.05 | 0.12 |
| NK/A | 0.49 | 0.03 | 0.50 | 0.07 | 0.36 | 0.03 | 0.31 | 0.02 | 0.28 | 0.03 | 0.26 | 0.01 | 0.57 | 0.02 | 0.89 | 0.11 |
| K/Na | 1.59 | 0.10 | 1.57 | 0.24 | 2.41 | 0.28 | 1.86 | 0.30 | 2.38 | 0.44 | 3.08 | 0.35 | 1.33 | 0.11 | 0.76 | 0.05 |
| Ab% | 34.65 | - | 35.33 | - | 25.82 | - | 30.42 | - | 25.71 | - | 20.54 | - | 40.09 | - | 52.89 | - |
| An% | 7.15 | - | 7.32 | - | 9.32 | - | 10.46 | - | 11.16 | - | 12.83 | - | 5.92 | - | 4.03 | - |
| Or% | 58.19 | - | 57.35 | - | 64.86 | - | 59.13 | - | 63.12 | - | 66.63 | - | 53.99 | - | 43.08 | - |

H₂O_{in} and S_{in} represent the amounts of water and sulphur loaded to the capsule, respectively. *sd*: 1 sigma standard deviation on multiple analyses (number of analyses given in brackets); n(S) : number of analyses of sulphur. H₂O estimated by the by-difference method (H₂O_{by diff.}) or by mass-balance constraints (H₂O_{calc.})

Table 4: Trace element compositions of starting material B12a and experimental glasses

| Run no. | B12a | PEL71 | PEL72 | PEL73 | PEL50 | PEL52 | PEL77 | PEL78 | | | | | | | |
|------------------------|-------------|-----------------|-----------------|-----------------|-----------------|-----------------|-----------------|-----------------|------|--------|------|-------------------|------|-------------------|------|
| T (°C) | | 750 | 750 | 750 | 800 | 800 | 850 | 850 | | | | | | | |
| Duration (h) | | 241 | 241 | 241 | 196 | 196 | 170 | 170 | | | | | | | |
| S _{in} (wt %) | | - | 1 | 2.1 | - | 2.1 | - | 1 | | | | | | | |
| <i>ppm</i> | | <i>sd (n=2)</i> | <i>sd (n=1)</i> | <i>sd (n=3)</i> | <i>sd (n=2)</i> | <i>sd (n=5)</i> | <i>sd (n=4)</i> | <i>sd (n=5)</i> | | | | | | | |
| Li | 55.1 | 100.3 | 1.4 | 92.2 | - | 123.4 | 8.0 | 99.8 | 0.9 | 110.3 | 8.4 | 96.9 | 4.6 | 99.8 | 3.6 |
| Be | 2.29 | < 8.27 | - | < 9.23 | - | < 8.42 | - | 5.13 | 0.83 | < 4.74 | - | < 4.37 | - | < 5.20 | - |
| B | 77 | 263 | 26 | 258 | - | 371 | 19 | n.a | - | 198 | - | 231 | 7 | 181 | 10 |
| Rb | 112 | 110.2 | 4.4 | 101.6 | - | 108.9 | 2.6 | 216.5 | 5.9 | 149.3 | 14.3 | 224.4 | 6.1 | 215.1 | 1.0 |
| Sr | 114 | 252 | 15 | 228 | - | 350 | 24 | 218 | 7 | 205 | 11 | 207 | 3 | 190 | 2 |
| Y | 25.4 | < 0.45 | - | < 0.34 | - | 43.35 | 1.80 | < 0.23 | - | 39.93 | 1.58 | < 0.41 | - | < 0.35 | - |
| Zr | 155 | 26.0 | 0.5 | 29.5 | - | 47.0 | 2.1 | 69.9 | 0.2 | 80.4 | 5.5 | 112.5 | 0.7 | 115.0 | 1.0 |
| Nb | 13.5 | 1.71 | 0.14 | 1.80 | - | 2.16 | 0.18 | 1.44 | 0.13 | 2.99 | 0.26 | 2.83 | 0.15 | 2.92 | 0.12 |
| Ba | 447 | 252 | 23 | 233 | - | 378 | 37 | 724 | 16 | 645 | 26 | 822 | 8 | 749 | 6 |
| La | 38.8 | 16.3 | 0.4 | 17.9 | - | 34.2 | 1.5 | 54.2 | 0.2 | 53.6 | 2.1 | 73.6 | 2.0 | 62.9 | 2.1 |
| Ce | 74.4 | 33.3 | 1.2 | 34.5 | - | 67.8 | 7.0 | 106.0 | 4.6 | 106.7 | 4.8 | 139.8 | 3.8 | 119.9 | 3.8 |
| Nd | 32.6 | 13.5 | 0.1 | 14.7 | - | 30.2 | 2.6 | 42.1 | 0.3 | 46.7 | 2.2 | 57.0 | 1.9 | 50.6 | 2.1 |
| Sm | 6.35 | < 2.58 | - | < 3.16 | - | 7.88 | 0.82 | 5.54 | 0.80 | 9.49 | 1.08 | 6.61 | 0.41 | 7.65 | 0.68 |
| Eu | 1.34 | < 0.73 | - | < 0.57 | - | 2.04 | 0.69 | 0.72 | 0.02 | 2.18 | 0.26 | 1.13 | 0.13 | 1.55 | 0.13 |
| Dy | 4.8 | < 1.50 | - | < 1.08 | - | 8.92 | 0.29 | < 0.59 | - | 7.27 | 0.67 | 0.74 | 0.09 | 0.82 | 0.04 |
| Yb | 2.76 | < 1.75 | - | < 1.33 | - | 2.62 | 0.26 | < 0.73 | - | 4.19 | 0.26 | < 0.88 | - | 0.95 | 0.04 |
| Hf | 4.3 | < 1.52 | - | < 1.87 | - | < 1.54 | - | 2.50 | 0.01 | 2.45 | 0.55 | 4.06 | 0.15 | 3.30 | 0.44 |
| Ta | 1.15 | 0.56 | 0.00 | 0.34 | - | n.a | - | < 0.16 | - | 0.27 | 0.05 | n.a | - | n.a | - |
| Pb | 22.5 | 63.5 | 8.7 | 73.8 | - | 96.2 | 2.7 | 52.3 | 3.3 | 50.4 | 5.5 | 53.6 ^a | 1.2 | 50.2 ^a | 0.8 |
| Th | 13.6 | 9.1 | 0.4 | 7.2 | - | 13.6 | 0.1 | 18.6 | 0.4 | 18.6 | 0.9 | 27.0 | 1.8 | 18.5 | 1.3 |
| U | 2.78 | 2.74 | 0.05 | 2.58 | - | 5.84 | 0.36 | 3.88 | 0.01 | 4.24 | 0.47 | 5.36 | 0.33 | 3.82 | 0.32 |
| Ba/Th | 32.9 | 27.6 | 2.8 | 32.6 | - | 27.8 | 2.7 | 38.9 | 1.2 | 34.8 | 2.2 | 30.5 | 2.0 | 40.5 | 2.8 |
| (La/Sm) _{PM} | 3.82 | - | - | - | - | 2.71 | 0.19 | 6.11 | 0.55 | 3.53 | 0.27 | 6.96 | 0.30 | 5.14 | 0.19 |
| Th/La | 0.35 | 0.56 | 0.03 | 0.40 | - | 0.40 | 0.02 | 0.34 | 0.01 | 0.35 | 0.02 | 0.37 | 0.03 | 0.29 | 0.02 |
| U/Th | 0.20 | 0.30 | 0.02 | 0.36 | - | 0.43 | 0.03 | 0.21 | 0.00 | 0.23 | 0.03 | 0.20 | 0.02 | 0.21 | 0.02 |
| Zr/Hf | 36.0 | - | - | - | - | - | - | 28.0 | 0.2 | 32.8 | 7.6 | 27.7 | 1.0 | 34.8 | 4.6 |
| Nb/Ta | 11.7 | 3.1 | 0.3 | 5.3 | - | - | - | - | - | 11.1 | 2.4 | - | - | - | - |
| Ce/Pb | 3.31 | 0.52 | 0.07 | 0.47 | - | 0.70 | 0.08 | 2.03 | 0.16 | 2.12 | 0.25 | - | - | - | - |

Table 4, continued

| Run no. | PEL79 | PEL9 | PEL13 | PEL14 | PEL35 | PEL36 | PEL37 | | | | | | | |
|------------------------|-------------------|-----------------|-------------------|-----------------|-------------------|-----------------|-------------------|-----------------|-------------------|------|-------------------|------|-------------------|------|
| T (°C) | 850 | 900 | 900 | 900 | 1000 | 1000 | 1000 | | | | | | | |
| Duration (h) | 170 | 91 | 91 | 91 | 93 | 93 | 93 | | | | | | | |
| S _{in} (wt %) | 2.10 | - | 1 | 2.1 | - | 1 | 2.1 | | | | | | | |
| <i>ppm</i> | | <i>sd</i> (n=5) | <i>sd</i> (n=7) | <i>sd</i> (n=7) | <i>sd</i> (n=6) | <i>sd</i> (n=6) | <i>sd</i> (n=6) | <i>sd</i> (n=4) | | | | | | |
| Li | 93.6 | 6.4 | 75.3 | 4.2 | 75.5 | 1.5 | 70.9 | 6.0 | 82.8 | 5.2 | 83.6 | 0.6 | 78.4 | 6.0 |
| Be | < 4.01 | - | 2.96 | 0.21 | 2.96 | 0.24 | 2.72 | 0.33 | 2.99 | 0.36 | 2.93 | 0.27 | 2.42 | 0.66 |
| B | 171 | 15 | 204 | 47 | n.a | - | n.a | - | n.a | - | 93 | 10 | n.a | - |
| Rb | 195.9 | 14.9 | 162.9 | 4.5 | 163.4 | 1.2 | 150.3 | 8.0 | 151.0 | 10.7 | 155.7 | 2.3 | 140.1 | 8.0 |
| Sr | 185 | 8 | 147 | 2 | 143 | 0 | 133 | 3 | 136 | 7 | 135 | 2 | 124 | 6 |
| Y | 28.97 | 1.28 | 3.39 | 0.85 | 8.23 | 0.70 | 27.53 | 0.53 | 14.12 | 0.83 | 18.65 | 0.50 | 25.44 | 1.17 |
| Zr | 122.9 | 6.2 | 138.7 | 2.1 | 161.7 | 2.3 | 152.2 | 11.2 | n.a | - | 180.0 | 2.9 | 174.5 | 7.9 |
| Nb | 3.25 | 0.19 | 4.21 | 0.24 | 4.78 | 0.55 | 4.52 | 0.34 | 10.03 | 0.62 | 10.16 | 0.12 | 9.79 | 0.42 |
| Ba | 725 | 29 | 583 | 9 | 581 | 3 | 531 | 11 | 525 | 28 | 528 | 6 | 479 | 24 |
| La | 60.5 | 2.4 | 48.9 | 0.8 | 47.0 | 0.3 | 43.7 | 1.3 | 46.7 | 2.5 | 46.6 | 0.3 | 42.2 | 2.0 |
| Ce | 115.6 | 4.4 | 97.9 | 1.0 | 97.1 | 0.6 | 89.7 | 2.6 | 88.5 | 4.5 | 88.7 | 0.6 | 80.7 | 3.9 |
| Nd | 49.9 | 2.1 | 41.0 | 0.6 | 41.0 | 0.3 | 38.1 | 1.4 | 38.6 | 2.4 | 38.7 | 0.3 | 35.2 | 1.5 |
| Sm | 9.35 | 0.61 | 6.81 | 0.19 | 7.05 | 0.20 | 7.14 | 0.33 | 6.91 | 0.25 | 7.19 | 0.28 | 6.72 | 0.41 |
| Eu | 2.10 | 0.07 | 1.32 | 0.03 | 1.39 | 0.05 | 1.47 | 0.07 | 1.52 | 0.10 | 1.54 | 0.04 | 1.49 | 0.14 |
| Dy | 6.00 | 0.26 | 1.02 | 0.17 | 2.20 | 0.13 | 5.41 | 0.19 | 3.26 | 0.25 | 4.11 | 0.15 | 4.92 | 0.41 |
| Yb | 2.18 | 0.42 | 0.28 | 0.11 | 0.37 | 0.10 | 3.09 | 0.13 | 0.97 | 0.16 | 1.40 | 0.16 | 2.80 | 0.21 |
| Hf | 3.50 | 0.35 | 4.02 | 0.09 | 4.54 | 0.13 | 4.18 | 0.27 | 4.56 | 0.21 | 4.89 | 0.19 | 4.18 | 0.28 |
| Ta | n.a | - | 0.26 | 0.01 | 0.30 | 0.05 | 0.27 | 0.02 | n.a | - | n.a | - | n.a | - |
| Pb | 54.3 ^a | 4.0 | 43.2 ^a | 1.9 | 44.5 ^a | 0.4 | 45.8 ^a | 1.6 | 63.0 ^a | 4.7 | 53.8 ^a | 0.9 | 45.0 ^a | 3.2 |
| Th | 17.1 | 0.6 | 16.5 | 0.6 | 16.8 | 0.5 | 15.1 | 1.4 | 15.5 | 0.8 | 15.8 | 0.1 | 14.1 | 0.7 |
| U | 3.51 | 0.13 | 3.66 | 0.08 | 3.70 | 0.09 | 3.39 | 0.33 | 3.38 | 0.18 | 3.44 | 0.02 | 3.09 | 0.19 |
| Ba/Th | 42.4 | 2.3 | 35.2 | 1.3 | 34.5 | 1.0 | 35.3 | 3.4 | 33.8 | 2.6 | 33.3 | 0.5 | 34.1 | 2.5 |
| (La/Sm) _{PM} | 4.04 | 0.09 | 4.49 | 0.09 | 4.17 | 0.07 | 3.83 | 0.13 | 4.22 | 0.17 | 4.05 | 0.10 | 3.93 | 0.19 |
| Th/La | 0.28 | 0.02 | 0.34 | 0.01 | 0.36 | 0.01 | 0.35 | 0.03 | 0.33 | 0.03 | 0.34 | 0.00 | 0.33 | 0.02 |
| U/Th | 0.21 | 0.01 | 0.22 | 0.01 | 0.22 | 0.01 | 0.22 | 0.03 | 0.22 | 0.02 | 0.22 | 0.00 | 0.22 | 0.02 |
| Zr/Hf | 35.1 | 3.9 | 34.5 | 1.0 | 35.7 | 1.2 | 36.4 | 3.5 | - | - | 36.8 | 1.6 | 41.7 | 3.4 |
| Nb/Ta | - | - | 16.4 | 1.3 | 16.0 | 3.4 | 16.7 | 1.9 | - | - | - | - | - | - |
| Ce/Pb | - | - | - | - | - | - | - | - | - | - | - | - | - | - |

n.a: not analysed. sd: 1 sigma standard deviation on multiple analyses (number of analyses given in brackets). (La/Sm)_{PM} = La/Sm ratio normalized to the primitive mantle (McDonough & Sun, 1995).^aPb contamination suspected (see text).

Table 5: Garnet-melt partition coefficients

| Run no. | PEL71 | | PEL72 | | PEL50 | | PEL77 | | PEL78 | | PEL79 | | PEL9 | | PEL13 | | PEL35 | | PEL36 | |
|----------------------|-------------------|-------|-------------------|------|-------------------|-------|-------------------|-------|-------------------|-------|-------------------|-------|-------------------|-------|-------------------|-------|-------------------|-------|-------------------|-------|
| T (°C) | 750 | | 750 | | 800 | | 850 | | 850 | | 850 | | 900 | | 900 | | 1000 | | 1000 | |
| Duration (h) | 241 | | 241 | | 196 | | 170 | | 170 | | 170 | | 91 | | 91 | | 93 | | 93 | |
| S_{in} (wt %) | - | | 1 | | - | | - | | 1 | | 2.1 | | - | | 1 | | - | | 1 | |
| <i>D</i> garnet-melt | <i>l</i> σ | | <i>l</i> σ | | <i>l</i> σ | | <i>l</i> σ | | <i>l</i> σ | | <i>l</i> σ | | <i>l</i> σ | | <i>l</i> σ | | <i>l</i> σ | | <i>l</i> σ | |
| Li | 0.38 | 0.01 | 0.84 | - | 0.25 | 0.00 | 0.35 | 0.06 | 0.35 | 0.03 | 0.43 | 0.03 | 0.22 | 0.03 | 0.22 | 0.01 | 0.21 | 0.04 | 0.17 | 0.01 |
| Be | - | - | - | - | - | - | - | - | - | - | - | - | - | - | - | - | - | - | - | - |
| B | - | - | - | - | - | - | - | - | - | - | - | - | - | - | - | - | - | - | - | - |
| Rb | - | - | 0.025 | - | 0.007 | 0.000 | - | - | - | - | - | - | - | - | 0.004 | 0.002 | - | - | - | - |
| Ba | - | - | - | - | 0.007 | 0.000 | - | - | - | - | - | - | - | - | 0.004 | 0.002 | - | - | - | - |
| Th | - | - | 0.285 | - | 0.020 | 0.000 | 0.076 | 0.013 | - | - | - | - | - | - | 0.004 | 0.002 | - | - | - | - |
| U | 0.60 | 0.01 | 0.31 | - | - | - | 0.25 | 0.02 | - | - | - | - | 0.03 | 0.01 | 0.03 | 0.01 | 0.09 | 0.01 | - | - |
| Nb | - | - | - | - | - | - | - | - | - | - | - | - | - | - | 0.04 | 0.02 | - | - | - | - |
| Ta | - | - | - | - | - | - | - | - | - | - | - | - | - | - | - | - | - | - | - | - |
| La | - | - | - | - | 0.01 | 0.00 | 0.02 | 0.00 | - | - | - | - | - | - | 0.003 | 0.001 | - | - | - | - |
| Ce | 0.094 | 0.003 | 0.106 | - | 0.021 | 0.001 | 0.056 | 0.006 | 0.008 | 0.002 | 0.004 | 0.000 | 0.007 | 0.003 | 0.008 | 0.003 | 0.013 | 0.003 | 0.004 | 0.001 |
| Pb | 0.115 | 0.016 | - | - | 0.014 | 0.001 | - | - | - | - | - | - | - | - | 0.003 | 0.001 | - | - | - | - |
| Sr | 0.01 | 0.00 | 0.004 | - | 0.009 | 0.000 | - | - | - | - | - | - | 0.001 | 0.000 | 0.003 | 0.002 | 0.005 | 0.002 | - | - |
| Nd | 1.86 | 0.01 | 0.86 | - | 0.37 | 0.00 | 0.67 | 0.05 | 0.13 | 0.01 | 0.06 | 0.01 | 0.11 | 0.04 | 0.10 | 0.03 | 0.17 | 0.02 | 0.06 | 0.01 |
| Sm | - | - | - | - | 4.38 | 0.63 | 6.17 | 0.46 | 1.45 | 0.15 | 0.78 | 0.07 | 0.94 | 0.14 | 0.87 | 0.22 | 1.04 | 0.06 | 0.44 | 0.10 |
| Zr | 3.62 | 0.07 | 1.84 | - | 1.51 | 0.00 | 2.57 | 0.03 | 1.21 | 0.04 | 0.69 | 0.05 | 1.32 | 0.08 | 1.08 | 0.16 | - | - | 0.69 | 0.08 |
| Hf | - | - | - | - | 0.84 | 0.00 | 1.33 | 0.15 | 0.78 | 0.22 | 0.51 | 0.14 | 0.83 | 0.12 | 0.63 | 0.11 | 0.71 | 0.18 | 0.53 | 0.16 |
| Eu | - | - | - | - | 11.08 | 0.38 | 6.63 | 0.96 | 2.57 | 0.28 | 1.28 | 0.22 | 1.16 | 0.16 | 1.54 | 0.32 | 0.70 | 0.08 | 0.64 | 0.25 |
| Ti | 6.37 | 6.26 | 3.19 | 0.65 | 1.66 | 0.74 | 3.89 | 2.50 | 2.39 | 0.97 | 1.92 | 1.15 | 1.39 | 0.85 | 0.97 | 0.36 | 0.21 | 0.04 | 0.52 | 0.27 |
| Dy | - | - | - | - | - | - | 210 | 28 | 156 | 21 | 15.2 | 1.0 | 48.6 | 8.7 | 17.2 | 3.7 | 13.0 | 3.0 | 5.26 | 0.62 |
| Y | - | - | - | - | - | - | - | - | - | - | 25.79 | 1.59 | 87.50 | 23.82 | 27.81 | 6.07 | 19.14 | 5.66 | 7.02 | 0.92 |
| Yb | - | - | - | - | - | - | 148 | 19 | 191 | 110 | 121 | 25 | 136 | 63 | 91.2 | 33.6 | 53.4 | 26.8 | 14.4 | 4.86 |
| Zr/Hf | - | - | - | - | 1.8 | 0.0 | 1.9 | 0.2 | 1.6 | 0.4 | 1.4 | 0.4 | 1.6 | 0.3 | 1.7 | 0.4 | - | - | 1.3 | 0.4 |
| U/Th | - | - | 1.1 | - | - | - | 3.3 | 0.6 | - | - | - | - | - | - | 6.7 | 4.3 | - | - | - | - |

Table 6: Orthopyroxene-melt partition coefficients

| Run no. | PEL79 | | PEL14 | |
|-----------------------------|--------------|-----------|--------------|-----------|
| T (°C) | 850 | | 900 | |
| Duration (h) | 170 | | 91 | |
| S_{in} (wt %) | 2.1 | | 2.1 | |
| <i>D orthopyroxene-melt</i> | | <i>1σ</i> | | <i>1σ</i> |
| Li | 0.65 | 0.04 | 0.57 | 0.05 |
| Be | - | - | 0.22 | 0.03 |
| B | - | - | - | - |
| Rb | - | - | - | - |
| Ba | - | - | - | - |
| Th | 0.129 | 0.005 | 0.023 | 0.002 |
| U | - | - | 0.024 | 0.002 |
| Nb | - | - | 0.32 | 0.02 |
| Ta | - | - | 0.32 | 0.03 |
| La | 0.009 | 0.000 | 0.004 | 0.000 |
| Ce | 0.008 | 0.000 | 0.005 | 0.000 |
| Pb | - | - | - | - |
| Sr | 0.003 | 0.000 | 0.002 | 0.000 |
| Nd | - | - | 0.009 | 0.000 |
| Sm | - | - | - | - |
| Zr | 0.05 | 0.00 | 0.06 | 0.00 |
| Hf | - | - | 0.10 | 0.01 |
| Eu | - | - | - | - |
| Ti | 0.60 | 0.29 | 0.36 | 0.07 |
| Dy | - | - | 0.11 | 0.00 |
| Y | 0.13 | 0.01 | 0.08 | 0.00 |
| Yb | - | - | 0.16 | 0.01 |

Table 7: Phengite- and biotite-melt partition coefficients

| Run no. | PEL71 | | PEL72 | | PEL50 | | PEL73 | | PEL52 | |
|-----------------|---------------|-----------|---------------|-----------|---------------|-----------|---------------|-----------|---------------|-----------|
| T(°C) | 750 | | 750 | | 800 | | 750 | | 800 | |
| Duration (h) | 241 | | 241 | | 196 | | 241 | | 196 | |
| S_{in} (wt %) | - | | 1 | | - | | 2.1 | | 2.1 | |
| | $D^{Ph/melt}$ | 1σ | $D^{Ph/melt}$ | 1σ | $D^{Ph/melt}$ | 1σ | $D^{Bt/melt}$ | 1σ | $D^{Bt/melt}$ | 1σ |
| Li | 0.61 | 0.01 | 0.58 | - | 0.30 | 0.00 | 0.65 | 0.04 | 0.49 | 0.05 |
| Be | - | - | - | - | - | - | - | - | - | - |
| B | 0.16 | 0.02 | 0.23 | - | - | - | 0.05 | 0.00 | - | - |
| Rb | 3.72 | 0.15 | 4.04 | - | 2.67 | 0.07 | 3.69 | 0.09 | 3.68 | 0.42 |
| Ba | 6.21 | 0.56 | 6.72 | - | 3.01 | 0.06 | 2.07 | 0.20 | 2.03 | 0.18 |
| Th | 0.09 | 0.00 | 0.18 | - | - | - | 0.20 | 0.00 | 0.03 | 0.01 |
| U | - | - | 0.60 | - | - | - | 0.16 | 0.01 | - | - |
| Nb | 2.25 | 0.19 | 1.97 | - | 2.60 | 0.24 | 0.82 | 0.07 | 0.75 | 0.21 |
| Ta | - | - | - | - | - | - | - | - | - | - |
| La | 0.13 | 0.00 | 0.17 | - | - | - | 0.06 | 0.00 | - | - |
| Ce | 0.12 | 0.00 | 0.17 | - | 0.01 | 0.00 | 0.06 | 0.01 | - | - |
| Pb | 0.19 | 0.03 | 0.26 | - | 0.11 | 0.01 | 0.14 | 0.00 | 0.08 | 0.02 |
| Sr | 0.41 | 0.02 | 0.43 | - | 0.18 | 0.01 | 0.09 | 0.01 | 0.05 | 0.01 |
| Nd | - | - | - | - | - | - | 0.13 | 0.01 | - | - |
| Sm | - | - | - | - | - | - | - | - | - | - |
| Zr | 0.30 | 0.01 | - | - | 0.12 | 0.00 | 0.21 | 0.01 | 0.03 | 0.00 |
| Hf | - | - | - | - | - | - | - | - | - | - |
| Eu | - | - | - | - | - | - | - | - | - | - |
| Ti | 11.55 | 16.74 | 3.39 | 0.60 | 4.91 | 1.49 | 15.01 | 9.68 | 12.10 | 5.16 |
| Dy | - | - | - | - | - | - | - | - | - | - |
| Y | - | - | - | - | - | - | 0.05 | 0.00 | - | - |
| Yb | - | - | - | - | - | - | 0.70 | 0.07 | - | - |

Table 8: Pb sulphide-melt partition coefficients

| Run no. | PEL52 | PEL79 | PEL13 | PEL37 |
|------------------------|--------------|--------------|--------------|--------------|
| T(°C) | 800 | 850 | 900 | 1000 |
| Duration (h) | 196 | 170 | 91 | 93 |
| S _{in} (wt %) | 2.1 | 2.1 | 1 | 2.1 |

| <i>D sulphide-melt</i> | <i>1σ</i> | | <i>1σ</i> | | <i>1σ</i> | | <i>1σ</i> | |
|------------------------|-----------|------|-----------|---|-----------|------|-----------|---|
| Pb | 0.40 | 0.23 | 0.44 | - | 0.13 | 0.00 | 0.54 | - |